



저작자표시-비영리-변경금지 2.0 대한민국

이용자는 아래의 조건을 따르는 경우에 한하여 자유롭게

- 이 저작물을 복제, 배포, 전송, 전시, 공연 및 방송할 수 있습니다.

다음과 같은 조건을 따라야 합니다:



저작자표시. 귀하는 원저작자를 표시하여야 합니다.



비영리. 귀하는 이 저작물을 영리 목적으로 이용할 수 없습니다.



변경금지. 귀하는 이 저작물을 개작, 변형 또는 가공할 수 없습니다.

- 귀하는, 이 저작물의 재이용이나 배포의 경우, 이 저작물에 적용된 이용허락조건을 명확하게 나타내어야 합니다.
- 저작권자로부터 별도의 허가를 받으면 이러한 조건들은 적용되지 않습니다.

저작권법에 따른 이용자의 권리는 위의 내용에 의하여 영향을 받지 않습니다.

이것은 [이용허락규약\(Legal Code\)](#)을 이해하기 쉽게 요약한 것입니다.

[Disclaimer](#)

공학박사 학위논문

**Enhanced waveguide-based near-eye
displays with polarization multiplexing**

편광 다중화를 이용하여 향상된 기능을 제공하는
도파관 기반의 근안 디스플레이

2021년 2월

서울대학교 대학원

전기정보공학부

유 찬 형

Enhanced waveguide-based near-eye displays with polarization multiplexing

지도 교수 이 병 호

이 논문을 공학박사 학위논문으로 제출함
2021년 2월

서울대학교 대학원
전기정보공학부
유 찬 형

유찬형의 공학박사 학위논문을 인준함
2021년 2월

위 원 장 鄭潤榮 (인)

부위원장 李竝浩 (인) *Joseph Lee*

위 원 姜勳宗 (인)

위 원 이재상 (인)

위 원 이홍석 (인) *홍석*

Abstract

Enhanced waveguide-based near-eye displays with polarization multiplexing

Chanhyung Yoo

Department of Electrical and Computer Engineering

College of Engineering

Seoul National University

This dissertation presents the studies on the optical design method that enhances the display performance of see-through waveguide-based near-eye displays (WNEDs) using the polarization multiplexing technique. The studies focus on the strategies to improve the crucial display performances without compromising a small form factor, the most attractive merit of the WNEDs. To achieve this goal, thin and lightweight polarization-dependent optical elements are devised and employed in the WNED structure. The polarization-dependent devices can allow multiple optical functions or optical paths depending on the polarization state of the input beam, which can break through the limitation of the waveguide system with the polarization multiplexing.

To realize the function-selective eyepiece for AR applications, the proposed devices should operate as an optically transparent window for the real scene while performing specific optical functions for the virtual image. The proposed devices are manufactured in a combination structure in which polarization-dependent optical elements are stacked. The total thickness of the stacked structure is about 1 mm, and it can be attached to the waveguide surface without conspicuously

increasing the form factor of the optical system.

Using the proposed polarization-dependent devices, the author proposes three types of novel WNED systems with enhanced performance. First, the author suggests a compact WNED with dual focal planes. Conventional WNEDs have an inherent limitation that the focal plane of the virtual image is at an infinite distance because they extract a stream of collimated light at the out-coupler. By using the polarization-dependent eyepiece lens, an additional focal plane can be generated with the polarization multiplexing in addition to infinity depth. The proposed configuration can provide comfortable AR environments by alleviating visual fatigue caused by vergence-accommodation conflict. Second, the novel WNED configuration with extended field-of-view (FOV) is presented. In the WNEDs, the maximum allowable FOV is determined by the material properties of the diffraction optics and the substrate. By using the polarization-dependent steering combiner, the FOV can be extended up to two times, which can provide more immersive AR experiences. In addition, this dissertation demonstrates that the distortion for the real scene caused by the stacked structure cannot severely disturb the image quality, considering the acuity of human vision. Lastly, the author presents a retinal projection-based WNED with switchable viewpoints by simultaneously adopting the polarization-dependent lens and grating. The proposed system can convert the viewpoint according to the position of the eye pupil without mechanical movement. The polarization-dependent viewpoint switching can resolve the inherent problem of a narrow eyebox in retinal projection displays without employing the bulky optics for mechanical movement.

In conclusion, the dissertation presents the practical optical design and detailed analysis for enhanced WNED based on the polarization multiplexing technique through various simulations and experiments. The proposed approaches are expected to be utilized as an innovative solution for compact wearable displays.

Keywords: Augmented reality, near-eye display, waveguide, polarization multiplexing, geometric phase optic, holographic optical element, polarization grating, volume grating, retinal projection display

Student Number: 2016-20939

Contents

Abstract	i
Contents	iii
List of Tables	vi
List of Figures	vii
Chapter. 1 Introduction	1
1.1 Augmented reality near-eye display	1
1.2 Key performance parameters of near-eye displays	4
1.3 Basic scheme of waveguide-based near-eye displays	22
1.4 Motivation and purpose of this dissertation	33
1.5 Scope and organization	37
Chapter 2 Dual-focal waveguide-based near-eye display using polarization-dependent combiner lens	39
2.1 Introduction	39
2.2 Optical design for polarization-dependent combiner lens	42
2.2.1 Design and principle of polarization-dependent combiner lens	42
2.2.2 Prototype implementation	48
2.3 Waveguide-based augmented reality near-eye display with dual-focal plane using polarization-dependent combiner lens	51
2.3.1 Implementation of the prototype and experimental results	51
2.3.2 Performance analysis and discussion	57
2.4 Conclusion	69
Chapter 3 Extended-field-of-view waveguide-based near-eye display via polarization-dependent steering combiner	70
3.1 Introduction	70
3.2 Optical design for polarization-dependent steering combiner	73
3.2.1 Principle of polarization grating	73
3.2.2 Principle of polarization-dependent steering combiner	76
3.2.3 Analysis and verification experiment for real-scene distortion	77

3.3 Waveguide-based augmented reality near-eye display with extended-field-of-view	81
3.3.1 Field-of-view for volume grating based waveguide technique.....	81
3.3.2 Implementation of the prototype and experimental results.....	84
3.3.3 Performances analysis and discussion	87
3.4 Conclusion	92
Chapter 4 Viewpoint switchable retinal-projection-based near-eye display with waveguide configuration.....	93
4.1 Introduction.....	93
4.2 Polarization-dependent switchable eyebox	97
4.2.1 Optical devices for polarization-dependent switching of viewpoints	97
4.2.2 System configuration for proposed method.....	100
4.2.3 Design of waveguide and imaging combiner.....	105
4.3 Compact retinal projection-based near-eye display with switchable viewpoints via waveguide configuration	114
4.3.1 Implementation of the prototype and experimental results.....	114
4.3.2 Performance analysis and discussion.....	118
4.4 Conclusion	122
Chapter 5. Conclusion.....	123
Bibliography	127
Appendix	135

List of Table

Table 1.1 Summary of AR near-eye display depending on the imaging combiner and display type.....	34
Table 2.1 Specfication of implemented PDCL	49
Table 2.2 Specfication of fabricated PDCL	53
Table 2.3 Measured optical power and efficiency	62
Table 3.1 FOV performance of commercialized product or prototype	72
Table 4.1 Specifications of the fabricated waveguide system.....	113

List of Figures

Figure 1.1 Conceptual diagram of the see-through near-eye display.....	3
Figure 1.2 Angular resolution of the near-eye display.....	5
Figure 1.3 Conceptual diagram of modulation transfer function (MTF).	6
Figure 1.4 FOV of the near-eye display.....	8
Figure 1.5 (a) Trade-off between the FOV and resolution for near-eye displays for 1920 display pixels (FHD resolution). (b) Angular resolution depending on the number of the display pixels and FOV. Each dot line indicates a boundary satisfying the specific angular resolution.	10
Figure 1.6 Concept diagram of eyebox: (a) full-FOV condition, (b) reduced FOV condition, and (c) out of range condition.	11
Figure 1.7 Eyebox of the near-eye display using a floating lens. (a) Small divergence angle case and (b) large divergence angle case.	13
Figure 1.8 Accommodation of the human eye. (a) For a far target: the crystalline lens becomes thinner, focusing on far objects. (b) For a near target: the crystalline lens becomes thicker, focusing on near objects.	14
Figure 1.9 Schematic diagram of vergence-accommodation conflict (VAC) in 3-D displays.....	16
Figure 1.10 Schematic diagrams of (a) birdbath-type AR display system and (b) equivalent optical model with a curved mirror replaced by a virtual convex lens. (c) Simulation result: FOV variation according to size of the beam splitter.	20
Figure 1.11 Configuration of AR near-eye display using curved mirror.	23
Figure 1.12 Configuration of waveguide-based near-eye display.....	25
Figure 1.13 Schematic diagram of the reflection-type waveguide: (a) partial-reflective mirror array method (b) microstructure mirror array method.	26
Figure 1.14 Schematic diagram of the diffraction-type waveguide.	28
Figure 1.15 Schematic diagrams for several surface-relief gratings (SRGs): (a)	

binary grating, (b) binary slanted grating, and (c) triangular gratings.	29
Figure 1.16 Schematic diagrams for Bragg matching: (a) angular selectivity and (b) wavelength selectivity.	31
Table 1.1 Summary of AR near-eye display depending on the imaging combiner and display type.....	34
Figure 2.1 Focus cue in the conventional waveguide system: (a) Far-corrected retinal image for infinity focus, (b) near-corrected retinal image for near objects.	40
Figure 2.2 Geometric phase effect by closed path on the Poincaré sphere. The solid line (A→B, C→A) represents the polarization change by the QWP. The dot lines (B→C) represent different paths by the HWP with varying orientation, respectively.	44
Figure 2.3 Geometric phase optical element with spatially varying optical axis.	45
Figure 2.4 Illustration of GPL operations: (a) with a convex lens function and (b) with a concave lens function. The DC terms are neglected.	46
Figure 2.5 Illustration of the proposed PDCL structure and polarization states (a) for lens mode and (b) for optical window mode.	47
Figure 2.6 Photographs of the proposed eyepiece-combiner.	48
Figure 2.7 Examination of dual-focal functionality using the PDCL: (a) experimental setup, (b) captured image in optical window mode, and (c) captured image in lens mode.....	50
Figure 2.8 Schematic diagram of proposed waveguide-type AR near-eye display. A green line indicates the light for the real scene. Each blue and red line indicates the optical path for virtual images depending on the polarization state, respectively...	51
Figure 2.9 Schematic diagram of the recording setup for VHGs.	53
Figure 2.10 Experimental setup of proposed configuration on optical table.	54
Figure 2.11 Ray-tracing simulations for the 4- <i>f</i> lens system.....	55
Figure 2.12 Photographs of experimental results: (a) in lens mode, (b) in window mode, and (c) in integrated mode.....	56

Figure 2.13 (a) Eyebox definition for the WNED system. (b) Photographs of experimental setup for measuring eyebox.....	58
Figure 2.14 Schematic diagram of effective FOV (a) by the PDCL, (b) in window mode, and (c) in lens mode.	59
Figure 2.15 (a) Effective FOV for lens mode depending on the focal length of PDCL. (b) Ratio of image size between both operating modes.	60
Figure 2.16 Calculated diffraction efficiency of VHG with different polarization states of input beam. The output value is normalized by the result of TE mode. ...	63
Figure 2.17 (a) Schematic diagram of improved configuration with active optical elements. Improved PDCL structure and polarization states (b) for lens mode and (c) for optical window mode.	65
Figure 2.18 Schematic diagram of the modified PDCL structure and operating mode for triple focal planes.....	66
Figure 2.19 Chromatic aberration of GPHL: (a) simulation for focal spots and (b) measured focal length depending on the wavelength.....	68
Figure 3.1 FOV in the waveguide-based near-eye display.....	70
Figure 3.2 Schematic diagram of the LC-based Bragg polarization grating.....	73
Figure 3.3 Illustration of the polarization grating (a) with a right-handed circular polarization (RCP) and (b) with a left-handed circular polarization (LCP).....	75
Figure 3.4 Schematic diagram of the (a) PDSC structure and the polarization state (b) for real scenes and (c), (d) for the virtual image with different polarization states, respectively. The polarization grating is abbreviated as PG.	76
Figure 3.5 Ray tracing simulation layout and results for the real scene. By deactivating the polarization grating, the simulation is performed for the case without PDSC. (a) The optical path through the PDSC and waveguide. (b) The position of the focal point on the retina in the cross-section. The marked lines indicate the optical path to the retina. By inserting the PDSC, a lateral shift of the focal spot (Δ) occurs. (c) The intensity map of the focal spot on the retina. The polarization grating is abbreviated as PG.....	78

Figure 3.6 Simulated MTF curves of the proposed system for a real object.....	79
Figure 3.7 Photographs of experimental results: the captured target image and the line profile of the intensity across the dot arrow lines.	80
Figure 3.8 k -vector diagram of the reflection-type VHG. (a) Rightmost incidence condition and (b) leftmost condition under the TIR regime.....	81
Figure 3.9 Benchtop prototype of proposed configuration. Arrow lines indicate the optical path of beams.	84
Figure 3.10 Experimental results: (a) without the PDSC (conventional system), (b) with the 5° PDSC, and (c) with the 10° PDSC. The red dot lines indicate the blank image area.	85
Figure 3.11 (a) Diffraction efficiency of the recorded VHG with two orthogonal linearly polarized input beams, respectively. (b) Output efficiency comparison before and after compensation when the 10° PDSC is adopted.	86
Figure 3.12 (a) Experimental setup for distortion verification. (b) Captured screen images and difference image between the original and the case with a polarization grating.	88
Figure 3.13 Diffraction angle of a polarization grating depending on the incidence angle.	89
Figure 3.14 MTF degradation for virtual images: (a) beam divergence by finite pixel size, (b) simulation with a 10° polarization grating and HD-resolution LSP with a 40° diverging angle.....	90
Figure 3.15 Simulation results of the image distortion for virtual images depending on the PDCL and polarization grating.....	91
Figure 4.1 (a) Simplified configuration of the retinal projection display. (b) Illustration of retinal images according to pupil movement.....	94
Figure 4.2 (a) Schematic diagram of the retinal projection-type near-eye display using an LHOE. (b) Illustration of the double image problem with a narrow viewpoint spacing and (c) blank image problem with wide viewpoint spacing in the RPD with multiple viewpoints.	96

Figure 4.3 Spatial distribution of the angular resolution depending on the incidence angle of the input beam (θ). In the free-space propagation method, the incidence angle toward the center point of the LHOE (C) is changed to provide the dynamic eyebox. The simulation is conducted under the following conditions; θ : $40^\circ \sim 90^\circ$, LHOE lateral size: 19 mm, eye relief: 20 mm, and divergence angle of the light source: 30° 98

Figure 4.4 Schematic diagram of the angular-multiplexed out-coupler; the output beam is selectively diffracted depending on the guiding angle, which is presented in different colors.99

Figure 4.5 Illustration of the composition of the PDEL and operating mode depending on the polarization state; (a) lens mode for virtual images and (b) optical windows mode for real scenes. 100

Figure 4.6 Schematic diagram of the proposed configuration. Each red line shows a beam path with LCP, and each blue line shows a beam path with RCP. The LCP and RCP are controlled by polarization. 101

Figure 4.7 Optical misdesign classification. The simulation results are obtained by changing the size and position of the imaging combiners or the diffraction angle using ray-tracing software (LightTools). 103

Figure 4.8 (a) Eyebox expansion by steering of the input light source in the wedge-shaped lightguide. (b) Focal spot is shifted by inducing Bragg mismatching condition. The simulation results show that the lateral shifted distance of the focal spot is 1.2 mm in a leftward direction and 1.3 mm in a rightward direction based on half of the original FOV. The simulation condition is as follows: the thickness of lightguide is 7 mm, the slanted angle of the wedge is 60° , and eye relief is 20 mm. 104

Figure 4.9 Trade-off relationships between design parameters..... 106

Figure 4.10 Schematic diagram of the VHG's constraint: the VHG's diffraction efficiency according to the incidence angle (angular selectivity). 107

Figure 4.11 Optimized results of allowable guiding configurations: (a) positional difference (Δ_p) between the two projected beams on the out-coupler, (b)

longitudinal length of the waveguide, and (c) effective FOV changed by misalignment of the two guiding beams. The blue dot lines indicate the value used in the prototype. 110

Figure 4.12 Simulation results: (a) the spacing between two viewpoints according to the output angle θ_o . The solid line indicates the pair of output angles with 4 mm spacing, which are target conditions in this experiment. (b) The FOV decrement according to the output angle. The dotted lines indicate reduced FOV variations at selected conditions in this experiment. 112

Figure 4.13 2-D layout of the designed waveguide system in LightTools. Each solid line is a ray path. Simulation result for input beam with (a) RCP mode and (b) LCP mode..... 113

Figure 4.14 (a) Schematic diagram of the automatic VHG recording system. (b) Recording angle for the multiplexed VHG. 115

Figure 4.15 Experimental results for focal spots according to polarization of input beam. The grid paper is placed at the eye relief distance (22.5 mm). 116

Figure 4.16 Prototype of the proposed configuration..... 117

Figure 4.17 Photographs of experimental results; (a) AR scene of the rendering test circle image with real FOV target, (b) virtual image with maximum FOV, (c) printed driving screen image (real object), (d) virtual information images and (e) AR scene for simulated driving..... 118

Figure 4.18 Experimental results: (a) with different focus depths of the camera, (b) at different viewpoints..... 119

Figure 4.19 MTF results of the prototype system. The marked circle indicates measured values and the solid line indicates interpolated MTF curve using curve fitting. 120

Figure 4.20 Simulation results of the polarization state along the optical path; (a) input beam with circular polarization, (b) diffracted beam by in-coupler, (c), (d), (e) guided beam according to TIR number, and (f) output beam extracted by out-coupler where φ_i is the inclination angle and e_i is the ellipticity. 121

Chapter. 1 Introduction

1.1 Augmented reality near-eye display

Humans most rely on vision among the various senses that provide information about our surrounding environment. According to the statistical data, about 70% of human sensory receptors are concentrated in the eye, and about 80% of the information is mediated through vision [1]. Before the advent of the electrical display devices, most of the visual information was obtained through paper books. However, since the 1990s when the display technology began to rapidly develop, it was possible to acquire vivid and colorful image information through display devices such as television and mobile phones. Recently, the flat panel display technology with an ultrahigh-resolution has been developed rapidly and the state-of-the-art display technique can support the hyper-realistic and ultrahigh-definition image corresponding to the highest acuity for vision [2].

However, traditional displays reproduce only two-dimensional (2-D) flat images, which cannot provide realistic three-dimensional (3-D) visual information, including depth information. In order to render a virtual object on a 3-D space according to the observer viewpoint, various 3-D display techniques such as integral imaging, multi-view, volumetric, and holographic display have been studied. Except for a holographic display that can reproduce a wavefront identical to a real object, most 3-D display methods use 2-D flat displays to display a 3-D image by binocular parallax, which is called a stereoscopic display [3]. The stereoscopic technique should require an additional optical device, such as eyeglasses or a lenticular lens, to give different images to each left and right eye, which can cause degradation of the display performance. The 3-D display had a huge boom after the ‘Avatar’ movie released in 2009, but has been on a steady decline due to the lack of remarkable 3-D contents and convenient 3-D display system. In recent years, it became possible to produce readily high-quality 3-D

images due to the rapid development of computer graphics and cameras. In addition, as mass production of small-sized display panels with a high-resolution becomes possible, 3-D displays can be transformed into different form factors from traditional ones, thereby have market competitiveness, and have drawn public attention. This new type of 3-D display is the near-eye display.

The near-eye display refers to a wearable display device having a display right in front of the eyes, which is called by various appellations such as a head-mounted display (HMD), eyeglasses-type display (EGD), and face-mounted display (FMD) according to the wearing concept. The near-eye displays provide the user not only with a simulated environment that completely replaces the real environment, but also enhanced computer-generated perceptual information superimposed on the real objects. Depending on whether it is combined with the real environment, the former is referred to as virtual reality (VR), while the latter is augmented reality (AR). Especially, the application range of the AR near-eye displays is expected to be limitless because it can be utilized in daily life, such as industries, communications, education, automobile, and entertainment. For this reason, the AR near-eye display is spotlighted as the portable next-generation electronic device following the smartphone.

Figure 1.1 represents the optical architecture of the see-through near-eye display based on the stereoscopic vision. The detailed structure depends on the various combiner techniques, but the overall optical system can be categorized into three main parts: a display light source, imaging optics, an imaging combiner. First, the display module reproduces a virtual image. Second, the imaging optics magnifies the virtual image or delivers it to the eyes sharply. Finally, the image combiner is the core element of the AR near-eye display, which provides users with an AR environment that combines virtual images and real scenes. The optical combiner should transmit the lights for real objects without distortion and effectively control the lights for virtual images. The various optical combiner

architectures are introduced, such as a beam splitter, curved reflector, arrayed reflectors, diffractive optics, and freeform optics.

The display performances for AR environments are determined by the structure and specifications of these optical systems, and trade-offs between them arise by given system parameters. It is very challenging to break these trade-offs. Today many researchers endeavor to upgrade the various optical configurations of AR near-eye displays and to overcome the trade-off relationships between the optical performances.

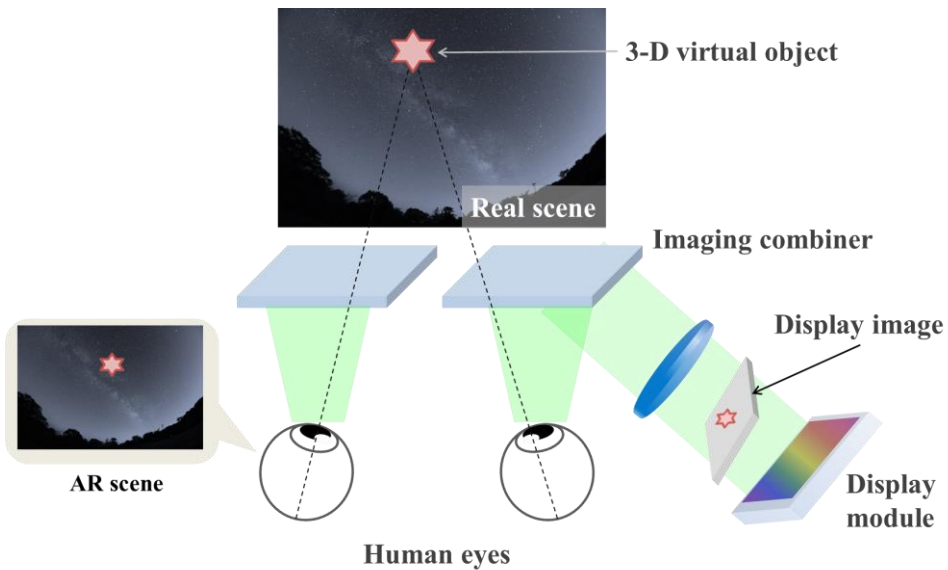


Figure 1.1 Conceptual diagram of the see-through near-eye display.

1.2 Key performance parameters of near-eye displays

Near-eye displays have many requirements and limitations for commercial product design because they must be wearable and compact. Therefore, near-eye displays should be considered for more complex and many performance parameters compared to 2-D flat panel displays. First, high-quality optical performance is required for a realistic and immersive experience. In addition to the binocular parallax, additional depth cues should be conveyed to enhance natural visual perception. Second, the form factor of the device is vital factor for comfortable wearing and exterior design.

Various design parameters for the near-eye display are complicatedly linked with each other. There is a trade-off between most design parameters under the condition that the display source and the configuration are determined. Many researchers are striving to improve display performances and break through trade-off relationships. In this section, representative performance parameters for the near-eye display will be briefly summarized.

The first key parameter is the display resolution of the virtual scene. In traditional flat-panel displays, the resolution is simply presented in terms of the number of horizontal and vertical pixels. Since the distance between the display and the observer is not fixed, the resolution has been simply expressed with the number of pixels. With the development of near-field display devices such as smartphones, pixel density such as pixels per inch (PPI) unit has become more critical than a pixel number. As the number of pixels per unit area increases, the sharpness of the display image increases.

In near-eye displays, the distance between the viewer's eyes and the floating image plane is fixed. Therefore, the spatial resolution (display density) can be simply converted to angular resolution. Angular resolution is suitable for designing the near-eye display considering the visual acuity of the human eye. Figure 1.2 shows the angular resolution for the near-eye display that is defined as the number

of the pixel-pair per unit angle ($\Delta\theta$) in a unit of cycles per degree (cpd) as follows:

$$\text{Angular resolution (cpd)} = \frac{1}{\Delta\theta \text{ (deg)}}. \quad (1.1)$$

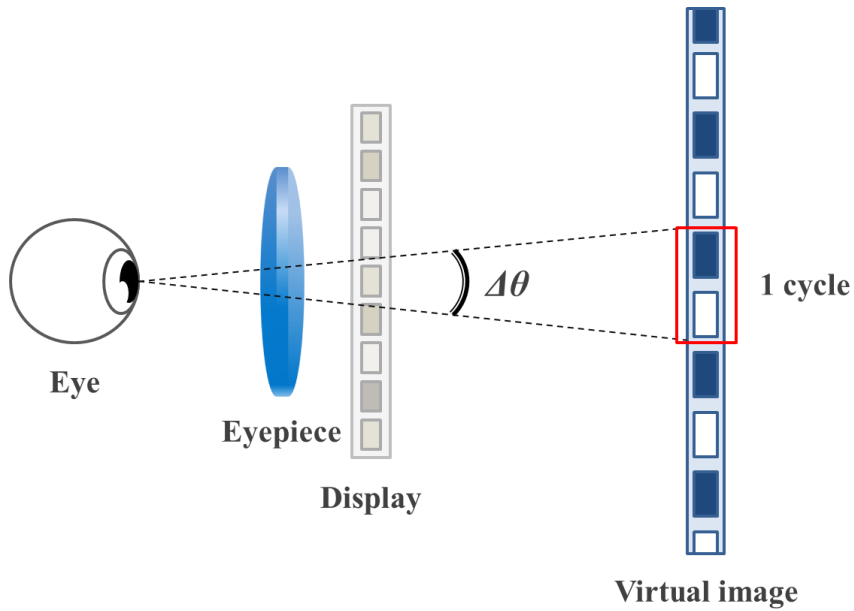


Figure 1.2 Angular resolution of the near-eye display.

The angular resolution represents the highest resolution of the virtual image that can be rendered by the display source. However, in the real application cases, the unit pixel of the floated image is not physically separated precisely like the actual display panel. In addition, the image quality can be deteriorated by the diffraction and distortion of various optical elements, and thus the contrast of the virtual image may be degraded. Since the angular resolution defined by Eq. 1.1 may differ from that of the existing system, it is more common to use *modulation transfer function* (MTF) to evaluate the sharpness of the image. MTF is a quantitative indicator of the relative contrast of the imaging system at a given spatial frequency, similar to the *spatial frequency response* (SFR) [4].

MTF can be obtained in two different methods. In the first method, MTF is derived from calculating the contrast for the periodic patterns as follows:

$$C(f) = \frac{I_{\max} - I_{\min}}{I_{\max} + I_{\min}}, \quad (1.2)$$

$$\text{MTF}(f) = \frac{C(f)}{C(f_0)} \times 100\%, \quad (1.3)$$

where f is the spatial frequency, I is the intensity or luminance of the periodic pattern, and $C(f_0)$ is the background contrast at the lowest spatial frequency for the normalization. Figure 1.3 shows the contrast-based MTF results from using bar patterns.

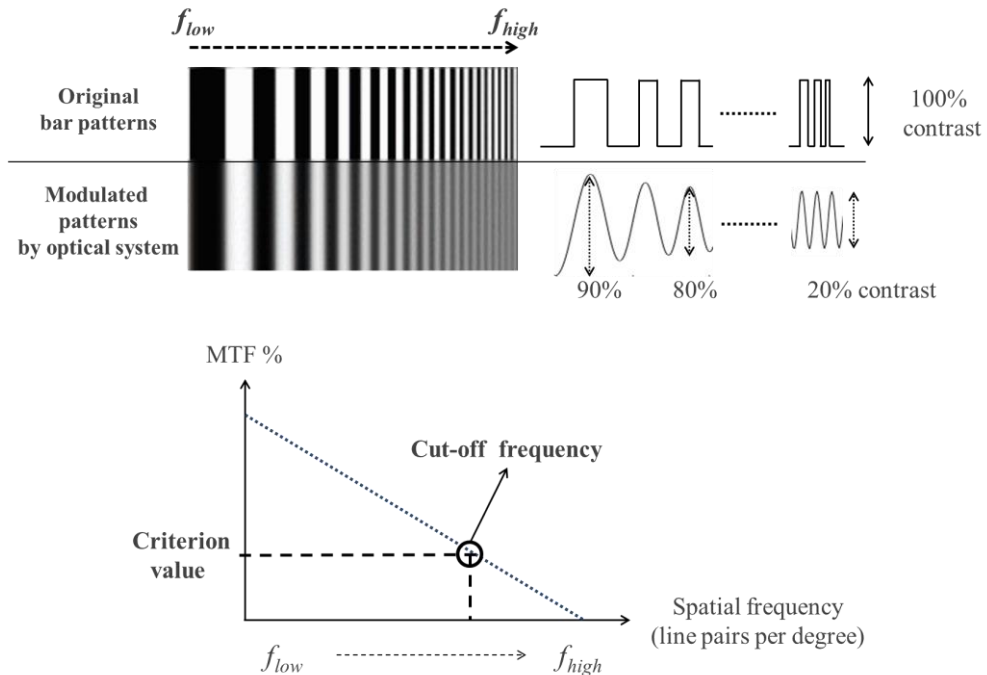


Figure 1.3 Conceptual diagram of modulation transfer function (MTF).

As shown in Fig. 1.3, the MTF chart indicates the contrast degradation by the optical system depending on the spatial frequency. The minimum resolvable distance that can distinguish two adjacent pixels is determined based on a specific criterion, which is called a cut-off frequency. The standard used in the imaging system is the Rayleigh criterion that implies 9% of MTF contrast [5]. In the display field, a higher criterion value of 20% is often used [6]. The resolution of the optical system becomes improved as the cut-off frequency becomes increased, and then a sharper image can be provided.

Second, MTF can be calculated as the modulus of the Fourier transform of the *point spread function* (PSF) as follows:

$$\text{MTF}(f_{x,y}) = |\mathcal{F}\{PSF(x, y)\}| = |\mathcal{F}\{h(x, y)\}|, \quad (1.4)$$

where x and y are the spatial distance, and $h(x, y)$ is the *impulse response function*, namely the PSF in the optical imaging system, which is considered as a linear system. In such a linear imaging system, an output result can be obtained using a transfer function in the following equation:

$$o(x, y) = i(x, y) \otimes h(x, y), \quad (1.5)$$

where $o(x, y)$ is the output image (virtual image), $i(x, y)$ is the input image (display image), and \otimes is the convolution operator. Since most of the displays typically have the same vertical and horizontal resolution, it is suitable to reduce the 2-D resolution to one dimension (1-D). 1-D PSF is defined as the *line spread function* (LSF) and can be obtained as follows:

$$LSF(x) = \int PSF(x, y) dy. \quad (1.6)$$

To obtain the MTF curves, the PSF or LSF of the optical system should be measured, which can be obtained in various methods such as a single-pixel imaging-based measurement or slanted edge method (ISO-12233 standard) [7,8]. Visual acuity of the human eye is roughly 30 cpd (i.e., 20/20 vision) [9]. The angular resolution of the virtual image is required to be higher than 30 cpd for incognizance of the pixelated image. For wide viewing conditions, enormous pixels must be supported to fulfill the visual acuity. An ultrahigh density micro-display over 4K has currently been under development for near-eye displays [10].

The second performance parameter is field-of-view (FOV). The FOV is the extent of the observable image that is displayed for a fixed gaze direction. Note that eye rotations or movements are excluded in this definition. The FOV is expressed in units of distance or angle and is generally defined by the angle to correlate with the eye's resolution in near-eye displays easily. Therefore, it is called the angle of view in another word. Figure 1.4 shows the 1-D FOV for a virtual scene.

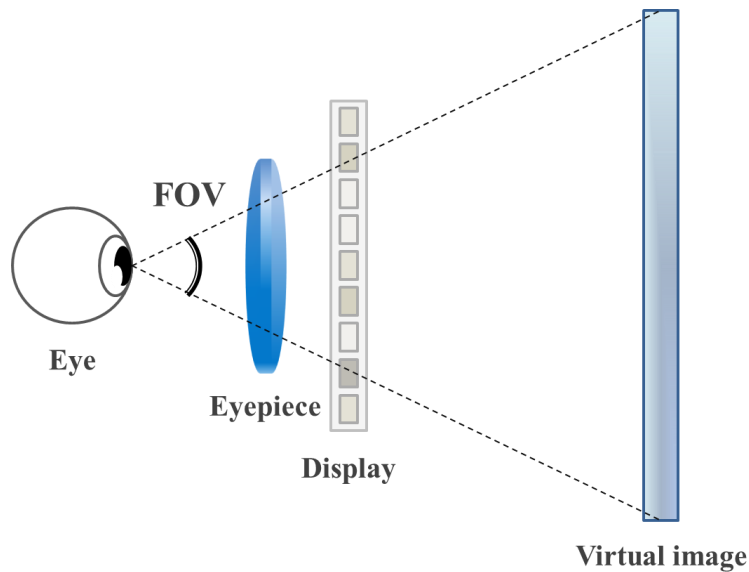


Figure 1.4 FOV of the near-eye display.

The FOV of a human eye is about 150 degrees in monocular vision and 114 degrees in binocular vision [11], horizontally. To provide full immersion for virtual environments, the FOV of near-eye displays should satisfy this criterion. VR near-eye displays consist of a relatively simple optical system, which is advantageous for providing a wide FOV. Over recent years, the released VR headsets have a FOV over 110 degrees [12], which meets the binocular FOV vision. However, AR near-eye displays are excruciatingly challenging to achieve these FOV requirements at the current technical level. Most commercial AR devices have a FOV of less than 60 degrees [12]. The visual field is subdivided according to the characteristics of the object to be recognized, and the technical level of the near-eye display is classified as follows. First, in the low-FOV regime (less than 30 to 40 degrees), it provides concentrated visual contents including text or simple graphics information. Second, in the mid-FOV regime (40~60 degrees), visual information, including partially the peripheral vision, can be delivered comfortably. The mid-FOV near-eye display is appropriate for artificially visualizing information that is useful in real life. Thirdly, wide-FOV designs (higher than 60 degrees) are potentially applicable for applications requiring immersion such as simulation and training for exquisite works. Currently, many researchers in the industrial and academic fields are engrossed in AR devices that provide a wide-FOV for a visual comfort zone.

The conventional near-eye displays have a trade-off between FOV and angular resolution, which is calculated as follows:

$$\text{FOV (deg)} = \frac{N}{2 \cdot \text{Angular resolution (cpd)}}, \quad (1.7)$$

where N is the number of pixels of the display. Consequently, the FOV is inversely proportional to the resolution for a given display source, as shown in Fig. 1.5(a).

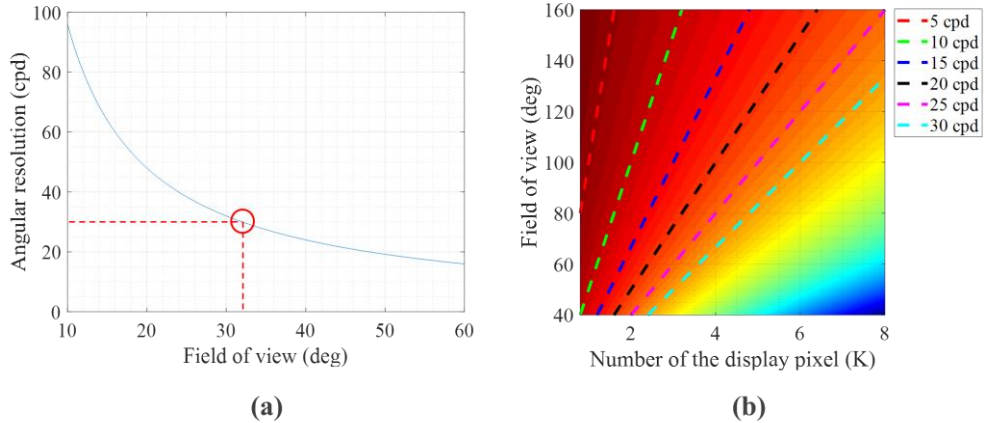


Figure 1.5 (a) Trade-off between the FOV and resolution for near-eye displays for 1920 display pixels (FHD resolution). (b) Angular resolution depending on the number of the display pixels and FOV. Each dot line indicates a boundary satisfying the specific angular resolution.

To satisfy the human visual acuity (30 cpd), the FOV is narrowed to about 32 degrees for FHD resolution. The resolution of the display must exceed 6.6K to provide a wide FOV over 110° simultaneously and a high resolution of 30 cpd for monocular vision, as shown in Fig. 1.5(b). The high-level resolution of a commercialized micro-display is around 2K ~ 4K, which is insufficient to meet human visual acuity. Consequently, a wide-FOV device often suffers from inadequate resolution. In addition, the FOV is a restraint on the configuration of the optical system, such as clear aperture, eye relief, and vignetting. The clear aperture of the optical elements determines the effective size of the virtual image. Since the clear aperture diameter is directly related to the size of the optics, there are limits to enlarge the aperture for improving the angle of view. Eye relief is the distance between the last surface of an eyepiece optic and the observer's eye. For a virtual image floating at a fixed focal plane, the FOV increases as the eye relief become shorter. However, a moderate eye relief (about 15~20 mm) should be required for comfortable use [13] or securing the object distance.

As previously mentioned, the FOV is a crucial factor for immersive experiences and is affected by various parameters that are in a trade-off relationship. When designing the near-eye display, an optimized FOV should be adopted in consideration of various parameters. For breaking through the trade-off problem, novel optical devices or methods are employed. In the third chapter of this dissertation, a novel type of AR waveguide-based near-eye display will be proposed to extend the FOV.

The third performance parameter is the eyebox. The eyebox refers to an area where the user can fully or partially observe the virtual image, as shown in Fig. 1.6. In general, the eyebox is defined as the physical movement range in a 2-D frontal plane at a specific depth position (i.e., eye relief). The eye pupil should be located within the eyebox to perceive the virtual image with full FOV or reduced FOV.

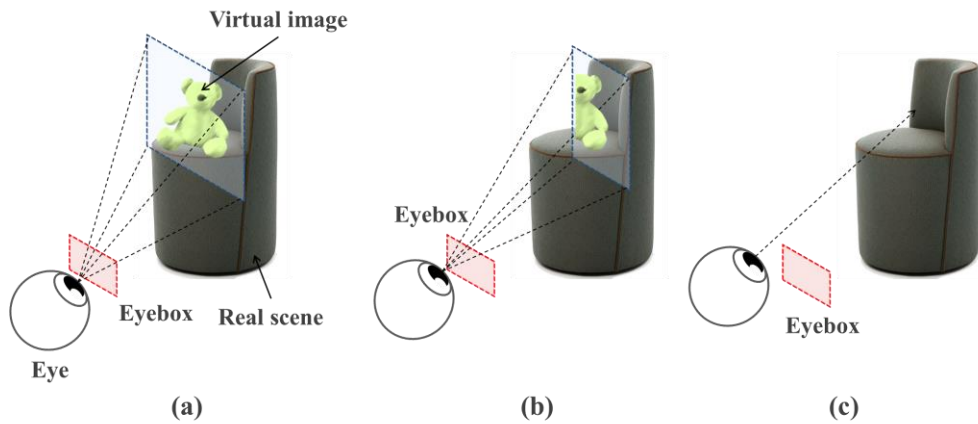


Figure 1.6 Concept diagram of eyebox: (a) full-FOV condition, (b) reduced FOV condition, and (c) out of range condition.

The eye pupil may get out of the eyebox due to the device movement by the head sway or the eyeball rotation by changing the gaze direction. Eyeballs typically rotate from 15 degrees to 30 degrees in daily life [14], which is a pupil movement of approximately 6 to 11 mm at an eye relief of 20 mm. In addition, an eye position or inter pupil distance (IPD) has individual variations due to their facial structures. In order to provide a comfortable viewing condition even in these various environmental variables, it is recommended to design the eyebox with at least 10 mm or more [15].

The eyebox is decided conclusively by the combiner technique of the near-eye display and design parameters with a trade-off relationship. For a hologram display using a spatial light modulator (SLM), the eyebox has a compromise with the FOV, which is called etendue [16]. The product of the eyebox size and the FOV is constant and proportional to the SLM's pixel number. For an imaging system using a floating lens, the eyebox is closely related to the divergence angle of the light source. If the divergence angle increases, the eyebox also increases because the overlapping area where the light bundle corresponding to each pixel is incident is widening, as shown in Fig. 1.7. Conversely, if the divergence angle decreases, the eyebox and effective FOV becomes smaller due to the vignetting effect.

Recently, researches on the eyebox extension with large FOV are intensively investigated. The extended eyebox scheme can be usually implemented using an eye-tracking technique. This method is to find the position of the shifted pupil using the pupil-tracking and then relocate the eyebox to the corresponding position. In addition to the pupil-tracking method, an eyebox duplication method that generates multiple viewpoints has been proposed to provide an enlarged eyebox. These eyebox expansion technologies can secure a comfortable viewing condition by breaking through the trade-off relation. In the fourth chapter of this dissertation, a novel method of eyebox expansion will be proposed.

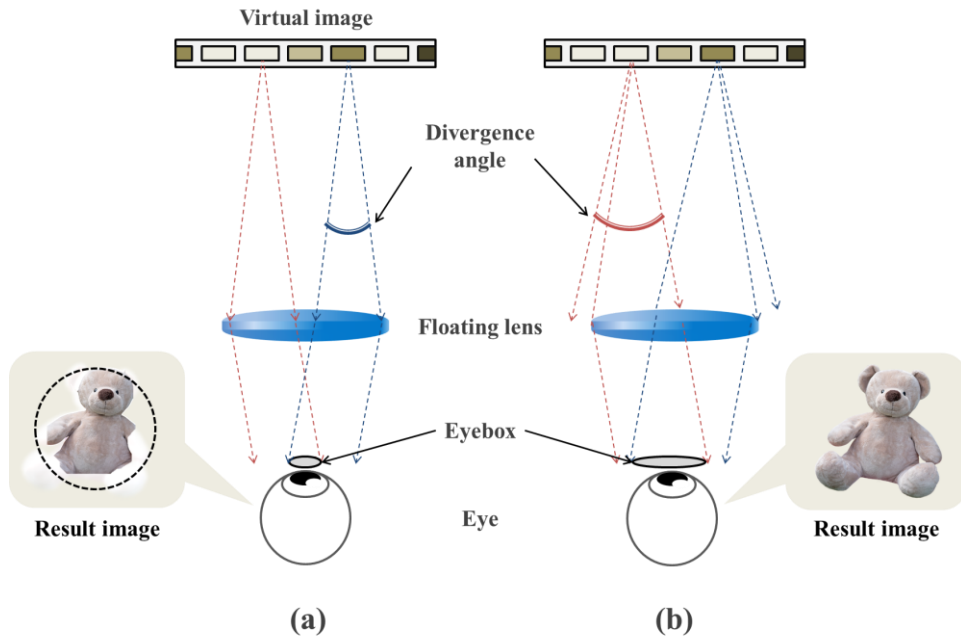


Figure 1.7 Eyebox of the near-eye display using a floating lens. (a) Small divergence angle case and (b) large divergence angle case.

The fourth key parameter is the focus cues. The focus cues refer to both the accommodation cue and the retinal-image blur effect. These two phenomena simultaneously occur by changing the eye focus in real life. The accommodation cue refers to the focus response of the eye, where ciliary muscles modulate the thickness and curvature of the crystalline lens. The blur effect of the retinal-image is minimized by the focus adjustment, and humans can observe a sharp image, as shown in Fig. 1.8.

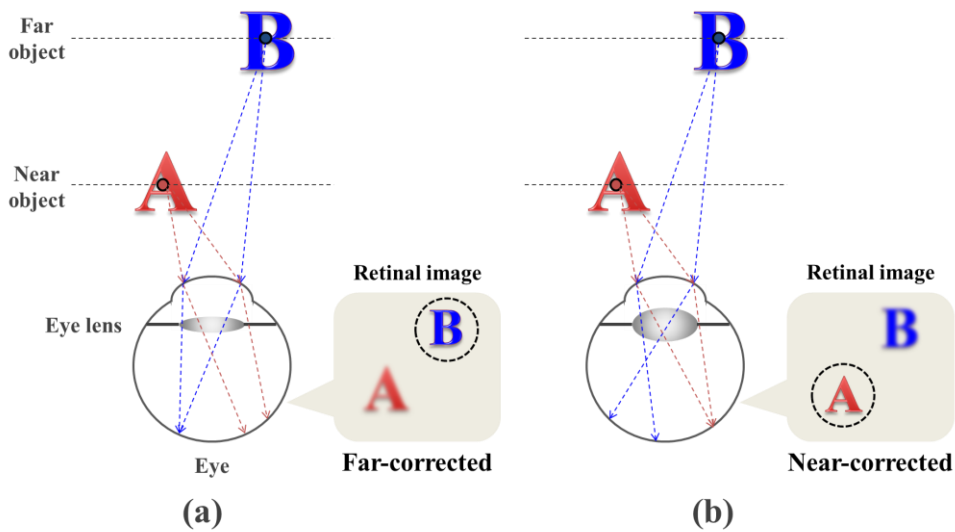


Figure 1.8 Accommodation of the human eye. (a) For a far target: the crystalline lens becomes thinner, focusing on far objects. (b) For a near target: the crystalline lens becomes thicker, focusing on near objects.

The focus cues enable the depth perception that is the ability to distinguish the distance of 3-D objects, along with other depth cues such as binocular disparity (stereopsis), convergence, motion parallax, perspective, relative size, occlusion, and shading [17]. The focus cue is more powerful than other depth cues, especially when discriminating against the depth of near-field objects within 10 m [18]. A diopter (denoted as D or dpt), which is a measurement unit of the optical power of a lens, is widely used to indicate the focal power or object distance and is simply the inverse of the focal length in meters. The blur extent in the retina-image is affected by the limited depth-of-field (DOF) of the eye. For normal eyes and optimal conditions, the DOF is known to be ± 0.3 D at a pupil diameter of 3 mm [19]. In other words, when we see an object that is more than 0.3 D different from the focal power of the eye, a blurred object is perceived. The accommodation response occurs within 100~300 ms in normal environments.

Vergence (convergence) is the simultaneous movement of both eyes to obtain

the binocular vision. Depending on the object's position, the degree of rotation of both eyes is adjusted to provide projected images in the retina center of both eyes. The vergence eye movement is triggered by differences between the retinal images in both eyes (i.e., binocular disparities). Vergence is an essential and dominant depth cue for depth perception, closely correlated with an accommodation cue. When adjusting the vergence angle of both eyes to see objects at a different distance, the focal power of the eye will automatically change, which is known as the accommodation reflex. Therefore, accommodation and vergence cue always coincide when staring at objects in the real world.

Binocular vision is a very effective source to represent three-dimensional objects and has been used mainly in 3-D displays. In the near-eye display, the stereoscopic image based on the binocular disparity can be easily displayed by the left-channel and right-channel separated display modules, compared to typical 2-D flat-panel displays that require additional optical elements or system. In the VR applications, 3-D virtual objects or environments are constructed for 3-D vivid immersion experiences. In AR applications, the virtual image has to be aligned to the real object. Augmented information well rendered in consideration of binocular disparities is observed at the same distance as the targeted real object. However, the focal plane of the virtual image is still fixed at the specific depth determined by the optical configuration. This discrepancy between the focal distance of the real object and virtual images may hinder a sharp and clear image. Furthermore, the vergence distance by the binocular disparity and accommodation distance by the optical system may be mismatched, which is the vergence-accommodation conflict (VAC), as illustrated in Fig. 1.9.

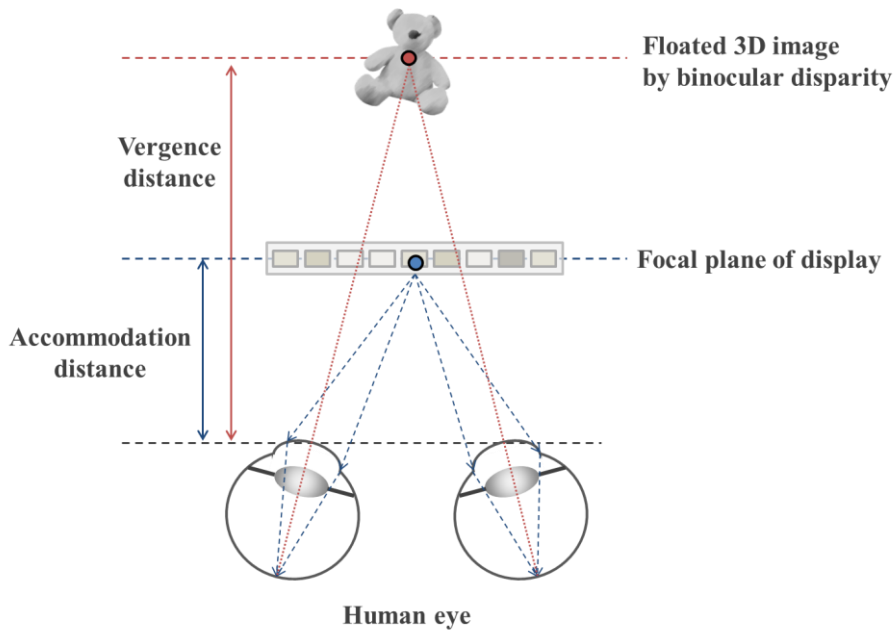


Figure 1.9 Schematic diagram of vergence-accommodation conflict (VAC) in 3-D displays.

The VAC problem may restrict comfort experiences in stereoscopic viewing conditions and may provoke various adverse effects such as visual fatigue, nausea, vertigo, and frequent eye-blink [20-22]. Especially, the VAC problem becomes a more critical issue in AR applications where a coincidence of real objects and virtual images is important. Various methods inducing the accommodation cues have been proposed to mitigate the VAC issue, and are presented in [23]. By resolving the VAC issue, discomfort or blurred vision can be alleviated compared to a conventional system with a single focal plane.

An intuitive approach to solving the VAC problem is to shift the focal plane dynamically according to the vergence distance of the 3-D image. This approach requires a focus-tunable technology to control the focal depth. Many researches proposed near-eye displays with multiple focal planes using a focus-tunable optical element, such as liquid lens, liquid crystal (LC) lens, and membrane mirror. A variable structure system is suggested to change the position of the display using a

motorized stage. Multi-focal displays can provide a wide range of comfort zone with quasi-continuous focus cues. In order to reconstruct a volumetric scene with corrected focus cues, a high-speed operating system with faster than real-time (30 Hz) should be required. With the rapid development of the optical device, it has become possible to provide extremely dense focal planes using a DMD (digital micro-mirror device) with ultra-high actuation frequency (up to 32000 Hz). However, several limitations still exist, such as form factor and driving circuit, to be employed to the near-eye display system.

A varifocal display is an alternative to the multi-focal display, which can provide a focus-corrected image only at a specific depth plane using a gaze-tracking technique. The natural scene is allowed by digital image processing that blurs virtual images except for the single focal depth where the eye is staring. This method requires both accurate gaze-tracking and fast image processing technology.

Holographic display, which has been considered as one of the ultimate 3-D display technologies, is another method to support focus cues. The holography technique can reproduce the wavefront of a real object using complex wavefront modulation and interference of coherent light. In the digital holography, a 3-D virtual image can be rendered by wavefront modulation using an SLM, which provides the same natural depth cues as the real object. However, holographic displays have several intrinsic problems. The hologram rendering is extremely difficult to be realized in real-time by a heavy computational load in calculating the computer-generated hologram (CGH). Coherent light sources may cause speckle noise, which not only deteriorates the image quality but also could be potentially injurious to the human eye [24]. In addition, the pixel pitch of the SLM should be very narrow to the wavelength of light for a wide angle of view, which is very challenging. Due to these limitations, radical improvements for the overall system are required to commercialize holographic displays.

The fifth performance parameter is optical efficiency. The optical efficiency is

calculated as the ratio between the energy amount of the input beam (display light source) and that of the output beam at the eyepiece. In VR near-eye displays, since the light emitted from the display passes through a simple optical system such as an eyepiece lens, the drop in optical efficiency remains relatively low. In particular, HMD-type VR systems do not require a high-level of brightness because they completely shield the user's eye from the external scene.

In contrast, in AR systems, optical efficiency may be dramatically reduced by complex optical structures. A beam splitter (half mirror) used as the imaging combiner splits the input beam into two paths, which inevitably decreases the optical efficiency. Representative optical elements such as diffractive optics, polarizing optics, and thin-film coating devices that are widely used in the near-eye display also have a limited efficiency for the incident beam. A considerable reduction in efficiency due to the cascaded optical elements deteriorates the visibility of the virtual image.

Most commercialized AR devices suffer from luminosity issues that the brightness of the display light source is insufficient compared with real scenes. To improve the contrast between real and virtual images, a light-blocking coating is applied on the outer surface of the eyepiece module. Despite this shielding, it cannot compete with bright outdoor surroundings, which is 10 to 100 times brighter than an indoor room [25]. The brightness of the smartphone display is 500 to 1000 cd/m^2 (nits). The light source of AR displays that is at least ten times brighter than this specification is required to observe the AR scene outdoors smoothly. Considering the efficiency drop by optical elements and combiner, the brightness of the light source should be improved by 2-10 times or more. This ultra-bright light source becomes technically complex and challenging with power consumption, high dynamic range, heat cooling, and cost. Since it is difficult to achieve these high-level requirements with a flat-panel display, research on a micro-LED based display or a projection display using a laser diode light source

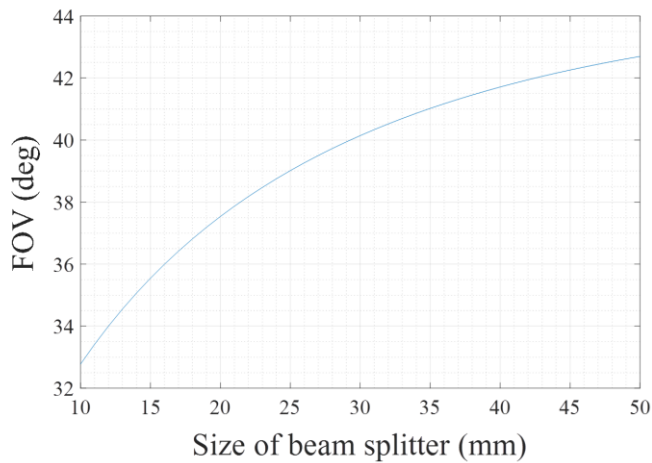
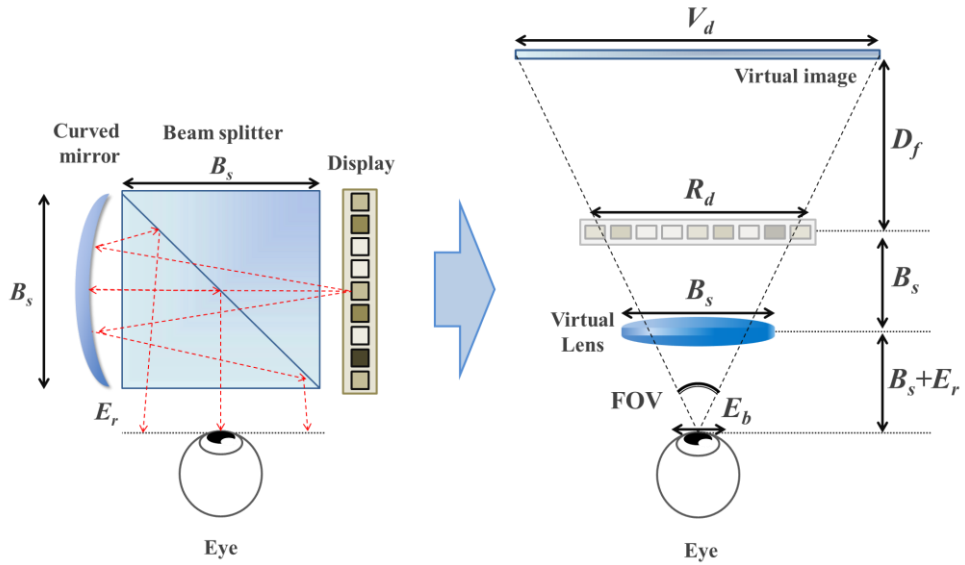
have been conducted intensively.

The last performance parameter is the form factor. The form factor is the most crucial design parameter for the commercialization and popularization of AR/VR near-eye displays. The form factor should be considered in two categories: physical dimensions (size and weight) and shape of the hardware structure. First, the compact form factor system with high-performance is a major challenge in AR/VR applications. If the device is bulky and heavy, users may feel uncomfortable for a long-term wearing condition. The size and weight of the devices have gradually been decreased by adopting state-of-the-art display and optics. However, optical performance and form factor are typically interdependent. The near-eye display system generally becomes complicated or bulky to improve the aforementioned optical performance.

For example, we suppose a birdbath-type see-through near-eye display consists of a display panel, a curved mirror, and a semi-transparent mirror (beam splitter), as illustrated in Fig.1.10(a). For a simple situation, the distances among the beam splitter and the display and mirror are neglected and the maximum size of the display and mirror is the same as the beam splitter. The imaging distance (D_f), eye relief (E_r), and eyebox (E_b) are generally fixed parameters for a comfortable viewing condition. The effective display size (R_d) considering the vignetting effect and field-of-view (FOV) is calculated as follows:

$$R_d = \frac{B_s \cdot (B_s + E_b)}{B_s + E_r}, \quad (1.8)$$

$$\text{FOV} = 2 \tan^{-1} \left(\frac{D_f \cdot R_d}{2B_s \cdot (D_f + 2B_s + E_r)} \right). \quad (1.9)$$



(c)

Figure 1.10 Schematic diagrams of (a) birdbath-type AR display system and (b) equivalent optical model with a curved mirror replaced by a virtual convex lens. (c) Simulation result: FOV variation according to size of the beam splitter.

Figure 1.10(c) illustrates the trade-off relation between FOV and form factor through the equation above. In order to secure a wide FOV, the size of the beam splitter should be increased, which makes the system bulky and heavy.

As previously discussed, the reduction in form factor is inevitably restricted to

provide high-level visual experiences. Most conventional AR/VR devices can be categorized into two primary categories: bulky HMD-type devices with high-performance and lightweight glasses-type devices with low-performance. The standalone HMDs can offer an immersive experience but are heavy and bulky due to a high-performance computing device, multiple sensors, and a battery in addition to optical devices. Meanwhile, glasses-type devices can connect with a smartphone or mobile device, reducing the computing load and sensors. However, it is challenging to interact with real objects in the mixed-virtual environment due to downsized system specifications. In conclusion, miniaturizing the device while maintaining good optical performances is the key to success for near-eye displays.

Second, the shape should give a comfortable fit for the user's facial structure. Improperly designed devices may pressure the user's nose or sides of the head, causing discomfort and dizziness. Additionally, the features of the near-eye display should be designed to be more visually attractive. The exterior design factor is a more important concept in AR devices than VR, which has been mainly used in the private or disconnected space from the outside. To gain more popularity to the public, it is necessary to provide various designs, such as fashionable sunglasses or spectacles, so that consumers can decide on a style according to personal preference. This dissertation is focused on improving the optical performance of a waveguide-based near-eye display with a compact form factor.

1.3 Basic scheme of waveguide-based near-eye displays

With the rapid development of display technology, high-definition and vivid images can be easily accessible. Beyond high-quality 2-D images, a demand for a 3-D visual experience has been steadily raised. Also, people tend to pursue more intuitive and immediate visual perception. AR/VR technology is a great solution to these needs, which is expected to change lifestyle more conveniently and productively. In addition, a recent building of 5G wireless networks and an explosive increase in virtual conferences due to the COVID-19 are accelerating the popularization of AR/VR technologies. The global market for AR/VR applications is expected to grow to 1.5 trillion U.S dollars by 2030 years [26].

A near-eye display system is an essential device for implementing immersive AR/VR experiences. As described in the previous chapter, the near-eye display should be designed to meet essential requirements by properly adjusting various parameters with a trade-off relation. Researches for the near-eye displays have focused on performance enhancement and lightening weight. Especially in optical see-through displays, display performances are heavily dependent on the optical configuration based on the imaging combiner type.

The imaging combiner can simultaneously deliver virtual images with high optical transparency for the real scene, which is a core optical component in see-through near-eye displays. Various techniques have existed for imaging combiner and optical architecture. Most of these techniques can be summarized into two different concepts: the mirror-based and the waveguide-based type.

The mirror-based methods use a semi-transparent mirror or reflective optical element as an optical combiner. This near-eye display system can be realized with comparatively simple optical architecture. Representative mirror-based methods include the birdbath design using a half-mirror as shown in Fig 1.10 and the off-axis bug-eye design using a curved half-mirror, as illustrated in Fig. 1.11.

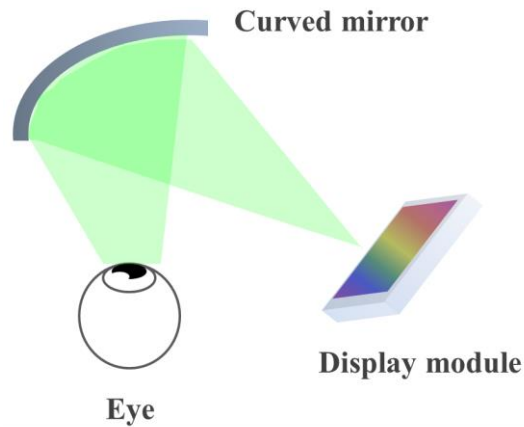


Figure 1.11 Configuration of AR near-eye display using curved mirror.

Both methods use a lens or mirror with optical power to display a magnified virtual image. Diagonally tilted or curved combiner is located in front of the eyes, which offer a wide FOV and excellent see-through quality. In addition, the fabrication process is relatively easy, and production costs are low due to the simple structure. During the early phase of AR developments, many companies introduced prototypes or products using the mirror-based technique, such as Google Glass, Meta, Mira, and Nreal [27-30]. However, these optical architectures suffer from bulky form-factor, which is not appealing to the customers. Moreover, in a curved mirror, optical distortion and resolution degradation due to the off-axis system are severe, requiring computational image compensation.

In order to reduce the optical aberration and curvature of the curved mirror, an exotic approach using freeform optics is devised [31]. Freeform optics, which consists of a freeform surface with no symmetry, can bring many advantages of minimized optical aberration, new optical function, and downsizing for the imaging system. Imaging combiner optimized using freeform optics can alleviate the aberration of the conventional off-axis system and reduce the optical system's form factor. However, freeform optics still has problems, such as complicated optical design and manufacturing, high production cost, and materials.

The waveguide-based technique conveys a display light using a thin waveguide, unlike conventional methods with the free space combiner. The waveguide-type near-eye display is one of the most promising technologies for AR devices since it innovatively reduces the form factor in front of the eye [32]. Using a waveguide, the light from the display can propagate through the thin substrate to the eye so that cumbersome optical elements can be substituted with thin optics. Also, a display module can be relocated from the front of the face to the side face. An unobstructed view of the real scene can be achieved by the optical configuration using the waveguide.

The waveguide in the AR application field has a slightly different concept from that commonly referred to in optical science. In optics, the waveguide is a micro-scale structure, which guides electromagnetic waves. In this case, the only electromagnetic wave of guide mode that satisfies a transverse resonance condition can be propagated within the waveguide [33]. Otherwise, since the waveguide in AR displays is very thick compared to a traditional waveguide, the resonance or plasmonic effects are inconsiderable. The propagating beam can be approximated with ray bundles without considering the guided mode. The waveguide in AR applications can actually be treated as a lightguide. In the display industry, two terms, waveguide and lightguide, are often used interchangeably. In this dissertation, lightguide and waveguide are not separately classified, and both are referred to as waveguide.

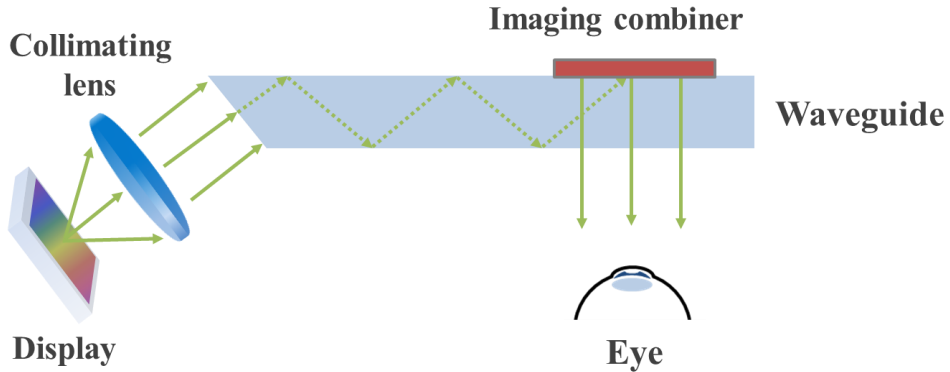


Figure 1.12 Configuration of waveguide-based near-eye display.

As shown in Fig. 1.12, the waveguide method uses a total internal reflection (TIR) principle to guide the display light through a waveguide to the front of the user's eye. The display light theoretically loses no power while traveling along the waveguide due to TIR. The waveguide technique generally uses a collimating lens to produce a parallel beam entering the waveguide at a specific incidence angle. This approach replaces diverging lights emitted by display pixels at different positions spatially with collimated lights having different direction vectors. It means that spatial information is converted into angular information. The waveguide substrate is mainly a planar structure to maintain a guiding angle, and it can achieve a form factor such as glasses with a thickness of few millimeters. Imaging combiner should be very thin because it is either inserted into the waveguide or on the surface. Depending on the type of imaging combiner, waveguide techniques can be classified into two groups: reflection-based method and diffraction-based method.

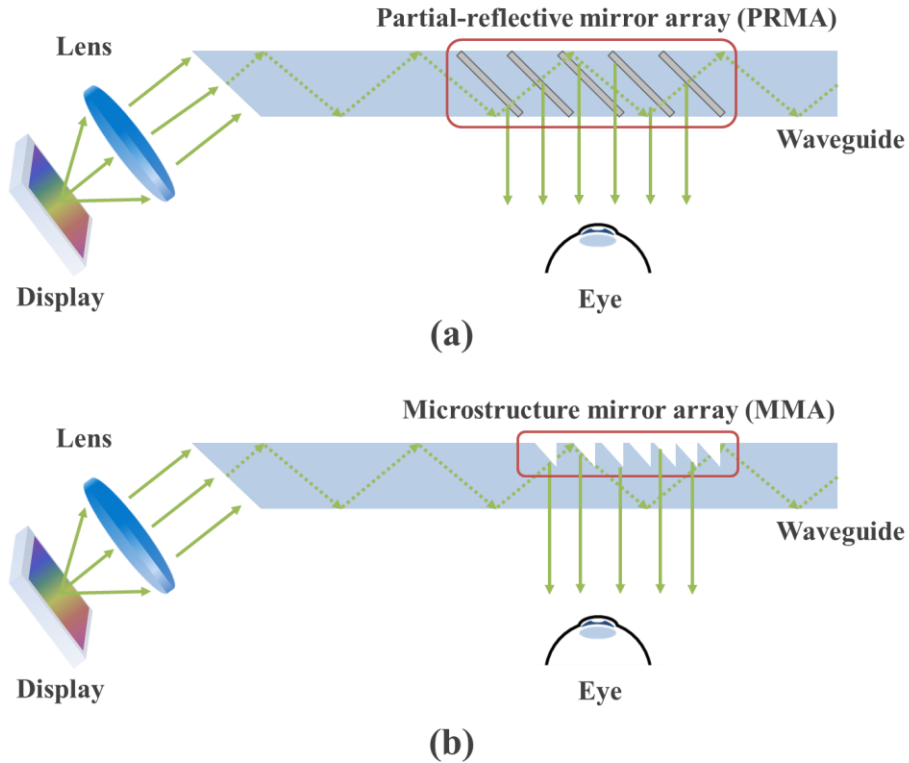


Figure 1.13 Schematic diagram of the reflection-type waveguide: (a) partial-reflective mirror array method (b) microstructure mirror array method.

The reflection-based waveguide display uses a partial-reflective mirror array (PRMA) inserted into the waveguide [34], or a microstructure mirror array (MMA) engraved on a surface [35], as shown in Fig. 1.13. Display light guided through the waveguide is extracted to the eye by the mirror reflection. These waveguide systems based on the mirror array are referred to as the geometrical waveguide, and prototypes using mirror arrays have been released by several companies such as Lumus and Optinvent [36,37]. The reflective techniques can provide relatively high-quality images by simple specular reflection. In addition, unlike the simple half-mirror method, multiple reflections by the mirror array enable a large eyebox. The optical design that can enlarge the eyebox by gradually deflecting the guiding beam with proper efficiency is called the exit-pupil expansion (EPE) technique.

However, the reflection-type waveguide system suffers from several major drawbacks that do not allow a practicable solution for high productivity and mass production. For the PRMA-based method, the FOV is determined by the waveguide thickness (T) as follow [38]:

$$\text{FOV}(rad) \approx \frac{NT \tan \alpha_s - E_b}{E_r}, \quad (1.9)$$

where N is the number of the cascaded mirror, α_s is the slanted angle of the mirror, E_b is the size of an exit-pupil, and E_r is the eye relief. The waveguide thickness needs to be thick for a large FOV through the equation above. Assuming that the number of mirrors is seven, the waveguide thickness is about 8 mm for 30° FOV. This is still thicker compared to standard glasses (3~5 mm). Furthermore, the mechanical adhesion between the waveguide and the slanted mirror arrays should require a complicated fabrication process with high precision [32].

For the MMA-based method, due to the tiny microstructure, the mid-level FOV can be achieved while allowing the waveguide to thin compared to the PRMA method. However, the MMA method also has disadvantages such as non-uniform intensity problem that the reflection efficiency varies depending on the incidence angle. The scattering and diffraction caused by the fine structure may deteriorate the image quality for the AR scene. Researchers in industry and academia try to resolve various problems for reflective methods, but it is difficult to commercialize because of their inherent limitations.

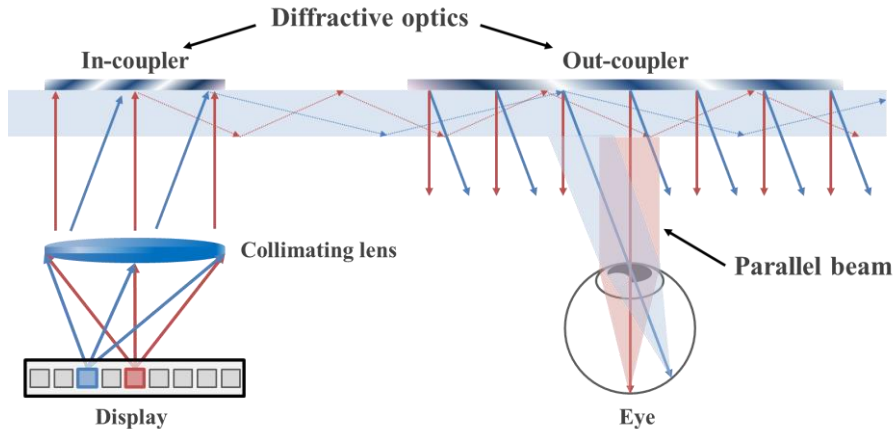


Figure 1.14 Schematic diagram of the diffraction-type waveguide.

The diffraction-based waveguide display utilizes the diffraction gratings as the imaging combiner. The diffraction grating on the input section (in-coupler) deflects the collimated input beam at a specific TIR angle, which couples into the waveguide. A guided beam by TIR is extracted to the eye by another diffraction grating on the output section (out-coupler), as shown in Fig. 1.14. The diffraction grating has a precise micro-pattern structure, which deflects the incident beam in the intended direction. The diffraction grating, which is fabricated on a flat substrate or film, can couple the display beam to the waveguide in a thin planar structure. Because of this operating scheme, the waveguide thickness can be decreased as thin as 1 mm or less, thereby reducing the form factor innovatively. Their excellent performance for form factor has appealed to consumers, and several AR development companies have launched commercial products or prototypes with waveguide-based systems.

The diffraction grating is typically divided into two types: surface-relief gratings (SRGs) and volume holographic gratings (VHGs). The Microsoft HoloLens and Magic Leap One, which are representative commercialized waveguide-based HMDs, adopted the SRG-type for their imaging combiners. SRGs are manufactured by etching the diffractive gratings on the substrate surface

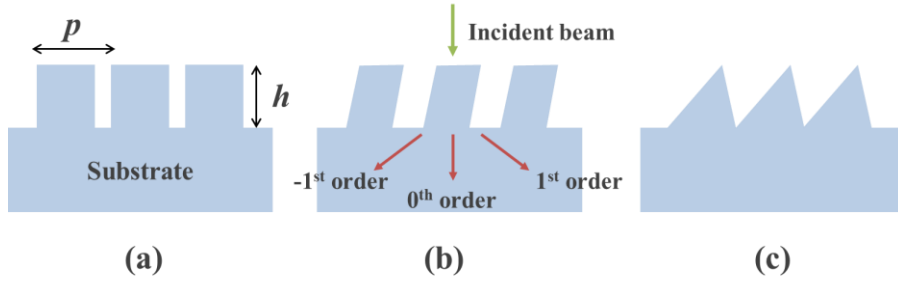


Figure 1.15 Schematic diagrams for several surface-relief gratings (SRGs): (a) binary grating, (b) binary slanted grating, and (c) triangular gratings.

using various etching techniques, such as ion beam etching, e-beam lithography, and chemical etching. There are various design parameters for SRGs design, such as the shape, height (h), repetition period (p), and refractive index, as shown in Fig. 1.15. The optical performances of SRGs, including the diffraction angle and efficiency, depend on those variables. These design parameters are optimized by suppressing specific diffraction orders to achieve maximum display performance [39]. The diffraction angle (θ_m) can be acquired by the following equation:

$$\theta_m = \sin^{-1} \left(\sin \theta_i - \frac{m\lambda}{p} \right), \quad (1.10)$$

where θ_i is the incidence angle, m is the diffraction order, and λ is the wavelength of the input beam. The display system must have respective gratings for each wavelength because of their wavelength dependency. In the SRGs type, three waveguide substrates engraved with different gratings should be required to display the three primary colors; red, green, and blue (RGB). They are referred to as a waveguide color channel.

Although SRGs-based near-eye display has a good performance for display quality with a compact form factor, there are several barriers to pursuing extreme image quality and competitive price. The SRGs deteriorate the image quality of the

real scene by unwanted high-order diffraction. A periodic grating structure diffracts the undesirable light from the real scene, inducing duplicated ghost images. In addition, the high cost of the fabrication process and difficulty in implementing an optimal grating structure may limit the production yield [32]. This overall manufacturing issue increases the product price, which opposes an obstacle to AR device's popularization.

To resolve issues for SRGs, volume gratings have been extensively investigated as the next-generation image combiner. The volume grating consists of a periodic phase or absorption perturbation throughout the entire volume. The volume grating is based on the Bragg effect, which is also called volume Bragg grating (VBG). The volume grating can be typically fabricated by a holographic technique using a photosensitive medium, and this is called volume holographic grating (VHG) or holographic optical element (HOE).

The VHGs can be recorded by interfering with two different coherent beams: reference and signal beam. When the two beams interfere inside the medium, the refractive index of the medium is modulated by the intensity of the interference pattern, thus constructing the Bragg grating structure. When the input beam is introduced to the recorded volume grating in the reconstruction process, multiple reflections occur by the layered index modulation. Those multiple reflected beams interfere with each other. Only the incident beam satisfying the Bragg matching condition (i.e., the input beam has the same wavelength and incident angle as the reference beam in the recording process) can be extracted the same as the signal beam. When the incident beam slightly mismatches the Bragg condition (Bragg mismatching condition), the input beam is diffracted with lower optical efficiency. Input beams that significantly mismatch the Bragg condition will pass through the medium, as shown in Fig. 1.16.

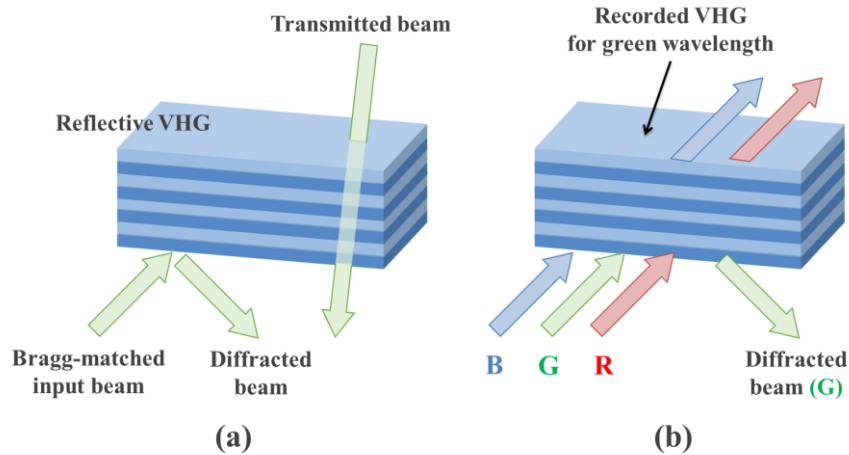


Figure 1.16 Schematic diagrams for Bragg matching: (a) angular selectivity and (b) wavelength selectivity.

Due to high angular and wavelength selectivity and low absorption, the VHGs have a high transmittance for real scenes in AR applications. It is also possible to record multiple volume grating inside the same volume that operates independently without crosstalk of each recorded pattern. The multiplexing technique of VHGs can simultaneously implement diffraction gratings for different colors or multiple optical functions in a single recording medium. The excellent see-through and multiplexing property is advantageous to be utilized as an imaging combiner for AR displays.

The VHGs are manufactured by optical recording, enabling mass production with high productivity and can rapidly modify the design specifications. Furthermore, the VHGs can be recorded in an ultra-thin film (typically less than 100 μm), reducing the thickness and weight of the waveguide system compared to the SRG-based system using a glass substrate. Despite these significant advantages, the recording material property with low mechanical and thermal resistance needs improvement. In this dissertation, the VHG was adopted as an imaging combiner considering the high degree of freedom in optical design, fabrication cost, and growth potential in research and industry.

The waveguide-based near-eye displays have many advantages listed above, but they have several limitations. First, FOV is relatively narrow compared to other imaging methods. In general, the FOV of the commercialized device is about 30 to 40 degrees. The FOV is limited by the angular bandwidth of the diffraction optic in a single waveguide structure. The system using VHGs has a narrower FOV than using SRGs due to their high angular selectivity. In order to resolve this problem, various multiplexing methods have been proposed, but it is still insufficient to provide an immersive experience. Second, there are insufficient design degrees of freedom. Due to the optical structure in which the incident beam must be parallel light to satisfy the guiding condition by TIR, there are practical constraints on system change. In the out-coupler part, a compensating device should be added to use conventional transmissive-type optics for distortion-free real scenes. Because of this complexity of system architecture, it is not easy to support additional optical functions. In this dissertation, novel methodologies in the waveguide-based near-eye display have been proposed to enhance optical performance while maintaining a compact form factor.

1.4 Motivation and purpose of this dissertation

In the previous section, various design parameters and representative imaging combiners in AR near-eye display are introduced. The imaging scheme for the virtual image is primarily determined by the optical function of the imaging combiner, and these imaging methods inevitably have limited system performance. It is complicated and crucial to balance the trade-off relations among the various system performances.

VR/AR applications still get a small percentage of the related market. Various factors such as unsatisfactory image quality, an unreasonable price and lack of killer content, and difficulty in integrated platforms hinder the popularization of VR/AR. Above all; the form factor of the system is the biggest obstacle to cultivate a broader market. To provide comfort and extended wearing conditions, the form factor should be compact to a glasses-level. Table 1.1 summarizes the display performance and technical challenge in AR displays. There are several pros and cons, depending on the imaging combiner and display type. Various researches have been conducted to overcome the drawback of each system. However, the form factor is inherently restricted by the optical configuration, and considerable improvement is challenging. In that respect, the waveguide technology seems to be the most promising for wearable display devices since they can implement a compact and lightweight optical system in front of the eye with a form factor comparable to glasses. However, even though the waveguide technology has a consumer-friendly form factor, inadequate several display performances need to be improved compared to other technologies. This dissertation focuses on improving display performance in waveguide-based near-eye displays.

In general, the waveguide technique has a single focal plane at infinity due to the collimated TIR beam. Traditional focus-tunable optical elements can be employed as an additional eyepiece to support multiple focal planes, which

Table 1.1 Summary of AR near-eye display depending on the imaging combiner and display type.

Type	Combiner	Form factor	Image quality	FOV	Eyebox	Focus cue	Issues
Mirror-type	Beam splitter (half-mirror)	Medium	Excellent	Small	Moderate	Affordable	Small FOV
	Curved mirror	Large	Poor	Large	Good	Affordable	Bulky
	Freeform	Medium	Good	Moderate	Moderate	Affordable	Complicated fabrication
Waveguide-type	Reflective optics	Good	Moderate	Moderate	Good	Poor	Complicated fabrication
	SRG	Excellent	Moderate	Moderate	Excellent	Poor	Complicated fabrication
	VHG	Excellent	Good	Small	Excellent	Poor	Small FOV
Retinal projection	Holographic lens	Excellent	Moderate	Large	Poor	All-in-focus	Narrow eyebox
Holographic	Holographic lens	Medium	Poor	Small	Poor	Natural	Filtering Speckle

undermines the advantage of the form factor. In addition, if the eye relief is increased by additional optics, other display performance such as FOV and eyebox may be degraded.

As shown in Table 1.1, the waveguide technique has low or mid-level FOV, which hinders fully immersive experiences. In the waveguide, FOV is determined by the maximum angular bandwidth and diffraction efficiency of the diffractive optical element, unlike the mirror-based method, which has a trade-off relationship with the thickness of the imaging combiner. In particular, the maximum angular bandwidth is related to the refractive index of the diffractive optics, and the FOV increases as the refractive index increases. To enlarge the FOV, a substrate or recording medium with a high refractive index has been developed. However, it is very challenging to modify the physical and chemical properties of the medium significantly.

To enhance display performances of FOV and focus cue without increasing the form factor, polarization-dependent optical devices are introduced in the proposed AR waveguide-based near-eye display. The polarization-dependent optics is based on the geometric phase (i.e., Pancharatnam-Berry phase), which is manifested by the extra phase delay in the anisotropic medium [40]. Because polarization-dependent optics is thin films (less than 1 mm) that have very lightweight (less than 1 g), the form factor of the entire system hardly increases even when they are appended to an existing system. The polarization-dependent optics has different optical functions according to the polarization state of the input beam. Novel eyepieces with enhanced performance are devised by taking advantage of their small form factor and multi-functionality. Since the proposed eyepieces can transmit light of real scenes by modulating the polarization state, they are utilized as see-through AR combiner. This dissertation proposes optical design methodologies for enhanced waveguide-based near-eye displays using the ingenious eyepiece-combiner based on polarization multiplexing. The modified

optical structures for a waveguide-based system to enlarge the FOV and support the focus cue are presented. In addition, a waveguide-based retinal-projection display with an extended eyebox is proposed using the polarization multiplexing technique. The proposed system is possible to alleviate the inherent limitation of the retinal-projection display, in which a virtual image can be observed only in a fixed viewpoint. Finally, the weaknesses of the proposed optical architectures and eyepieces are analyzed, and solutions or alternatives for them are discussed.

1.5 Scope and organization

The main body of this dissertation is composed of three chapters. In Chapter 2, a waveguide-based near-eye display for multi-focal planes is proposed. To support multi-focal planes, a novel eyepiece-combiner based on a polarization-dependent eyepiece lens is devised. Dual focal planes can be generated by changing the focal length of the proposed eyepiece depending on the polarization state of the input beam. The detailed structure and operating principle of the see-through combiner are presented, and the prototype system is demonstrated in this chapter. Also, system performance is analyzed to ensure the prototype operates in practice.

In Chapter 3, an enhanced waveguide-based near-eye display with enlarged FOV is proposed. In order to increase the FOV, polarization-dependent gratings are adopted into the out-coupler part. A novel structure can provide an extended FOV of up to twice the limited performance in a single waveguide. According to the proposed optical device and structure, the distortion of real scenes and virtual images is analyzed through simulation and verification experiments. By applying the proposed scheme to the angular-multiplexed VHG, the FOV is improved to the level of the commercialized device based on SRGs.

In Chapter 4, the author proposes a retinal-projection display for an extended eyebox with a polarization-switching scheme. The author presents the merits of the waveguide-based method compared to the free-space propagation method. The retinal-projection display system is constructed based on the waveguide. To resolve the eyebox limitation for the traditional retinal-projection display, a novel optical structure is proposed by using polarization-dependent optical devices. It can modulate a viewing position with switchable focal spots. By changing the position of the focal spot, it is possible to extend the eyebox and alleviate a duplicated or blank image problem by the spacing between each focal spot. The proposed system can be manufactured to enable large DOF, which can mitigate the VAC issue.

As described above, this dissertation focuses on enhancing the display

performance of the waveguide-based AR near-eye display by using polarization-dependent devices and a multiplexing technique. The proposed optical devices and architecture can effectively resolve critical issues for the waveguide technique without compromising the compact form factor, and these solutions can further advance technology for waveguide-based display.

Chapter 2 Dual-focal waveguide-based near-eye display using polarization-dependent combiner lens

2.1 Introduction

As described in Chapter 1, the optical configuration of a see-through near-eye display can be summarized into two main concepts: ‘Mirror-type’ and ‘Waveguide-type.’ The mirror-based near-eye display uses a semi-transparent mirror as an optical combiner. They can be implemented with comparatively few optical elements and straightforward configuration. The mirror-type using flat half-mirror or curved half-mirror as an imaging combiner is easily implemented to insert additional optics to the optical path before entering the combiner. This optical structure may support focus cues with minor modifications to the optical system using a focus-tunable optical device. However, despite these advantages, the mirror-based systems suffer from a bulky form-factor, which is uncomfortable to wear for long hours.

Meanwhile, the second concept using a waveguide technique has a lightweight and compact form factor. Using a thin waveguide and diffractive optics can eliminate cumbersome optical components in front of the eye that obstructs the user’s view. Although the waveguide technique provides a compact form factor that enables wearing without any discomfort in daily life like glasses, it is challenging to modify it due to the standardized optical structure.

As previously mentioned in Chapter 1.3, in the waveguide-based near-eye display, collimated light is extracted to the user’s pupil by an out-coupler in front of the eye. In this case, virtual images are displayed at infinity, and the observer’s eye is forced to focus at infinity by accommodation response, as shown in Fig. 2.1. If a real object is located near a user, augmented images appear blurred due to the

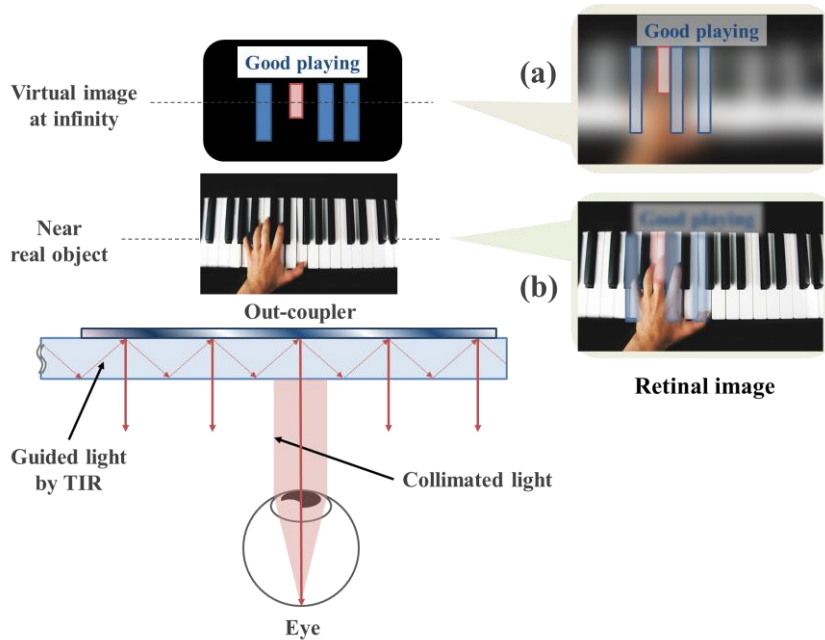


Figure 2.1 Focus cue in the conventional waveguide system: (a) Far-corrected retinal image for infinity focus, (b) near-corrected retinal image for near objects.

difference in accommodation depth between real objects and display images. If users stare at a real object, the virtual image looks blurred, and if staring at the virtual image, the real object looks blurred. This blur effect may compromise the visibility of the augmented image. This problem may also hinder the user from vividly experiencing mixed reality and induce visual fatigue by the mismatch between accommodation and vergence distance, which is referred to as the VAC issue [20].

To mitigate the problem, various solutions have been proposed in the 3-D display system and are summarized in [41]. Given that most of them have additional bulky optics to adjust the focal plane, they are difficult to employ in a waveguide display directly. Because of the operational principle using the collimated light, traditional focus-tunable optics for focus adjustment cannot be located in the input part before entering the waveguide. To locate them in the output part, conjugation optics that compensates for real-scene distortion should be

required, which makes the system heavy and bulky and undermines the merit of the waveguide-based system.

Except for methods suitable for the mirror-based methods, other approaches have been proposed in the waveguide-based near-eye display. For Microsoft HoloLens (Kress and Sterner) proposed placing a set of additional lenses on each side of the out-coupler [42]. This approach can support a more comfortable AR environment by visualizing virtual images at an appropriate depth but can provide only a single focal plane. Yeom et al. proposed a waveguide-type holographic near-eye display, which can deliver a holographic image offering a natural accommodation response [43]. However, the AR near-eye display, based on the holographic principle, suffers from a significant problem since exit pupil and eyepiece have a trade-off relationship [16]. Kim and Park proposed a retinal-projection-type near-eye display using a waveguide, which provides always-focused images [44]. This method differs from the conventional waveguide technique because the output beam is not a collimated light but a converging light. Magic Leap has recently released an SRGs-based commercial product, which renders at two distinct focal planes [45]. They adopted two-waveguide channels with respectively different focal planes for a single color. For a full-color system, six waveguide channels are required, which increases the total thickness of the optical system. Although this approach is very straightforward, it has the limitation that the system thickness increases in proportion to the number of focal planes.

In this chapter, the author proposes a dual-focal see-through waveguide-based near-eye display using a novel combiner-eyepiece. A novel optical device called a polarization-dependent combiner lens (PDCL) can support two different focal planes (near and infinity) depending on the polarization state of the input beam. The PDCL is ultra-thin compared to traditional optics. The proposed system with a compact form factor can achieve near-corrected focus cues for virtual images.

2.2 Optical design for polarization-dependent combiner lens

2.2.1 Design and principle of polarization-dependent combiner lens

As discussed in the previous section, the waveguide techniques using diffractive optics provide a virtual image on infinite focus. In order to adjust the focal plane to a specific depth position, a concave lens is required to form a virtual focal point. When using a conventional lens, an additional lens for compensating a real-scene distortion should be adopted on the opposite side of the out-coupler, which causes an increase in form factor. In addition, in this case, it cannot provide a wide comfort zone because only a single focal plane is supported.

In order to expand the zone of comfort while maintaining the form factor, a transmissive-type combiner lens with a thin film type is devised. The proposed eyepiece-combiner is based on a geometric phase holographic lens (GPHL) [40]. The GPHL is a type of geometric phase lens fabricated by optical recording using holographic technology and an anisotropic medium. The GPHL has high optical efficiency and superior homogeneity of attenuation and dynamic phase. In addition, the fabrication process of the GPHL is very similar to that of the conventional hologram. Because of these advantages, the GPHL is a commercialized geometric phase lens, enabling mass production with excellent imaging performance. In this section, the author will briefly introduce the principle of geometric phase lens, and more details can be found in [46]. The geometric phase, which is also called Pancharatnam–Berry phase, is a phase difference acquired over the cyclic process in adiabatic processes. This effect explains various physical phenomena in the Hamiltonian system. In particular, the geometric phase effect can explain the extraordinary phase delay for polarized light, which is the main principle of the geometric phase lens. The polarized light changes its polarization state through a waveplate due to the phase delay by optical path difference (OPD). In an isotropic medium, ordinary phase delay (δ_o) (i.e., dynamic phase) is calculated as:

$$\sigma_o = \frac{2\pi}{\lambda} nd, \quad (2.1)$$

where n is the refractive index of the medium, d is the thickness, and λ is the wavelength of the incidence light. Meanwhile, in an anisotropic medium, extra-phase shift (φ) is produced via the geometric phase effect, which is referred to as geometric phase and can be presented as:

$$\sigma_e = \frac{2\pi}{\lambda} \left(\frac{n_e + n_o}{2} \right) d + \varphi(x, y, \Phi), \quad (2.2)$$

where n_e is the extraordinary refractive index, n_o is the ordinary refractive index, x and y are the spatial coordinates on the substrate plane, and Φ is the orientation angle of the anisotropic medium.

The polarized light and polarization change by phase shift can be expressed on the Poincaré sphere, a graphical tool for visualizing of the polarization state. The geometric phase is acquired in a closed path to be traversed on the Poincaré sphere. Assume that the original light is horizontally linear polarized (indicated at point A), and it is converted to right-handed circular polarization (RCP) using quarter-waveplate (QWP) (point B). The RCP light is then turned into left-handed circular polarization (LCP) with a half-waveplate (HWP) (point C). Finally, the LCP light is turned back into the original polarization state (point A) using a QWP. This sequence of polarization change is a cyclic process within a closed pathway, as illustrated in Fig. 2.2.

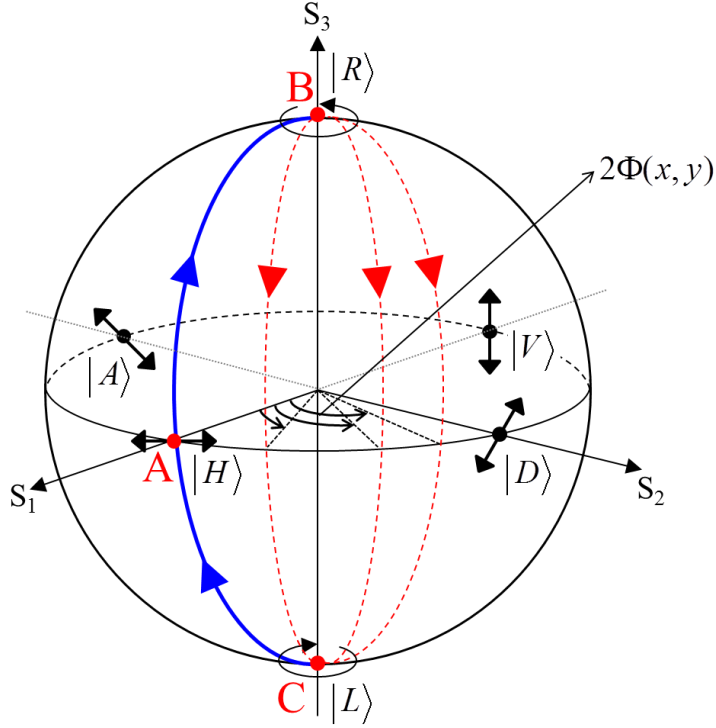


Figure 2.2 Geometric phase effect by closed path on the Poincaré sphere. The solid line (A→B, C→A) represents the polarization change by the QWP. The dot lines (B→C) represent different paths by the HWP with varying orientation, respectively.

As shown in Fig. 2.2, there are various paths when the RCP converts to LCP with an HWP. The optical path is varied by the orientation of the HWP. In this cyclic process, the polarization state of the output beam is the same, but phase shift changes according to the path. The variation of the phase shift caused by the path difference in the closed-loop is the geometric phase, which is given by half of the orientation angle of the HWP, as follows:

$$\varphi(x, y, \Phi) = \pm 2\Phi(x, y). \quad (2.3)$$

Note that the azimuthal angle on the Poincaré sphere is double the orientation angle, which is the geometric phase by optical anisotropy. When an incident light with

arbitrary polarization $|\Psi_{in}\rangle$ passes through an optical element with a geometric phase, the output light can be divided into three parts as the following equation using Dirac notation [40]:

$$e^{j\delta_{in}} |\Psi_{in}\rangle \rightarrow \sqrt{\eta_+} e^{j(\delta_{in}+2\Phi)} |\Psi_+\rangle + \sqrt{\eta_-} e^{j(\delta_{in}-2\Phi)} |\Psi_-\rangle + \sqrt{\eta_0} e^{j\delta_{in}} |\Psi_{in}\rangle, \quad (2.4)$$

where δ_{in} is the initial phase, η is the optical efficiency, Φ is the inclined angle of the optical axis, and $|\Psi_{\pm}\rangle$ is the two eigenstates as the primary term (+) and conjugate term (-). Two eigenstates are always mutually orthogonal to each other and are generally described as circular polarization of RCP and LCP. The last term in the above equation represents the unmodulated light by optical elements, typically called the DC term. If the orientation angle Φ varies spatially, the geometric phase also has a spatial dependency, as shown in Fig. 2.3.

Optical element with geometric phase

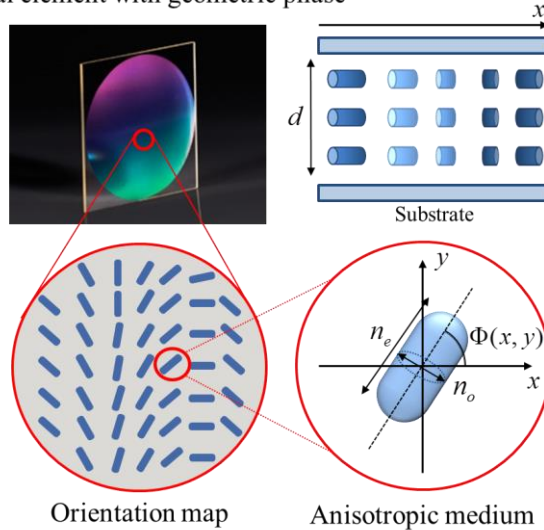


Figure 2.3 Geometric phase optical element with spatially varying optical axis.

The geometric phase lens is designed so that the spatial distribution of the geometric phase has the phase profile for the lens. Commercialized GPHL converts an incident beam with circular polarization into a conjugated output beam with high coupling efficiency ($\sim 98\%$) excluding a tiny leakage ($\sim 2\%$) as follows:

$$e^{j\delta_m} |\Psi_{\pm}\rangle \xrightarrow{GPHL} \sqrt{\eta_{\pm}} e^{j(\delta_m \pm 2\Phi(x,y))} |\Psi_{\mp}\rangle + \sqrt{\eta_0} e^{j\delta_m} |\Psi_{\pm}\rangle. \quad (2.4)$$

The GPHL used in the proposed configuration is fabricated by using polymerized liquid crystal and linear photo-alignment polymer [40], which is very thin (0.45 mm) and lightweight. When the incident beam is LCP, the GPHL operates as a concave lens that has a negative focal length, as shown in Fig. 2.4(a). While with an RCP beam, the input beam is converged at the focal point, as shown in Fig. 2.4(b). In both cases, the absolute value of the focal length and optical efficiency is theoretically the same. A polarization-dependent eyepiece-combiner is devised by using their conjugate function according to the polarization state of the input beam.

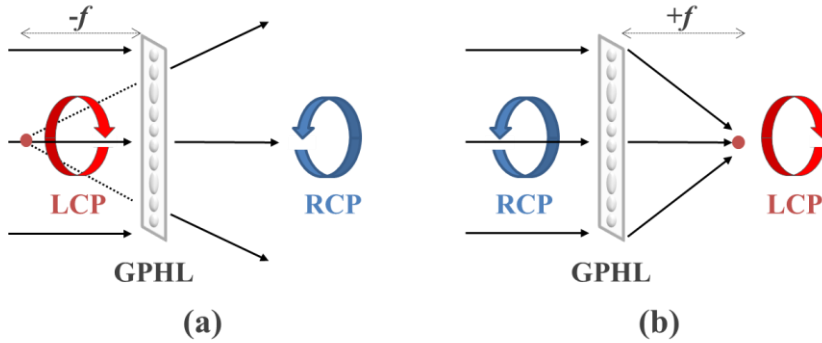


Figure 2.4 Illustration of GPHL operations: (a) with a convex lens function and (b) with a concave lens function. The DC terms are neglected.

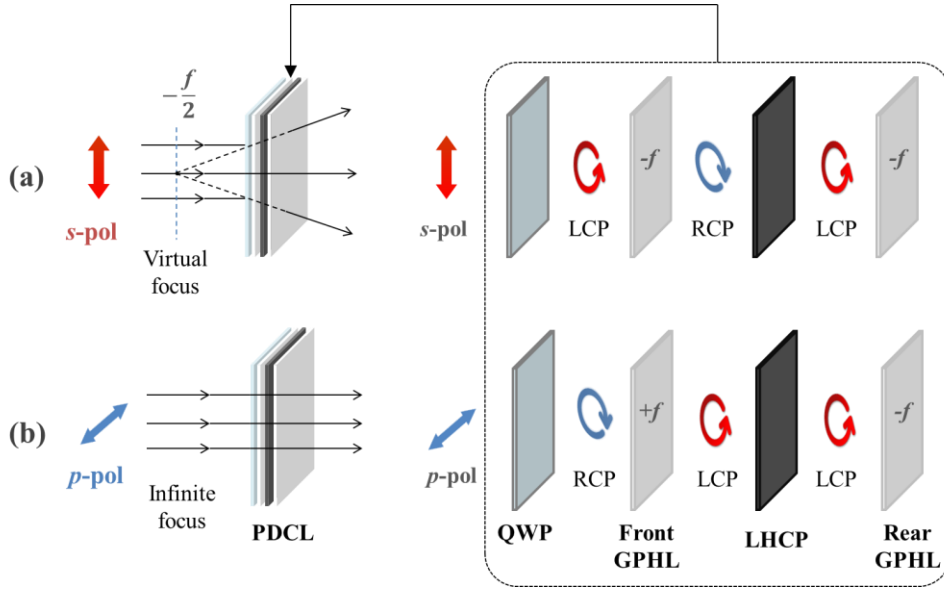


Figure 2.5 Illustration of the proposed PDCL structure and polarization states (a) for lens mode and (b) for optical window mode.

Figure 2.5 shows the schematic diagram of the PDCL, which can operate in lens mode or optical window mode. The PDCL consists of two GPHLs with the same focal length, a QWP, and a left-handed circular polarizer (LHCP). For the dual-focal plane, two GPHLs are stacked across the circular polarizer. The QWP attached to the front GPHL is used to convert the input beam with linear polarization into circular polarization. The LHCP allows the rear GPHL to act as a concave lens irrespective of a polarization state of an input beam.

For lens mode, a vertical polarized (i.e., s-pol) beam is incident on the PDCL; two GPHLs can act as a diverging lens in succession. In this case, the focal power of PDCL is merely equivalent to half of the GPHL because the distance between the two GPHLs can be ignored due to the thin circular polarizer film (~ 0.3 mm) compared to the focal length of the GPHL. This operating scheme can float a virtual image at the focal length of the PDCL.

For optical window mode, a horizontal polarized (i.e., p-pol) beam is incident on the PDCL; the lens function of two GPHLs cancel each other out. The input

beam can go through the PDCL without any further refraction. The multi-functionality depending on the polarization state can be a suitable eyepiece lens for the AR display system. The proposed optical component can be placed directly in front of the eye. It is also easily attached to the waveguide without burdensome increases in form factor due to its flatness and thinness.

2.2.2 Prototype implementation

The PDCL is fabricated with commercialized GPHL (Edmund Optics S/N: 34-466) with a focal length of ± 100 mm. Each optical film constituting the PDCL is combined using an optical adhesive (Norland 65). The optical adhesive enables clear attachment through ultraviolet (UV) curing and eliminates the air gap between the optical elements with index matching, increasing optical efficiency. Figure 2.6 shows the lab-fabricated PDCL with 1 mm thickness and 25 mm diameter. The fabricated PDCL has a negative focal length (f_p) of -50 mm for lens mode, which is a maximum focal distance of virtual images with commercial products. The detail of the fabricated PDCL is presented in Table 2.1.

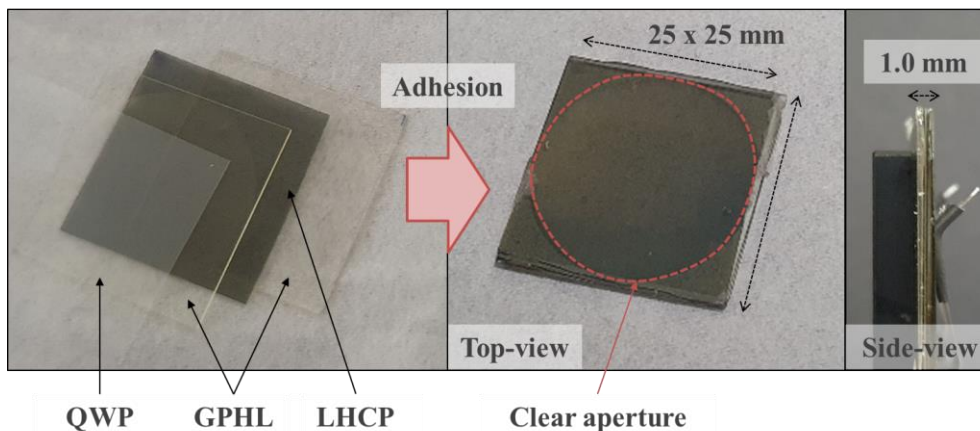


Figure 2.6 Photographs of the proposed eyepiece-combiner.

Table 2.1 Specification of implemented PDCL.

Index		Value	
Thickness		1.0 mm	
Diameter (D_P)		25 mm	
Focal length (f_P)		- 50 mm	
Optical efficiency	Total transmission (η_P)		46.0%
	Mode	Primary (η_+)	91.6%
		Conjugation (η_-)	4.1%
		DC (η_0)	4.3%

Optical efficiency is measured with an optical power meter (Newport 1830-C model) at 532 nm wavelength. Total transmitted efficiency (η_P) is calculated by dividing the optical intensity of light passing through the PDCL by the incident beam's original intensity. The optical intensity for each operating mode is acquired by placing a circular polarizer at the position passing through the PDCL. The conversion efficiency of the ideal PDCL is 96%, but the experimentally measured efficiency shrinks by 4.4%. This degradation may occur because the polarization state converted by a circular polarizer inside the PDCL is not perfectly circular polarization but elliptical polarization.

In Fig. 2.7, the multi-functionality of the proposed device is demonstrated. To verify the feasibility, we captured changes in the size of the output beam while changing the distance of the diffusing screen. The beam radius does not change with a vertical-polarized collimated beam. On the other hand, as the distance of the screen from the PDCL increases, the horizontal-polarized input beam diverges. By calculating the ratio of the diverging beam size depending on the screen distance, it is demonstrated that the PDCL has a virtual focus of -50 mm. These results well accord with the operating scheme in Fig. 2.5.

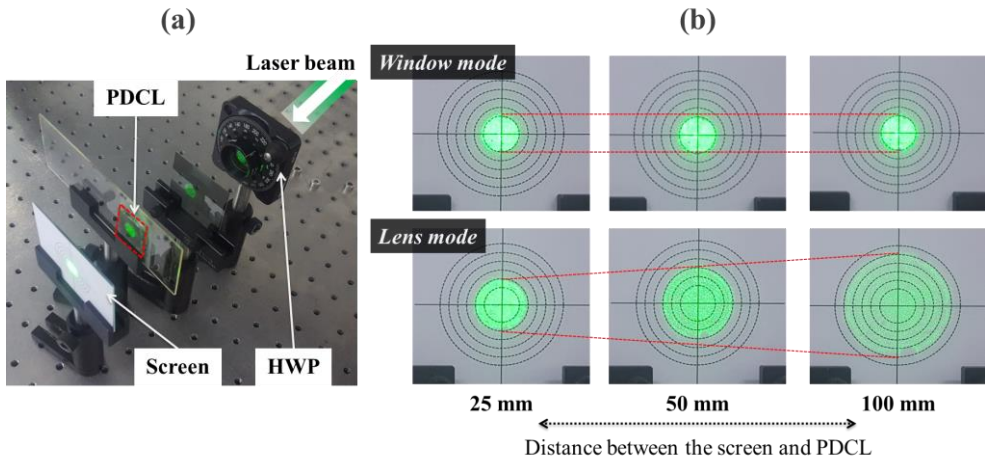


Figure 2.7 Examination of dual-focal functionality using the PDCL: (a) experimental setup, (b) captured image in optical window mode, and (c) captured image in lens mode.

2.3 Waveguide-based augmented reality near-eye display with dual-focal plane using polarization-dependent combiner lens

2.3.1 Implementation of the prototype and experimental results

The proposed transmissive-type eyepiece lens can perform the dual function of the lens and see-through window with polarization multiplexing. Due to its multi-function, it is possible to display virtual images at infinity and specific distances in a waveguide-based near-eye display. The two-dimensional architecture of the proposed system with a PDCL is presented in Fig. 2.8. The entire optical system consists of a laser scanning projector (LSP), a polarization rotator unit, a planar waveguide, a PDCL, reflection-type VHGs as imaging combiner, and a linear polarizer.

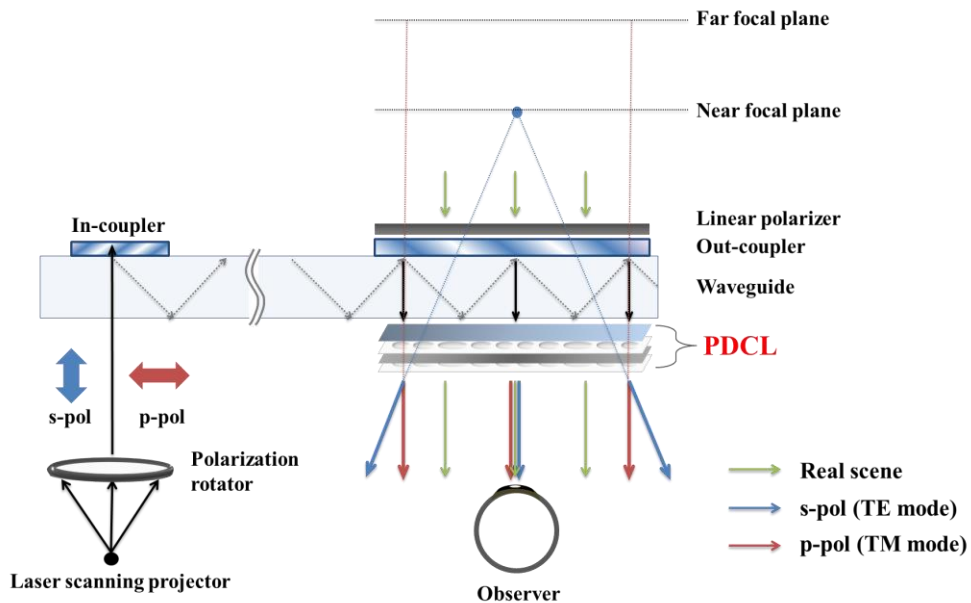


Figure 2.8 Schematic diagram of proposed waveguide-type AR near-eye display. A green line indicates the light for the real scene. Each blue and red line indicates the optical path for virtual images depending on the polarization state, respectively.

Instead of the micro-display panel and collimating optics in conventional waveguide techniques, the LSP is adopted to render virtual images. This projection-based display has several advantages, such as high contrast, excellent brightness, and compact module size. Currently, purchasable micro-display provides moderate brightness in dark indoor settings but has insufficient brightness in bright outdoors. On the other hand, laser projectors have an ultrahigh brightness by straight-line beam propagation and high color purity with narrow spectral-bandwidth [47]. These advantages can make up for the weaknesses of waveguide systems using diffraction gratings.

The randomly polarized light emitted from the LSP is converted to a linear polarization state by a polarization rotator unit, which can support time-sequential polarization multiplexing. The polarization rotator in the used experiment is implemented by an electrical-switching retarder (Thorlabs LCC1221) and a linear polarizer. The active waveplate operates as an HWP or see-through window by an electric signal, which can switch between s-pol and p-pol with a fast operating speed of up to 100 Hz. It can display a video with two focal stacks in real-time. The linearly polarized beam is incident on the waveguide and diffracted by the in-coupler VHG. The diffracted beam propagates along the waveguide by total internal reflection, and then the extracted beam by the out-coupler VHG enters the PDCL. By synchronizing a polarization rotator and display module, the proposed system can support two discrete focal planes located at infinity or near-distance according to the optical power of the PDCL.

The in-coupler and out-coupler VHGs are fabricated with photopolymer films. Figure 2.9 shows the recording process of the VHG. By using a prism, the signal beam can be incident on the recording medium at an incident angle, satisfying the TIR condition in the waveguide. Two imaging couplers have the same grating properties, such as Bragg angle and grating spacing, so that the out-coupler can only be recorded by rotational-symmetrically reversing the photopolymer film

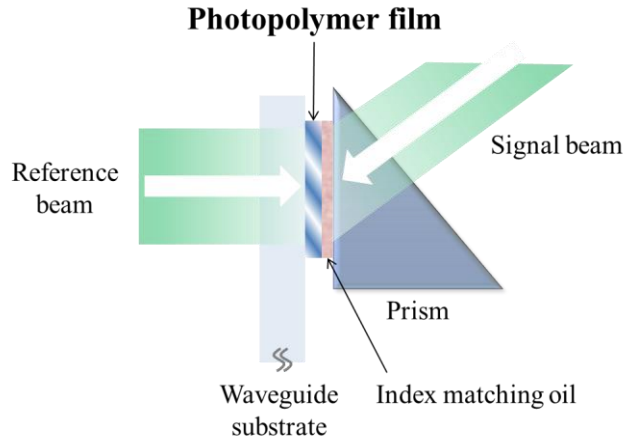


Figure 2.9 Schematic diagram of the recording setup for VHG.

in the one recording setup. Index matching oil is used between the prism and the photopolymer film to prevent unwanted back reflection due to the air gap. The detail of the fabricated VHG coupler is presented in Table 2.2.

A horizontal polarizer is located in front of the out-coupler to observe undistorted real scenes irrespective of polarization. In this case, the PDCL always acts as an optical window for real scenes, and see-through real-world scenes can be observed. The air gap between the linear polarizer and out-coupler should be required to prevent an optical loss of multiple reflections by the EPE scheme. In the experiment, the polarizer is placed apart from the out-coupler with the 0.1 mm gap.

Table 2.2 Specification of fabricated VHG.

Index	Value
Model	Bayfol photopolymer
Thickness	4 μm
Refractive index modulation	1.5 ± 0.03
Bragg incidence angle	60°

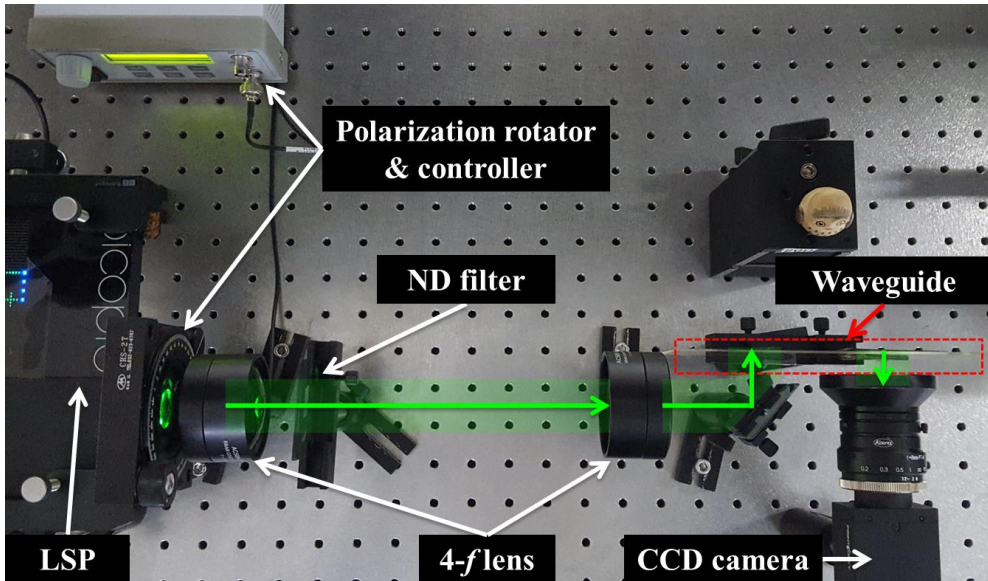


Figure 2.10 Experimental setup of proposed configuration on optical table.

The experimental setup for the proposed configuration is constructed on an optical table. The corresponding prototype is shown in Fig. 2.10. The commercialized LSP (Celluon PicoPro) is adopted as a display source in the experiment. The display resolution is 1280×720 pixels, and the maximum optical scanning angle is 43 degrees in a horizontal direction. The clear aperture of the polarization rotator is 25.4 mm, which acts as an entrance-stop that limits the overall range of projection angle. This limited specification is 35 degrees and is larger than the angular-selectivity of the recorded HOE that can guarantee FOV of 10.5 degrees in FWHM along a horizontal direction. A 4- f system is set up to focus the input beam on the in-coupler VHG. This relay system merely relocates the scanning mirror plane of the LSP to the in-coupler HOE nearby, which can provide an enlarged FOV and display resolution compared to the absence of a 4- f system. If there is no 4- f system, only the input beams with a small acceptance angle can reach the out-coupler due to wide divergence angle of the LSP and limited in-coupler size. The extended FOV by the 4- f system can be confirmed through simulation, as shown in Fig. 2.11. The focal lengths of the 4- f lenses are 75 mm

and 150 mm, which provide $\times 2$ magnified beam diameters (~ 2 mm). The optical couplers are recorded with a wavelength of 532 nm. The planar waveguide substrate is a polished glass of which thickness is 0.6 mm. The specification of the GPLH used in the experiment is presented in Table. 2.1.

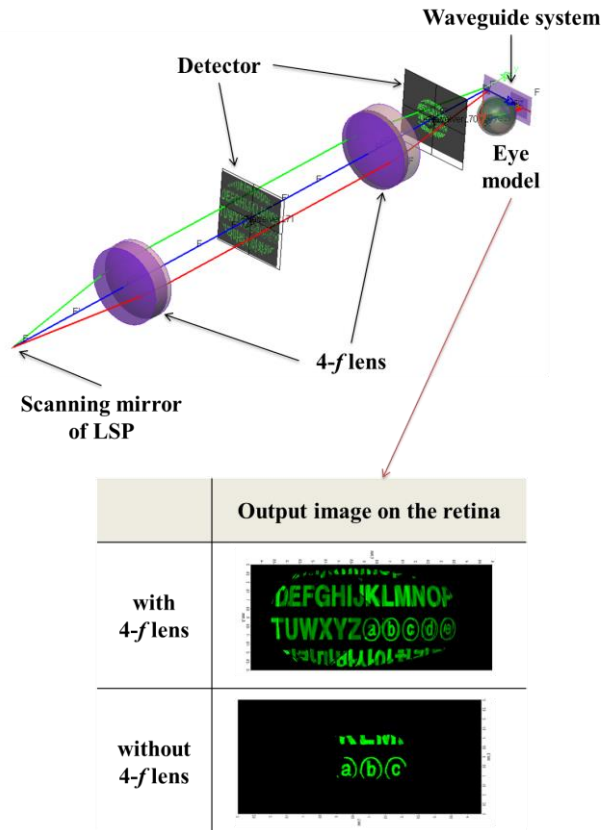


Figure 2.11 Ray-tracing simulations for the 4- f lens system.

Figure 2.12 shows the photographs of the experimental results taken with different focal planes of a CCD camera, which is located at the distance of eye relief with an exposure of 0.1 sec. A camera lens has $f/1.4$ and an 8 mm focal length. The aperture diameter of the lens is adjusted to be similar to the pupil size

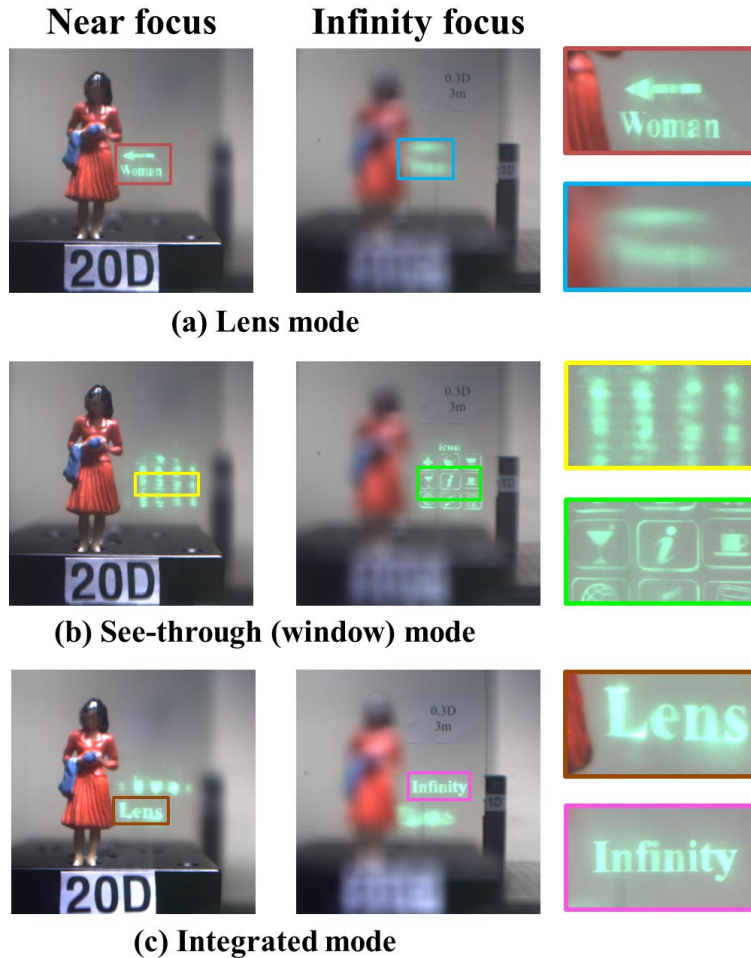


Figure 2.12 Photographs of experimental results: (a) in lens mode, (b) in window mode, and (c) in integrated mode.

of the human eye in an indoor environment. To visualize the change of focal distance, a woman-shaped figure is placed at 20 D (near), a bar-type target is placed at 1 D (middle), and a white background wall is located at 0.3 D (far). Virtual objects, such as texts and graphic symbols, are rendered at 20 D and 0 D (infinity), respectively, according to the operating mode of the PDCL. In lens mode, the virtual image is sharply focused when the camera focuses at 20 D, as shown in Fig. 2.12(a). On the other hand, when the camera focuses on the background wall, the virtual image is blurred. Figure 2.12(b) shows the see-through mode when the

virtual image is rendered at infinity. In this case, virtual images are blurred when the camera focuses on the woman toy (near object), and the blurred shape is dependent on the shape of the exit pupil replicated by the EPE scheme. When the camera focuses on the text on the paper attached to the wall (far object), the virtual image is in focus. In Fig. 2.12(c), both virtual images located near and infinity are visualized simultaneously. In integrated mode, dual-focal planes can be supported in real time by synchronizing the display module and polarization rotator. As described in the experimental results above, the proposed system can provide two independent focal planes for virtual images with a polarization-multiplexing technique and a proposed polarization-dependent eyepiece-combiner and always observe a real scene without distortion.

2.3.2 Performance analysis and discussion

In this section, major display performances of the proposed system are analyzed, and their limitation and countermeasures are discussed. In the first parameter, the eyebox of the prototype system is acquired by measuring the size of the exit pupil, as shown in Fig. 2.13. For the waveguide structure, duplicated output beams are generated due to multiple TIR and diffraction at the out-coupler, which is called an EPE scheme. In this case, the total width of the duplicated beams is determined as the eyebox, as shown in Fig. 2.13(a). The period of multiple reflections (Λ) by EPE is $2t \tan(\theta_g)$, where t is the waveguide thickness, and θ_g is the guiding angle, which is about 2.1 mm for an on-axis incident beam. Since this value is similar to the laser beam's diameter, a quasi-continuous exit-pupil is formed, as shown in Fig. 2.13(b). The measured eyebox is about 25 mm, which is similar to the size of PDCL. In this case, the user can observe the virtual image without vignetting in the eyebox.

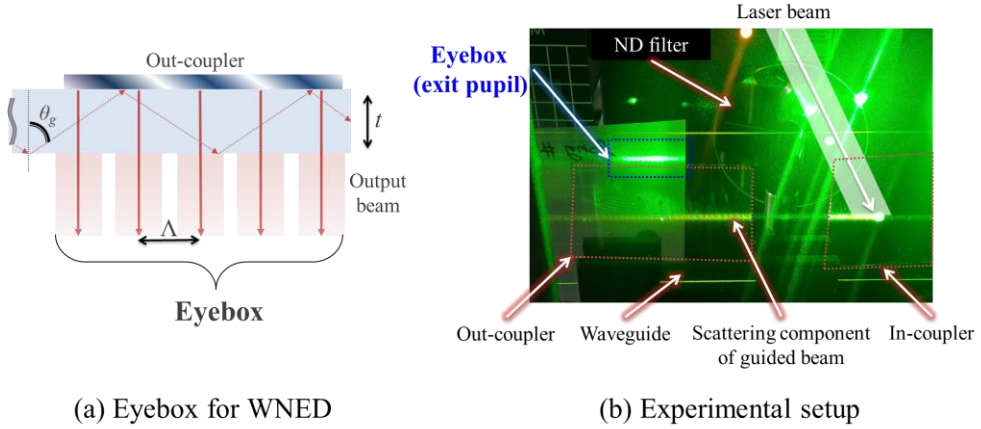


Figure 2.13 (a) Eyebox definition for the WNED system. (b) Photographs of experimental setup for measuring eyebox.

Considering the beam components corresponding to the outermost FOV, at least two output beams must enter the pupil regardless of the pupil movement for a continuous eyebox, which can be expressed by the following inequality:

$$2\Lambda_{\max} \leq D_p + W_b, \quad (2.5)$$

where D_p is the diameter of the eye pupil, and W_b is the beamwidth of the laser beam. The average standard pupil diameter is 4 mm, and W_b is 2 mm in the experiment. The maximum period (Λ_{\max}) corresponding to the outermost FOV of 10 degrees is 2.9 mm. Since the above requirement is satisfied, the prototype system can provide a continuous eyebox.

In the second parameter, the effective FOV of the proposed system is determined by the operating mode. Figure 2.14 demonstrates the limiting factors of the FOV in the proposed configuration. First, the maximum FOV (θ_1) limited by the PDCL aperture (D_P) can be simply written as:

$$\theta_1 = 2 \tan^{-1} \left(\frac{D_P}{2E_r} \right), \quad (2.6)$$

where E_r is the eye relief. In this experiment, the eye relief is 20 mm, which provides a FOV of 64.8 degrees. A wide FOV can be achieved due to the close distance of the eyepiece lens. Second, when the PDCL operates as an optical window, the FOV limited by the out-coupler (θ_2) is determined by the angular-selectivity of VHG, which is 10.5 degrees on the FWHM criterion. Thirdly, in the lens mode, the distance of a virtual image plane has repercussions on the effective FOV (θ_3). The size of virtual images in lens mode is reduced by the focal power of the PDCL. The ratio of the image size between operating modes (m) can be derived using the trigonometric ratio, which is given as:

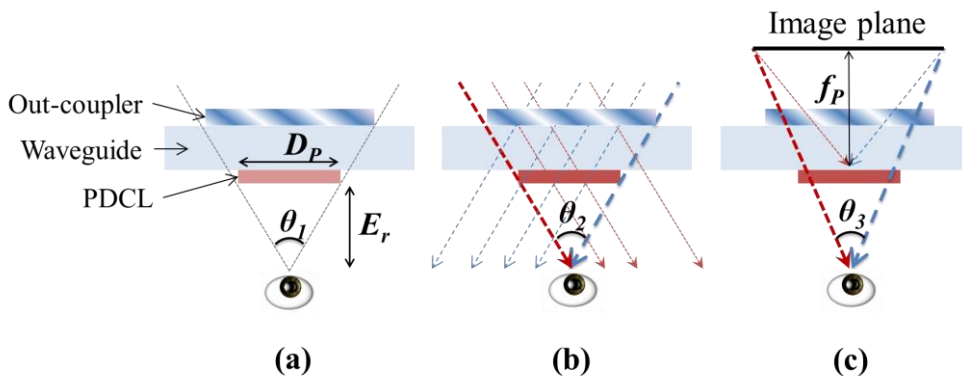


Figure 2.14 Schematic diagram of effective FOV (a) by the PDCL, (b) in window mode, and (c) in lens mode.

$$m = \frac{S_{inf}}{S_{lens}} = 1 + \frac{E_r}{|f_P|}, \quad (2.7)$$

where S_{inf} is the size of the retinal image for window mode, and S_{lens} is that for lens mode. The effective FOV also decreases in proportion to the image size, which can be given as:

$$\theta_3 = 2 \tan^{-1} \left[\frac{\tan(\theta_2/2)}{m} \right]. \quad (2.8)$$

By applying the specification in the experiment, the calculated FOV for lens mode is 7.5 degrees. To sum up, the effective FOV of the proposed configuration is dependent on the operation mode and focal power of PDCL. The prototype system provides a monocular FOV of 7.5 to 10.5 degrees along the horizontal axis. Both the FOV and the ratio of image size are sharply converged as the focal length of the PDCL becomes longer. By using the PDCL with a focal length greater than 180 mm, the difference between the two modes is less than 10%, as shown in the dotted line of Fig. 2.15.

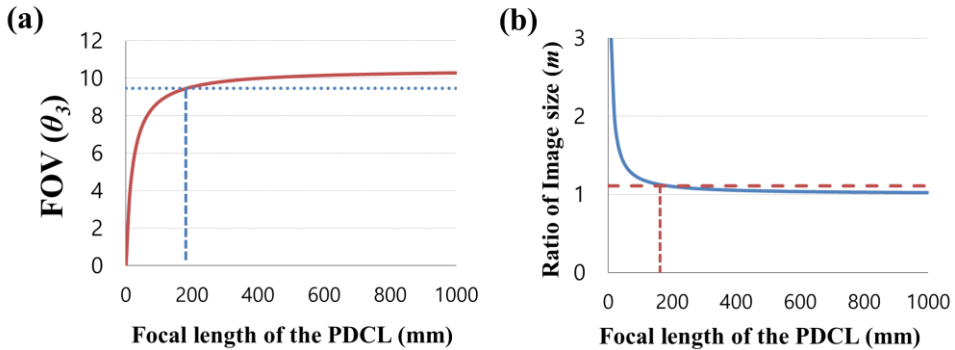


Figure 2.15 (a) Effective FOV for lens mode depending on the focal length of PDCL. (b) Ratio of image size between both operating modes.

In the third parameter, angular resolution is inversely proportional to the FOV, as in Eq. 1.7. For window mode, the angular resolution (Θ_{inf}) can be given as:

$$\Theta_{inf} = \frac{N_D}{2\alpha_D}, \quad (2.9)$$

where N_D is the pixel resolution of LSP, and α_D is the divergence angle of LSP. When calculated by the specifications of the LSP used in the experiment, Θ_{inf} is about 15 cpd. The angular resolution for lens mode (Θ_{lens}) is modulated by the FOV ratio between both operating modes, which can be calculated as follows:

$$\Theta_{lens} = \frac{\theta_2}{\theta_3} \Theta_{inf}. \quad (2.10)$$

By applying the specification in the experiment, the enhanced angular resolution for lens mode is 20.8 cpd. Since the retinal image size is related to angular resolution, this difference for the operating mode should be small to form uniform resolution within them. The actual resolution may be degraded from the calculated value by various factors of the waveguide system, such as waveguide flatness, scattering effect, wavefront distortion of VHG, and optical aberration of GPHLs.

In the fourth parameter, the optical efficiency of the proposed system is measured using the optical power meter and compared with the theoretical value. The measured optical power and efficiency are presented in Table 2.3. This efficiency results are the sum of all the output beams entering the exit-pupil formed about 20 mm. For both real scene and virtual images, the optical efficiency is limited to a maximum of 25% by the two polarizing plates along the optical path. In order to verify the measured values, theoretically detailed analysis is performed.

Table 2.3 Measured optical power and efficiency.

Index		Power	Efficiency
Real scene	Input	1.05 mW	18.5%
	Transmission	0.194 mW	
Virtual image	Input	698 nW	-
	Lens mode	138 nW	19.8%
	Window mode	31 nW	4.4%

For real scenes, the optical efficiency (η_R) is reduced by the polarization absorption of the linear polarizer and the circular polarizer in the PDCL and quadruplicate Fresnel reflections, which can be given as follows:

$$\eta_R = \eta_{pol}^2 \cdot (1 - \eta_f)^5, \quad (2.11)$$

where η_{pol} is the transmission efficiency of the polarizer (~46%), and η_f is the Fresnel loss. The theoretically calculated η_R for the on-axis condition is about 17.3%, similar to the experimental result.

For virtual image, the optical efficiency varies depending on the operating mode in which the polarization states of the input beam are orthogonal to each other. The VHG's diffraction efficiency for polarization state can be calculated based on the coupled wave theory (CWT) [48], which can be expressed as follows:

$$\eta_{TM} = \eta_{TE} \cdot \cos^2 2(\theta_B - \theta_G), \quad (2.12)$$

where η_{TM} is the diffraction efficiency for TM mode, η_{TE} is the diffraction efficiency for TE mode, θ_B is the Bragg angle (i.e., incidence angle satisfying Bragg matching condition), and θ_G is the slanted angle of Bragg grating. In the VHG's recording

condition, the Bragg angle is zero degrees (on-axis), and θ_G is 30 degrees. The diffraction efficiency for TM mode (window mode) is 40% of that of TE mode (lens mode), as shown in Fig. 2.16.

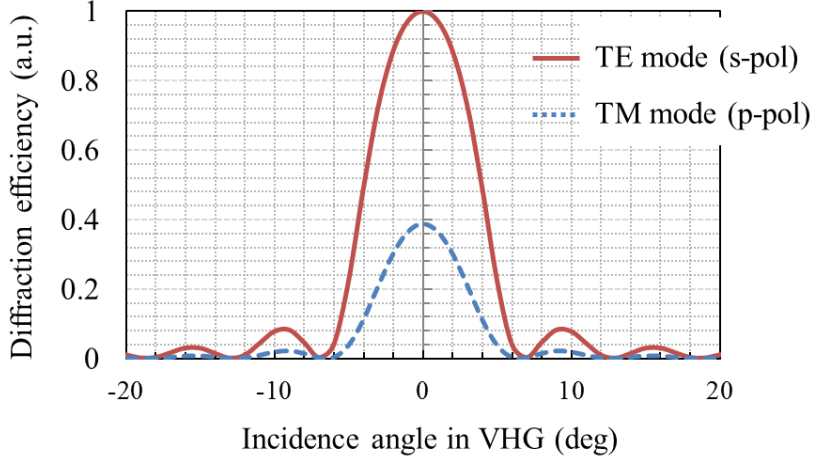


Figure 2.16 Calculated diffraction efficiency of VHG with different polarization states of input beam. The output value is normalized by the result of TE mode.

The optical efficiency for lens mode is about 2.5 times higher than that for see-through mode. For uniform brightness on two modes, actively adjustable light source interlocking with the polarizing rotator can be one solution. In the experiment, the brightness difference is compensated by adjusting the brightness of an input image with digital processing. For a virtual image, the total efficiency (η_V) of the whole system within the eyebox is as follows:

$$\eta_{V-TE/TM} = \eta_P \cdot \eta_+ \cdot (1 - \eta_f)^3 \cdot \eta_{TE/TM} \cdot \sum_n \eta_{TE/TM} \cdot (1 - \eta_{TE/TM})^{n-1}. \quad (2.13)$$

The above equation assumes that there is no optical loss due to scattering and is the sum of all the optical power of the exit pupil replicated in the eyebox. The

calculated η_{V-TE} is 22.4%, and η_{V-TM} is 5.1%, which is similar to the experimental result in Table 2.3 as well. Since the LSP has an ultrahigh brightness, the optical efficiency for virtual images is sufficient for the indoor room.

In this chapter, the key performances of the proposed system are theoretically and experimentally analyzed. This evaluation confirmed that the proposed system has the advantage of supporting the dual focal depth for a virtual image but has a disadvantage of optical efficiency drop. To resolve this efficiency issue, the author will discuss an improved optical structure. The efficiency drop is caused by the polarizer inserted for polarization control, which can be alleviated by changing the polarizer into an active device, as illustrated in Fig. 2.17. By replacing the circular polarizer within the PDCL with an active variable retarder with a thin form factor, the optical efficiency for virtual images can be improved by at least two times compared to the previous structure. Since the polarization state of the incident beam can always be fixed to the TE mode, it is possible to prevent the decrease in the diffraction efficiency of VHG. In this prototype system, the brightness for virtual images is enhanced by up to 8 times. Since the brightness compensation is not required according to the polarization mode, the computational load can be reduced. For real scenes, by replacing the linear polarizer attached to the out-coupler with an active barrier plate and synchronizing it with the active retarder in the PDCL, the efficiency for the real scene can be doubled compared to the previous configuration. These active optical devices can be implemented as a liquid crystal-based film or retarder with a high-speed switching [49]. However, the focal power of the GPHL may be adjusted by using the active retarder. Since the active retarder inserted in the PDCL generally uses two electrode substrates (e.g., ITO), the thickness becomes thicker than the circular polarizer. Due to the increase in the gap between the two GPHLs, the focal power may need to be slightly tuned to consider an effective focal length.

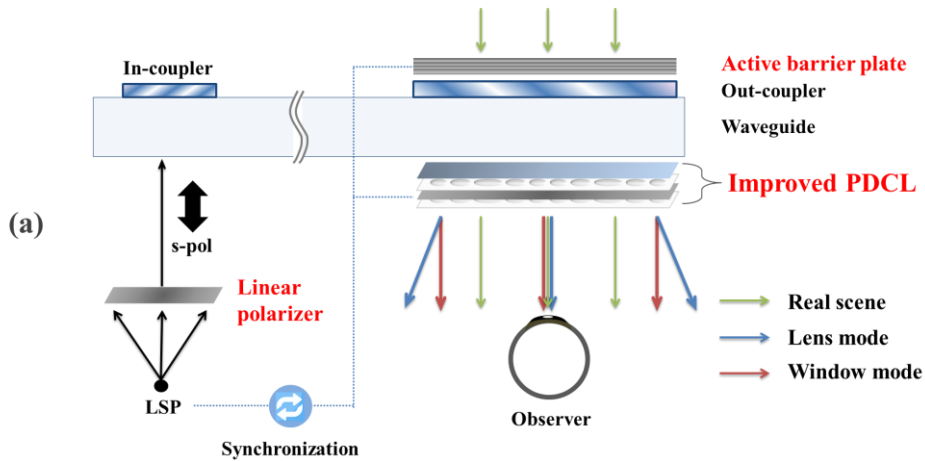


Figure 2.17 (a) Schematic diagram of improved configuration with active optical elements. Improved PDCL structure and polarization states (b) for lens mode and (c) for optical window mode.

The dual focal planes of the proposed system are insufficient to alleviate the VAC issue and provide sharp AR images at all times. The number of focal planes can be increased to more than two by employing the active structure mentioned above. Figure 2.18 presents an eyepiece-combiner with triple focal planes with active optics. Three operating modes can be implemented by overlapping a single GPHL with high optical power (D_1) and two GPHL with a small power (D_2).

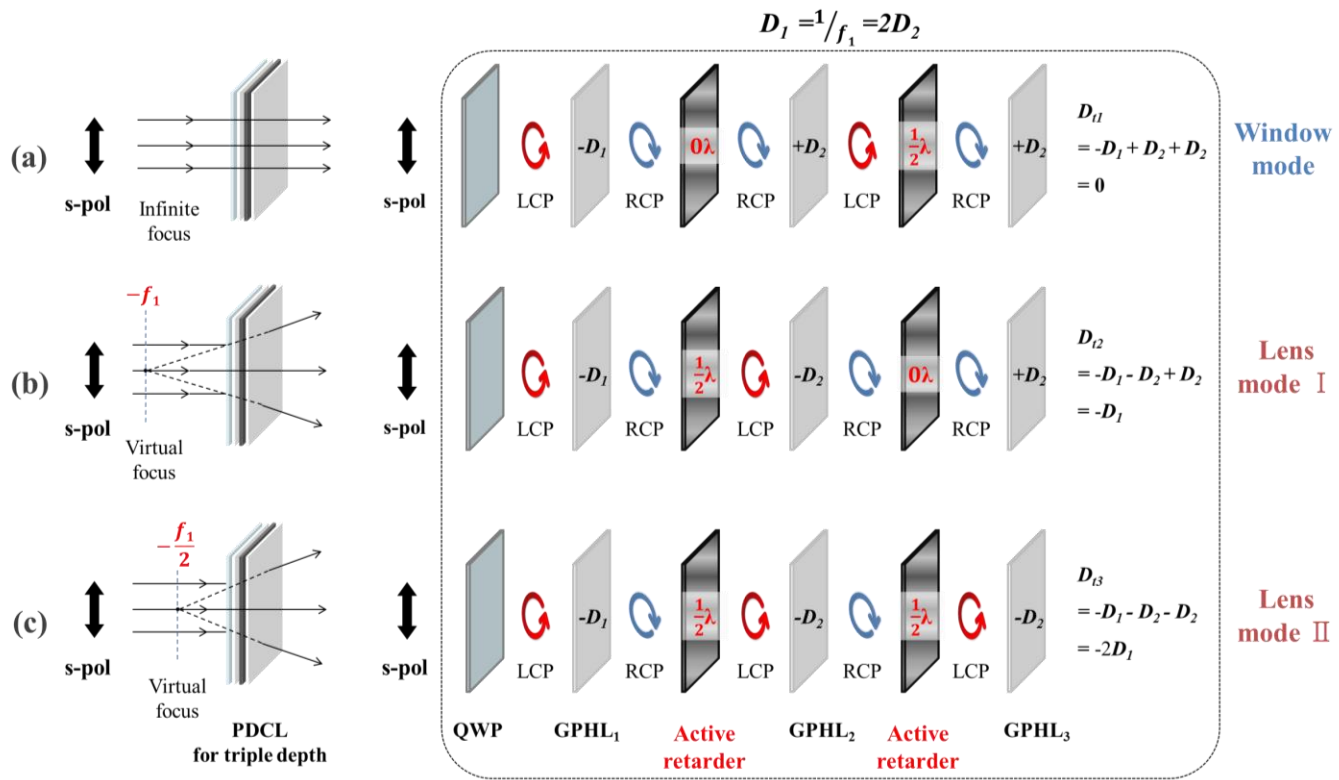


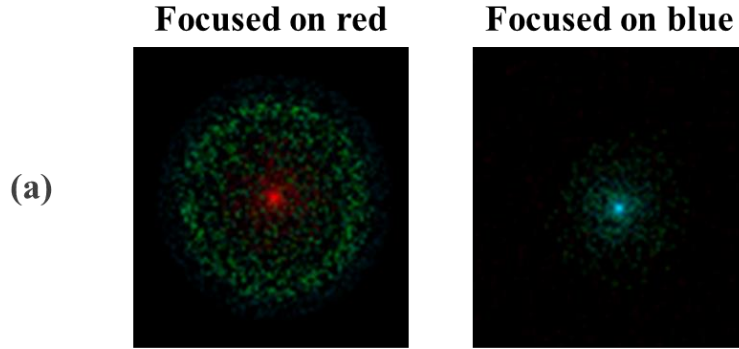
Figure 2.18 Schematic diagram of the modified PDCL structure and operating mode for triple focal planes.

Three focal planes can be formed with time multiplexing by synchronizing two active retarders inserted in the PDCL in real-time. Similarly, as stated above, the number of focal planes can be increased in proportion to the number of GPHL and active retarder. However, to provide a real-time AR image, there is a limitation in that the operating speed of the active optics and the PDCL thickness should be increased in proportion to it.

Despite the advantages of compact volume, multi-functionality, and high numerical aperture (NA), the geometric phase lens still has a critical limitation as an eyepiece for near-eye displays. Compared to traditional lenses, GPHLs have severe chromatic aberration. The phase profile for a geometric phase lens is given by [46]:

$$\varphi(\rho) = \frac{\pi\rho^2}{\lambda f}, \quad (2.14)$$

where ρ is the radius on the radial coordinates system. The phase shift (φ) determined by the refractive index and the optical axis of the anisotropic medium is constant regardless of the wavelength (λ). In other words, the product of the wavelength and the focal length is the same ($\lambda_1 f_1 = \lambda_2 f_2$) for the on-axis incident condition. Consequently, two parameters are inversely proportional to each other. When using a multi-wavelength light source for a full-color AR image, three different focal planes are formed according to each wavelength after passing through the GPHL, as shown in Fig. 2.19. When PDCL is fabricated using GPHL with chromatic aberration, the color separation issue occurs for virtual images in lens mode. The chromatic aberration is twice aggravated by repeated phase modulation of two GPHLs in the PDCL. On the other hand, for real scenes and virtual images in see-through mode, chromatic aberration is removed by the conjugated lens profile.



(b)

Designed focal length (mm)	Measured focal length (mm)		
	Red (656nm)	Green (532 nm)	Blue (486nm)
100	83.5	100	112.8

Figure 2.19 Chromatic aberration of GPHL: (a) simulation for focal spots and (b) measured focal length depending on the wavelength.

In order to resolve the chromatic aberration, an achromatic geometric phase lens should be required. The broadband achromatic lens can be implemented with a multi-layered metalens [50], a phase manipulated metalens [51], and broadband waveplate lenses [52]. To sum up, the chromatic focal shift can be mitigated by using an aberration-corrected geometric phase lens. Finally, the PDCL used in the experiment has a short focal length for the human eye. For practical use, the near-corrected virtual image should be rendered at reasonable distance near arm reach (~50 cm, 2 D) [53]. This adequate focal depth can be achieved with a longer focal length.

2.4 Conclusion

In this chapter, the author has proposed a waveguide-based AR near-eye display with dual-focal planes using a novel polarization-dependent eyepiece-combiner, which can selectively refract the incident light depending on the polarization state of the input beam. The proposed configuration enables dual-focal planes for virtual images with the polarization multiplexing method, which can improve the sharpness of virtual images superimposed on real objects and mitigate the visual fatigue by the VAC problem. In addition, the proposed eyepiece lens has a compact form factor of 1 mm thickness. This superior property is suited for AR displays. We have demonstrated a proof-of-concept system in which focal distances are located at infinity and 20 D, respectively. In addition, various display performances are quantitatively analyzed, and problems and limitations of the proposed system are discussed in detail. By additionally suggesting a modified system from the initially proposed configuration, it is proved that their problems can be mitigated. In summary, the proposed multi-focal technique for waveguide-based display will be a competitive solution for immersive and comfortable AR experiences.

Chapter 3 Extended-field-of-view waveguide-based near-eye display via polarization-dependent steering combiner

3.1 Introduction

In Chapter 1, the author discussed a promising waveguide technology among various methods of near-eye display. In Chapter 2, the author proposed a novel polarization-dependent eyepiece and waveguide architecture that can support focus cue, one of the major challenges of waveguide technology. In Chapter 3, the author will discuss a limitation of the FOV in the waveguide technology and a methodology to overcome this by using polarization multiplexing. As described in Chapter 1.3, the FOV (i.e., angle of view) depends on the TIR angle in the waveguide and angular bandwidth of the diffraction grating as imaging combiner, as shown in Fig. 3.1. In short, the diffraction efficiency and angle of the grating are directly related to the FOV.

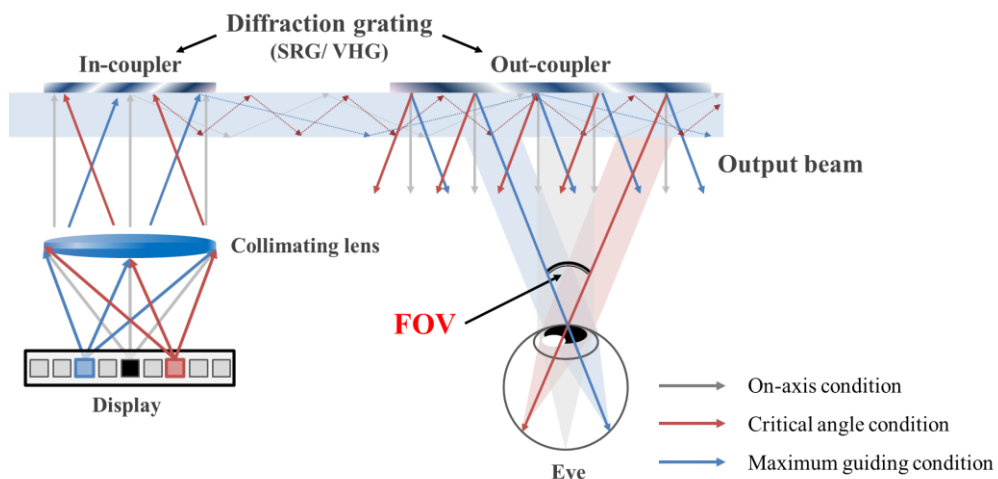


Figure 3.1 FOV in the waveguide-based near-eye display.

The grating-based combiners in released AR waveguide displays typically provide a mid-level FOV of approximately 30 to 40 degrees horizontally, as shown in Table 3.1, which is insufficient to provide immersive experiences [54]. To enlarge the FOV for more informative and realistic AR environments, various solutions have been proposed. In the SRG-based technique, a method of optimizing the grating parameters is widely used to extend the angular bandwidth of grating couplers [39]. Microsoft proposed a novel combiner structure with two intermediate couplers separated spatially [55]. In the VHG-based technique, several multiplexing techniques of VHGs have been reported. Han et al. proposed the spatially triple-multiplexing out-coupler VHG with an FOV of 27° in the air along the horizontal direction, but only a concept design of out-coupler and simulation results are presented [56]. Yu et al. experimentally implemented space-variant VHGs with an FOV of 20° , nearly identical to Han's method [57]. Shen et al. suggested a multilayered VHGs structure with an FOV of 28° based on the finite element method (FEM) simulation [58]. Recently, polarization volume gratings (PVGs) based on liquid crystals have been reported [59,60]. The liquid crystals have a higher refractive index than the conventional photopolymer, resulting in an FOV increase. Shi et al. proposed a novel waveguide-based configuration using metagratings with a horizontal FOV of 67° [61]. However, they did not demonstrate the prototype system experimentally, and the proposed system has limitations in vertical resolution and mass manufacturing due to alternate columns of the metagratings, which should be fabricated separately in the vertical direction.

In this chapter, the author proposes a waveguide-based AR near-eye display with an extended FOV using polarization gratings. In the proposed structure, the polarization gratings and polarization control plates are stacked on the front and the rear out-coupler part, which can support two different optical paths depending on the polarization state of the input beam. The polarization grating is very thin, with a

thickness of less than 1 mm. Consequently, the proposed structure with a compact form factor can provide an extended FOV.

Table 3.1 FOV performance of commercialized product or prototype.

	Hololens 1	Hololens 2	Magic Leap one	Rokid VISION	Vuzix Blade	Sony SED-E1
Type	SRG	SRG	SRG	SRG	SRG	VHG
Release date	2016.03	2019.11	2017.12	2020.Q1	2019.06	2016.06
FOV	30 deg (horizontal)	43 deg (horizontal)	40 deg (horizontal)	45 deg (diagonal)	28 deg (diagonal)	20 deg (diagonal)

3.2 Optical design for polarization-dependent steering combiner

3.2.1 Principle of polarization grating

A polarization-dependent steering combiner (PDSC) is based on the polarization grating, which selectively diffracts the incident beam in the \pm first-order depending on the polarization state of the input beam [62]. As the GPLH introduced in the previous chapter, the polarization grating is implemented by the geometric phase of the anisotropic medium. The polarization grating has a periodic phase pattern like conventional diffraction gratings, but the effective phase modulation merely depends on the polarization state of the incident light. Like other geometric phase optics, the polarization grating is fabricated using a photo-aligned liquid crystal (LC) polymer, metasurface, and plasmonic surface. In the case of using LC, the periodic structure is comprised of uniaxial birefringence LC molecules with an in-plane orientation angle (Φ) that varies linearly along a surface, as shown in Fig. 3.2.

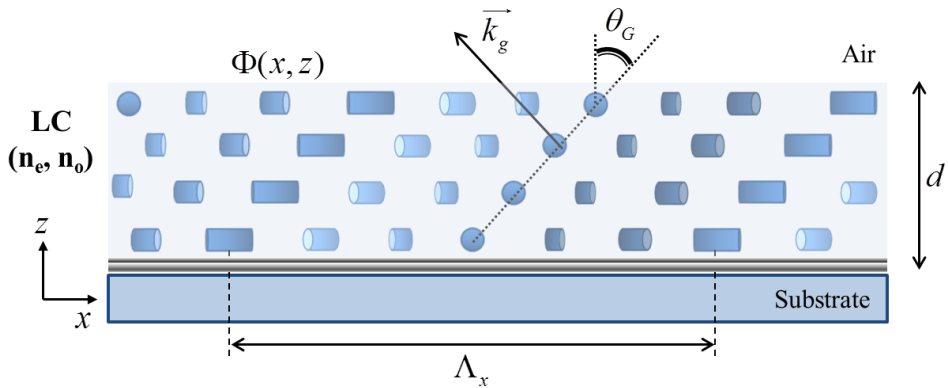


Figure 3.2 Schematic diagram of the LC-based Bragg polarization grating.

The Q parameter used to distinguish Raman-Nath (thin) grating and Bragg (volume) grating is defined as follows:

$$Q = \frac{2\pi\lambda d}{n\Lambda^2}, \quad (3.1)$$

where λ is the wavelength, d is the layer thickness, n is the average refractive index of the material, and Λ is the periodic spacing. Traditionally, A diffraction grating is considered to be a surface grating (Raman-Nath regime) when $Q < 1$, and a volume grating (Bragg regime) when $Q > 10$ [63]. If a liquid crystal layer is sufficiently thick, the volume grating effect is predominant. Consequentially, polarization gratings with sufficient thickness have the same properties as typical Bragg volume gratings due to periodic index modulation, except that they are composed of an anisotropic medium.

When a chiral LC is employed, as shown in Fig. 3.2, the orientation angle Φ is given as follows:

$$\Phi(x, z) = \frac{\pi x}{\Lambda_x} + \frac{\phi z}{d}, \quad (3.2)$$

where Φ is the twist angle of the LC layer, and Λ_x is the periodic spacing at the surface and can be determined by $\Lambda_x = \Lambda / \cos\theta_G$ where θ_G is the slanted angle of grating. The diffraction angle θ_m for m -th order is given as follows:

$$n_o \sin \theta_m = \frac{m\lambda}{\Lambda_x} + n_i \sin \theta_i \quad (3.3)$$

where n_o is the refractive index of the outer medium, n_i is the refractive index of the incident medium, and θ_i is the incident angle. For an ideal Bragg polarization grating with a high Q value, only diffracted beams with $m = \{-1, 0, 1\}$ can exist. For a thin grating at on-axis incidence (i.e., incidence angle with peak diffraction

efficiency is zero), the diffraction efficiency can be calculated as follows [64]:

$$\eta_0 = \cos^2\left(\frac{\pi\Delta nd}{\lambda}\right), \quad (3.4)$$

$$\eta_{\pm 1} = \frac{1 + |\overline{S}_3|}{2} \sin^2\left(\frac{\pi\Delta nd}{\lambda}\right), \quad (3.5)$$

where \overline{S}_3 is the normalized Stokes parameter corresponding to ellipticity (χ) (RCP: 1, LCP: -1). If the layer thickness is chosen as $d = \lambda/2\Delta n$ (half-wave plate), zero-order transmission (DC-term) will be zero ($\eta_0 = 0$), and the Bragg-matched incident light will be totally diffracted with first-orders without a loss ($\eta_{\pm 1} = 1$).

Because of the same operating principle as the geometric phase lens, the polarization grating can be fabricated in an ultra-thin film with high diffraction efficiency. The polarization gratings adopted in this experiment are transmissive-type products. Two circularly polarized input beams (LCP and RCP) are diffracted in opposite directions with respect to the surface normal with the same diffraction angle, as shown in Fig. 3.3.

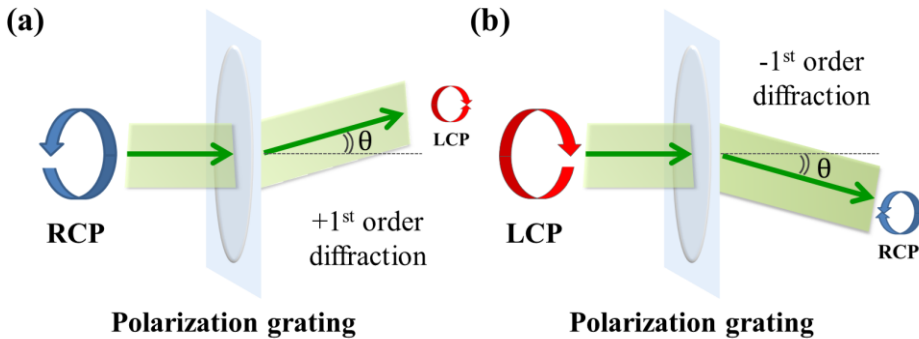


Figure 3.3 Illustration of the polarization grating (a) with a right-handed circular polarization (RCP) and (b) with a left-handed circular polarization (LCP).

3.2.2 Principle of polarization-dependent steering combiner

The proposed steering combiner can be divided into two parts: the FOV expanding part for virtual images and the compensation part for the real scene, as shown in Fig. 3.4. The waveguide, including the out-coupler, is sandwiched between the compensation and expansion parts. First, in the FOV expander, the QWP and the polarization grating are sequentially stacked on the backside waveguide (inward direction). The conventional planar waveguide can only preserve the polarization state of the input beam with linear polarization. Consequently, the input and output beam in the waveguide system is linearly polarized to use a polarization multiplexing. Similar to PDCL proposed in Chapter 2, the QWP is inserted to convert a linear polarization into a circular polarization before entering the polarization grating. In this experiment, by tilting the QWP with a 45° optical axis, the vertical polarization (V-pol) is converted to LCP, and the horizontal polarization (H-pol) is converted to RCP.

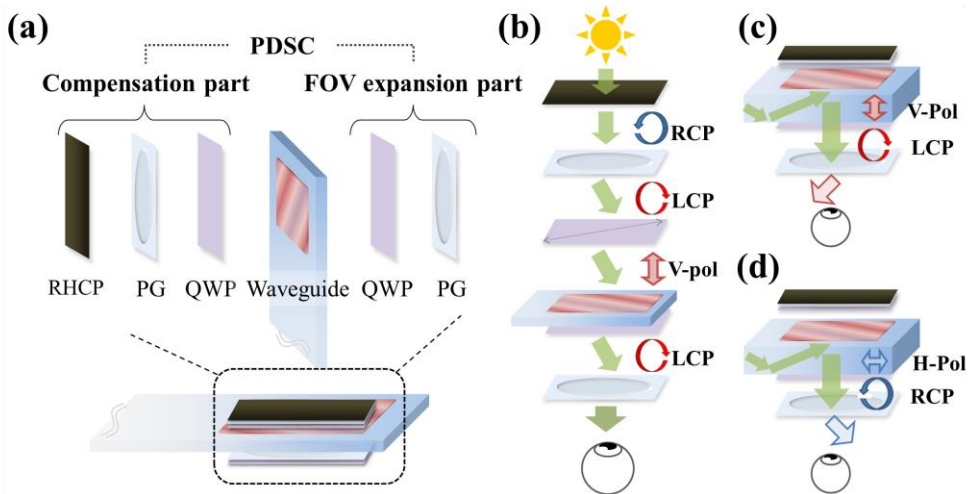


Figure 3.4 Schematic diagram of the (a) PDSC structure and the polarization state (b) for real scenes and (c), (d) for the virtual image with different polarization states, respectively. The polarization grating is abbreviated as PG.

As a result, the output beam passing through the polarization grating is split in two directions according to the polarization state, resulting in the FOV expansion with a single-channel waveguide, as shown in Figs. 3.4(c) and 3.4(d).

Second, the compensation part consists of the circular polarizer, polarization grating, and QWP, which are stacked on the foreside waveguide (outward direction) to countervail the distortion for the real scene by the polarization grating of the FOV expander part. The unpolarized light from the real object is circularly polarized by the uppermost right-handed circular polarizer (RHCP) and is deflected to the left or right direction by the outer polarization grating. By tilting the optical axis of the outer QWP perpendicular to the inner QWP, the cross-circular polarized light is incident on the polarization grating in the FOV expander part. The propagating light is diffracted in opposite directions compared to the compensation part. Therefore, this doublet structure can offset the diffraction effect for the real scene and have a see-through function as an optical window, as shown in Fig. 3.4(b). Since the proposed PDSC is composed of thin polarization-dependent film components, it has the advantage of being very thin (~1 mm). To support the EPE scheme, an air gap between the PDSC and the waveguide is required, but this gap does not compromise the advantages of the compact form factor.

3.2.3 Analysis and verification experiment for real-scene distortion

For minimizing the distortion for the real scene, two polarization gratings must be attached face-to-face. However, a gap between two polarization gratings is required for the waveguide and retarders. This gap should be narrow for low optical aberration. Here, the thickness of the waveguide and the retarder films usually is less than 1 mm, respectively, which is thin enough to observe the real-world scene with minimal distortion.

Figure 3.5 represents the simulation results based on ray tracing that show the focusing position and intensity distribution projected on the retina according to the

presence of the PDSC. The optical path and focal spot are slightly changed from their original positions. The PSF becomes broader compared to the original case.

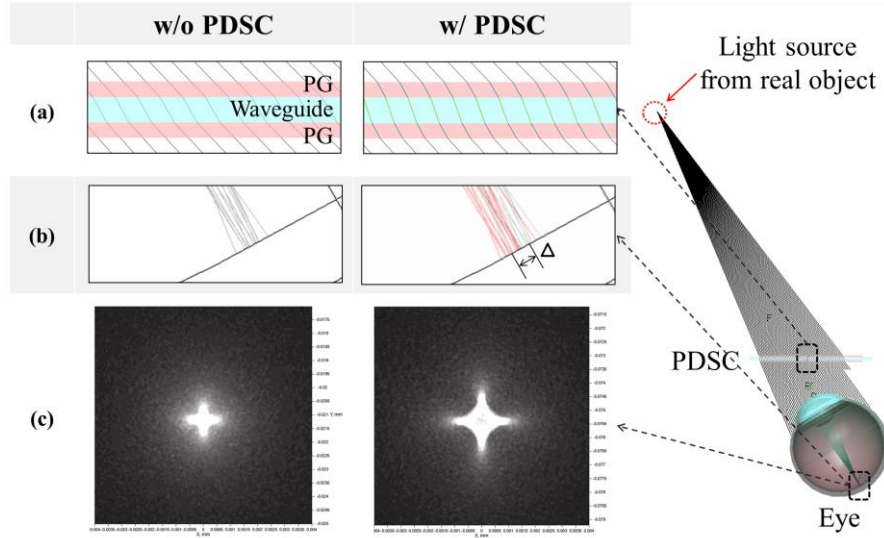


Figure 3.5 Ray tracing simulation layout and results for the real scene. By deactivating the polarization grating, the simulation is performed for the case without PDSC. (a) The optical path through the PDSC and waveguide. (b) The position of the focal point on the retina in the cross-section. The marked lines indicate the optical path to the retina. By inserting the PDSC, a lateral shift of the focal spot (Δ) occurs. (c) The intensity map of the focal spot on the retina. The polarization grating is abbreviated as PG.

The simulated MTF curves, according to the distance (z) of a real object and waveguide thickness (t_g), are depicted in Fig. 3.6. When the distance from the waveguide increases, the acceptance angle entering the PDSC aperture becomes smaller. Consequently, the shifting of the optical path by the polarization grating is reduced, which can maintain high resolution for the real scene. In the case of oblique incidence (off-axis), as the oblique angle (θ_{off}) increases, the MTF value is decreased due to the increment of the path difference within the gap. As an example, we set $t_g = 0.6$ mm, $z = 200$ mm, and $\theta_{off} = 30^\circ$; the cut-off frequency is

about 24 cpd to adopt an MTF criterion of 20%. This calculated value is insufficient for the 20/20 vision condition (i.e., 30 cpd). However, as the waveguide thickness decreases, the resolution quality is improved beyond 30 cpd. When the distance of the real object is 200 mm (5 D) or more, the MTF cut-off frequency exceeds 30 cpd.

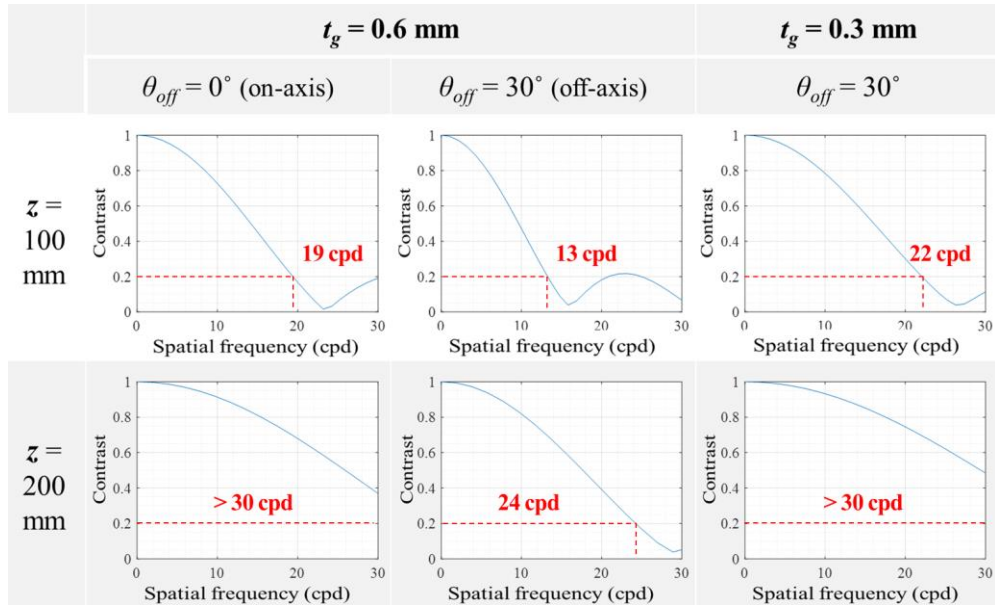


Figure 3.6 Simulated MTF curves of the proposed system for a real object.

Figure 3.7 shows the experimental results for the real object (USAF 1951 resolution target), which is located at 100 mm from the CCD camera. The MTF value for the real scene is acquired by calculating the contrast of test patterns. The measured MTF cut-off frequency is 15.8 cpd (35% criterion) in the conventional scheme, but the MTF for the proposed scheme with the PDSC is about 13.4 cpd. Considering that the measured MTF includes the optical aberration of the camera lens, the experimental result is similar to the simulation. The proposed method can be adopted in the general case of observing real objects over 5 D, considering the average adult's accommodation power (less than 5 D) [65].

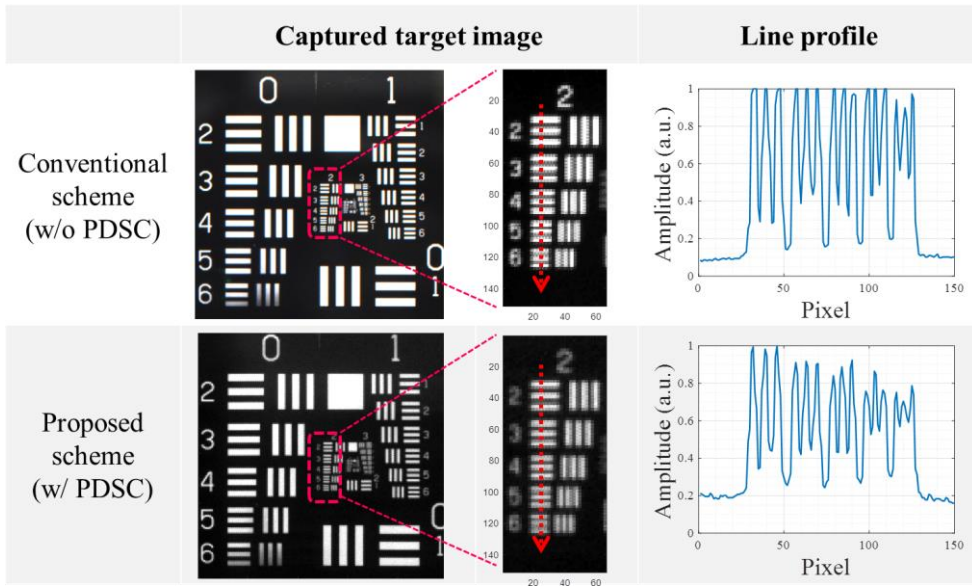


Figure 3.7 Photographs of experimental results: the captured target image and the line profile of the intensity across the dot arrow lines.

3.3 Waveguide-based augmented reality near-eye display with extended-field-of-view

3.3.1 Field-of-view for volume grating based waveguide technique

In this experiment, the reflection-type VHGs recorded in Bayfol® photopolymer film is used as the optical couplers. The VHGs can have high optical efficiency and negligible high-order diffraction due to their high angular selectivity and wavelength selectivity compared to the SRGs. However, excellent selectivity can typically cause the narrow angular bandwidth directly related to the FOV in diffraction-based waveguide techniques. The FOV is determined by the Bragg mismatching (Off-Bragg) condition of the VHGs, which can be calculated by using the beta-value expression of Uchida (BVM) [66]. This method suggested that the wavevector mismatching (Δk) is assumed to be attenuated along the thickness direction (z -axis). This constraint means that the transverse k -vector is conserved (modified conservation of momentum). Figure 3.8 shows the k -diagram for the VHG using the BVM method.

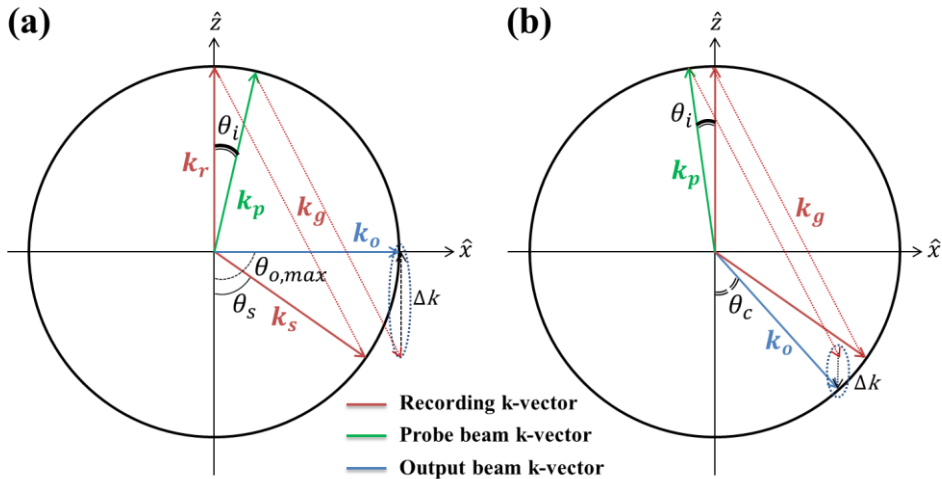


Figure 3.8 k -vector diagram of the reflection-type VHG. (a) Rightmost incidence condition and (b) leftmost condition under the TIR regime.

In the recording process, the grating vector (k_g) is determined by the wavevector of the reference beam (k_r) and the signal beam (k_s), which is defined as: $\vec{k}_r - \vec{k}_s = \vec{k}_g$, where the magnitude of the wavevector is $|\vec{k}_r| = |\vec{k}_s| = 2\pi n/\lambda$. The magnitude of the grating vector is given by $|\vec{k}_g| = 2\pi/\Lambda$, where Λ is the grating period.

In the reconstruction process, the diffraction angle is obtained by the vector sum of the probe beam's k -vector (k_p) and the grating vector k_g . When the probe beam is incident at the Bragg angle, the diffracted beam satisfies the Bragg matching condition: $\vec{k}_p + \vec{k}_g = \vec{k}_o$. On the other hand, if the incident angle is out of the Bragg angle, the Floquet condition in the BVM method is satisfied as follows: $\vec{k}_p + \vec{k}_g \pm \Delta k \vec{N} = \vec{k}_o$, where N vector is the VHG's surface normal vector, and Δk is a mismatching term, which is given as:

$$\Delta k = |\vec{k}_p| \cos \theta_i - |\vec{k}_g| \cos \theta_g - |\vec{k}_p| \cos \left(\sin^{-1}(\sin \theta_i + \sin \theta_g) \right). \quad (3.6)$$

The maximum incidence angle $\theta_{i,max}$ that allows Bragg diffraction can be obtained by using the k -diagram method, which is defined as:

$$\theta_{i,max} = \sin^{-1} \left(1 - \frac{|\vec{k}_g|}{|\vec{k}_p|} \sin \theta_g \right). \quad (3.7)$$

For waveguide-based near-eye displays, the diffraction angle is limited above the critical angle for the TIR condition. The maximum TIR angle is also limited to achieve an effective EPE scheme. The allowable incidence angle (θ_i) under the simple case, where the Bragg angle is zero, should satisfy the following inequality:

$$\frac{n_g}{n_v} \sin \theta_c \leq \frac{1}{n_v} \sin \theta_i + \sin \theta_s < \frac{n_g}{n_v} \sin \theta_{o,max}, \quad (3.8)$$

where n_g is the refractive index of the waveguide substrate, n_v is the refractive index of the VHG medium, θ_c is the critical angle satisfying the TIR condition, θ_s is the recording angle of the signal beam in the recording medium, and $\theta_{o,max}$ is the maximum guiding angle in a waveguide. In a general case where the refractive index of a waveguide and VHG medium are the same ($n_g = n_v$), the range of incidence angles satisfying the above inequality (i.e., maximum allowable FOV in the air (Θ) with a single waveguide) can be calculated as:

$$\Theta = \left| \sin^{-1} \left(n_g \cdot (\sin \theta_{o,max} - \sin \theta_s) \right) - \sin^{-1} \left(n_g \cdot (\sin \theta_c - \sin \theta_s) \right) \right|. \quad (3.9)$$

The n_v is typically 1.5 based on widely used photopolymer films. In this condition, the maximum FOV value is 29° in the air, where the $\theta_{o,max}$ is extremely 90° . Considering the EPE technique and the pupil diameter of the human eye, the practicable FOV is decreased by excluding the guiding light with a large TIR angle. As an example, if set $\theta_{o,max} = 75^\circ$, the reduced FOV is 25.9° . In the proposed configuration, the extended FOV (Θ_m) in the horizontal direction can be achieved with a PDSC, which can be approximately given as follows:

$$\Theta_m = \begin{cases} \Theta_{eff} + 2\theta_{PG} & \text{for } \Theta/2 > \theta_{PG} \\ 2\Theta_{eff} & \text{for } \Theta/2 \leq \theta_{PG} \end{cases}, \quad (3.10)$$

where θ_{eff} is the effective FOV taking into account the angular bandwidth of the recorded VHG, and θ_{PG} is the diffraction angle of the polarization grating. The extended FOV can maximally be increased up to twice the original FOV.

3.3.2 Implementation of the prototype and experimental results

The experimental setup is constructed on an optical table, as shown in Fig. 3.9. To implement the polarization-multiplexing technique for two orthogonal linear polarizations, we use two laser-scanning projectors (LSP) (Celluon PicoPro) and combine the optical path with a polarization beam splitter (PBS). The 1-D horizontal EPE scheme is adopted to ensure the sufficiently wide eyebox ($> 15\text{mm}$). A 4- f relay lens system is set up to focus the input beam on the in-coupler HOE, which can reserve the vertical FOV restricted by the 1-D EPE configuration. The thickness of the waveguide substrate is 0.6 mm, and the total thickness of the out-coupler part, including the PDSC, is less than 2 mm. The VHG combiners are recorded with a 532 nm laser and have a horizontal FOV θ_{eff} of 15 degrees on the FWHM criterion. We use the commercialized polarization gratings (Edmund Optics S/N: 12-677, 12-678) with a diffraction angle of 5° and 10° for 550 nm in the air.

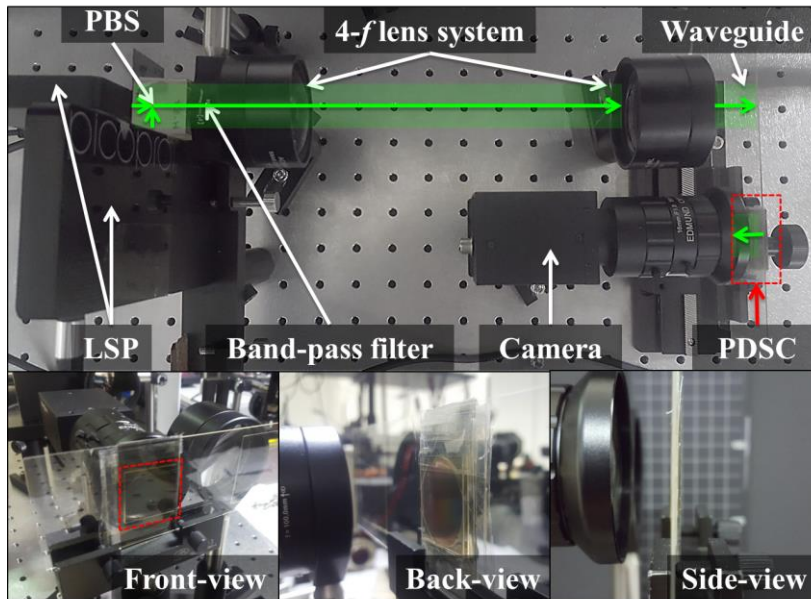


Figure 3.9 Benchtop prototype of proposed configuration. Arrow lines indicate the optical path of beams.

The display results are shown in Fig. 3.10, which is captured with an 8 mm or 16 mm focal length lens. The virtual image is rendered at infinity. Without the PDSC, the observed image has a horizontal 17° FOV. The output image with an extended FOV of 25.5° is obtained with the PDSC of the 5° diffraction angle. The extended FOV is 33.2° with a 10° PDSC. However, the discontinued images are observed in the middle area, as shown in Fig. 3.10(c). The diffraction angle of the PDSC should be less than half of the original FOV (θ_{eff}) for preventing this problem.

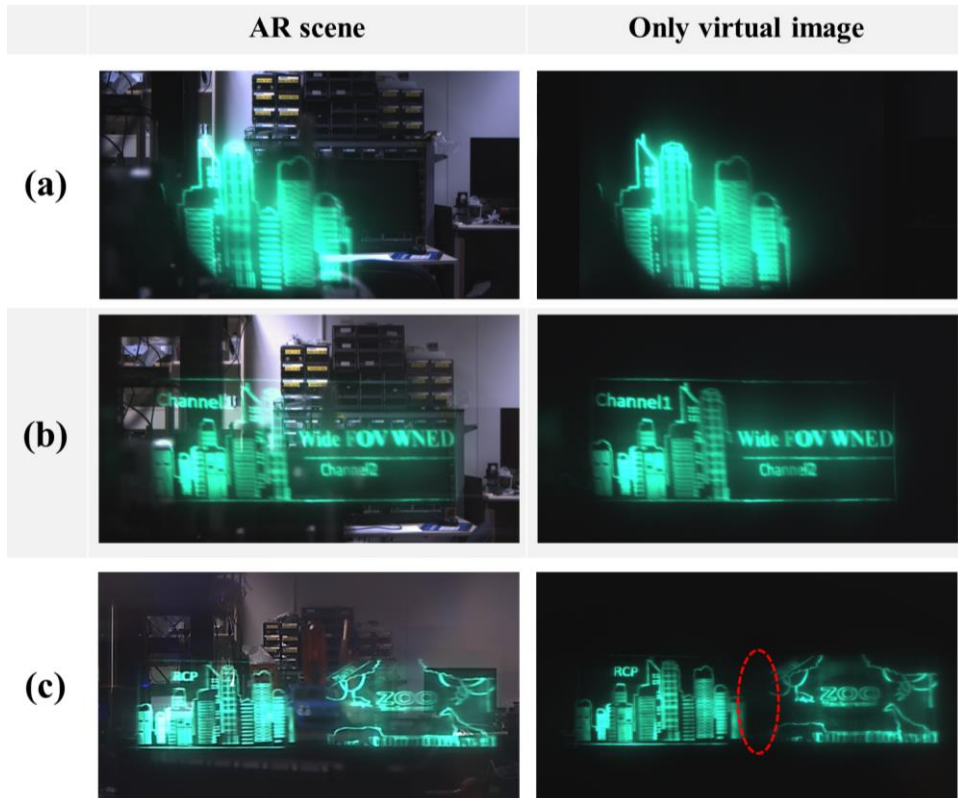


Figure 3.10 Experimental results: (a) without the PDSC (conventional system), (b) with the 5° PDSC, and (c) with the 10° PDSC. The red dot lines indicate the blank image area.

To verify the feasibility, we have demonstrated that the proposed configuration can expand the FOV under the monochromatic condition. The optical efficiency for the real scene is reduced by half due to a circular polarizer in the compensation part of the PDSC. This optical loss for real scenes is similar to the efficiency drop by the sun visor coating of commercialized AR devices.

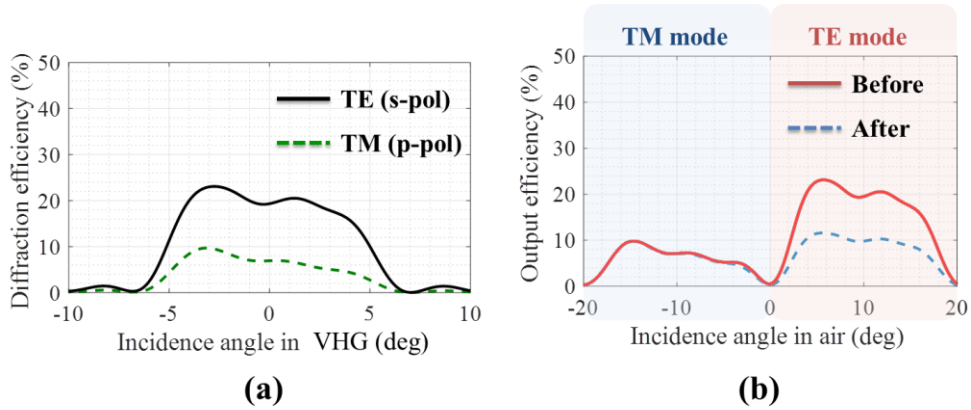


Figure 3.11 (a) Diffraction efficiency of the recorded VHG with two orthogonal linearly polarized input beams, respectively. (b) Output efficiency comparison before and after compensation when the 10° PDSC is adopted.

The simulated diffraction efficiency for the recorded VHGs, depending on the polarization state, is depicted in Fig. 3.11(a). As described in Chapter 2.3.2, the VHG's diffraction efficiency for TM mode is lower than that for TE mode. Therefore, in the proposed configuration, the intensity discrepancy for each polarization channel is compensated to improve the brightness uniformity. In this experiment, the brightness equalization is conducted by attaching an additional polarization film in front of the laser projector for TE mode and digitally modulating the grayscale of the virtual image.

3.3.3 Performances analysis and discussion

The extended FOV derived in Eq. 3.10 is an approximate equation obtained under the assumption that the display wavelength for virtual images and the design wavelength of the polarization grating are the same. As in the experimental condition, when the wavelength for display (532 nm) and the design wavelength (550 nm) are inconsistent, the diffraction angle slightly changes from Eq. 3.10. This relationship can be calculated with the following equation:

$$\theta_{PG} = \sin^{-1} \left(\sin \theta_i \pm \frac{\lambda}{\Lambda} \right), \quad (3.11)$$

where θ_{PG} is the diffracted angle by the polarization grating, θ_i is the incidence angle to the polarization grating in air, λ is the wavelength for display source, and Λ is the designed grating period of the polarization grating. The following equation defines the extended FOV according to the incidence wavelength:

$$\Theta_m = \begin{cases} 2 \sin^{-1} \left(\sin \theta_{i,\max} + \frac{\lambda}{\Lambda} \right) & \text{for } \Theta/2 > \theta_{PG} \\ 2 \left| \sin^{-1} \left(\sin \theta_{i,\max} + \frac{\lambda}{\Lambda} \right) - \sin^{-1} \left(\sin \theta_{i,\min} + \frac{\lambda}{\Lambda} \right) \right| & \text{for } \Theta/2 \leq \theta_{PG} \end{cases} \cdot (3.12)$$

As an example, we set $\theta_i = -10 \sim +10$ deg, $\lambda = 532$ nm, $\theta_{PG} = 10^\circ$ for 550 nm; the calculated FOV Θ_m is 39.95° , which is a tiny difference (0.05°) from the calculated FOV (40°) using the Eq. 3.10. A more accurate FOV can be calculated using the above equation. Therefore, it is suggested that the approximation equation (Eq. 3.10) is used to induce intuitive understanding.

The image quality degradation of the virtual image is not a major issue because the polarization grating merely changes the propagating direction of the

input beam. For measuring the distortion by the polarization grating, an experimental setup is constructed, as shown in Fig. 3.12(a). This setup consists of an LSP and a polarization grating to exclude distortion by the waveguide and VHG combiner. This is the equivalent model as the proposed system. Figure 3.12(b) shows that the display image is shifted laterally by the polarization grating, but the optical distortion cannot be observed. For an accurate comparison, the two captured images are overlapped each other. The two images are almost exactly matched except for minor differences caused by the camera lens. The mean square error (MSE) in the center area cropped by the dotted line is about 3.7.

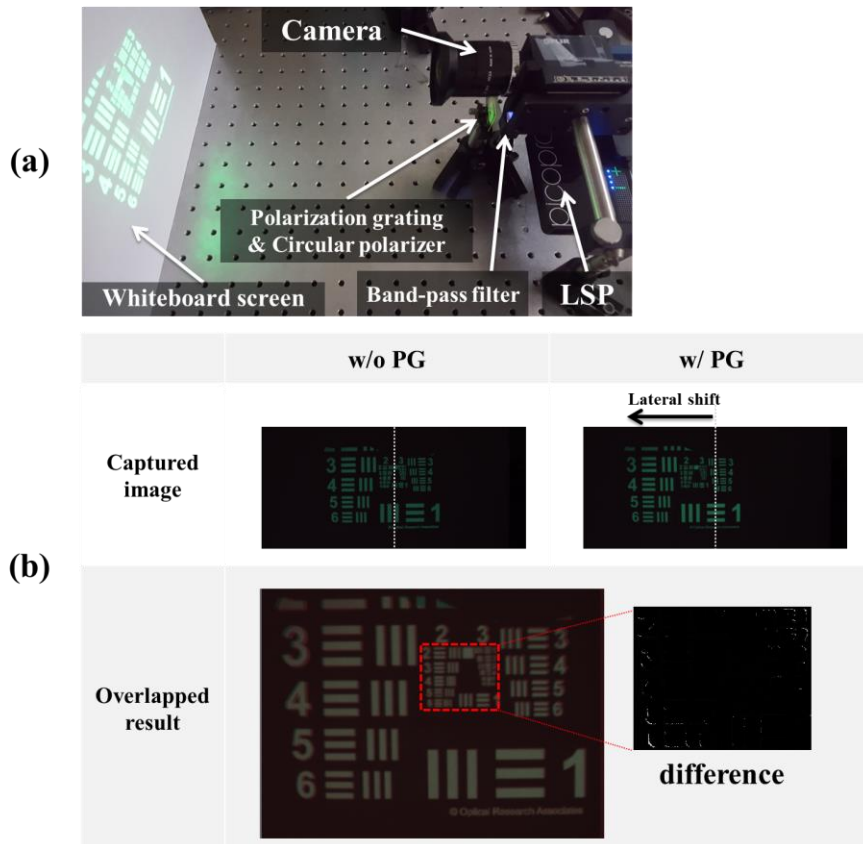


Figure 3.12 (a) Experimental setup for distortion verification. (b) Captured screen images and difference image between the original and the case with a polarization grating.

However, Figure 3.12(b) shows a tiny difference in the outer area of the two captured images. The diffraction angle by the PDSC is slightly changed according to the incidence angle because the polarization grating is a diffraction-based optical element. Figure 3.13 shows the diffraction angle according to the incidence angle when 10° polarization grating is used. The fluctuated diffraction angle causes the image lengthening in the image edge but is insignificant in the peripheral vision area of the human eye [67].

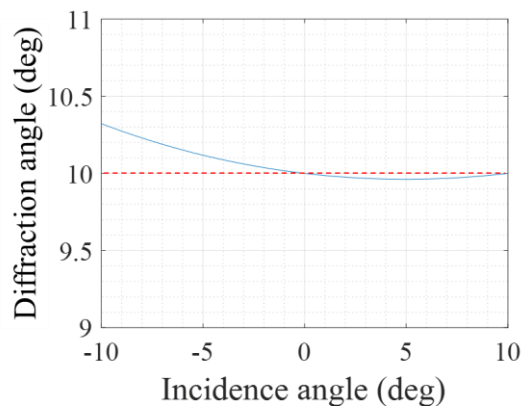


Figure 3.13 Diffraction angle of a polarization grating depending on the incidence angle.

Assuming as an ideal case where the input beam emitted from the single display pixel is incident at the same angle, MTF degradation does not occur by the polarization grating. If a single pixel has a finite size (actual case) or a display source with a Gaussian beam is adopted, such as an LSP, the input beam emitted from the single pixel is slightly diverged by the polarization grating, as shown in Fig. 3.14(a). This diverging effect can deteriorate the image quality. Figure 3.14(b) shows the simulated MTF results. The MTF contrast is decreased in the peripheral region of the FOV. However, this MTF degradation is insignificant in the peripheral vision area of the human eye [67].

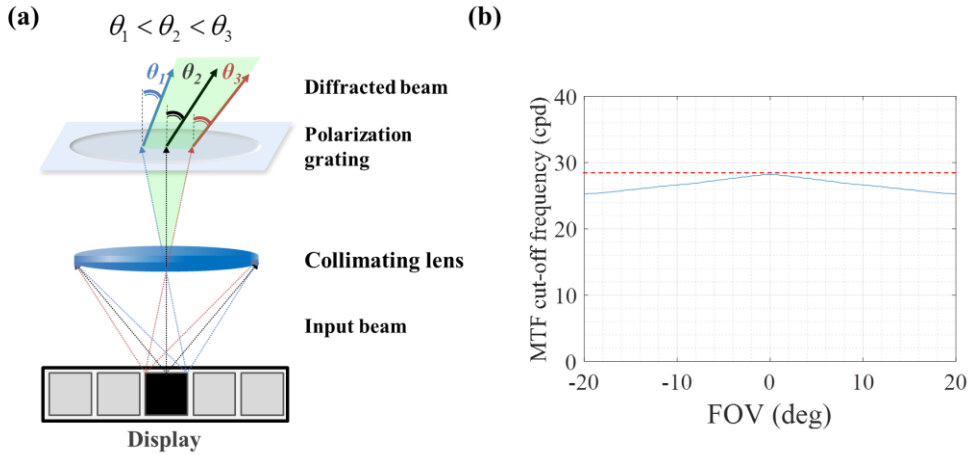


Figure 3.14 MTF degradation for virtual images: (a) beam divergence by finite pixel size, (b) simulation with a 10° polarization grating and HD-resolution LSP with a 40° diverging angle.

The proposed configuration for the extended FOV can be superimposed with the polarization-dependent combiner lens (PDCL) proposed for the dual-focal plane in Chapter 2. The waveguide system that provides two focal planes while extending the FOV can be realized by placing the PDCL behind a polarization grating. In this case, the polarization state of the output beam passing through the polarization grating is determined according to the polarization state of the input beam, which means that the PDCL operates only in one of the see-through or the lens mode for one optical path. This problem can be resolved by replacing the circular polarizer in the PDCL with an active variable retarder, as proposed in Fig. 2.17. In the case of using an active device, it is possible to implement both a see-through and a lens mode regardless of the polarization state of the input beam, but there is a trade-off relation in which the brightness decreases to 50%. Also, the polarization state of the input beam should be changed by temporal-polarization multiplexing. For real-time rendering, the operating speed of the active retarder should operate at around 240 Hz.

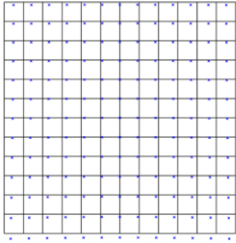
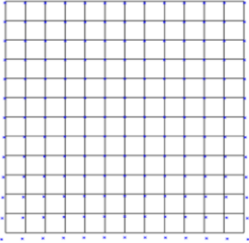
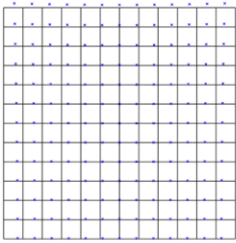
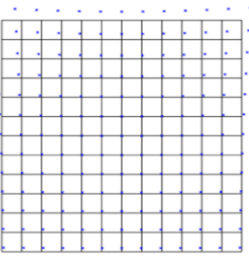
	w/o PDCL	w/ PDCL
w/o PG		
SMIA	0.40	0.96
w/ PG		
SMIA	0.56	1.53

Figure 3.15 Simulation results of the image distortion for virtual images depending on the PDCL and polarization grating.

Figure 3.15 represents the simulation results of the image distortion in Zemax software. The SMIA TV distortion metric is $(E - C) / C \times 100(\%)$, which E is the bottom-to-top distance at the edge, and C is the bottom-to-top distance at the center. For the normal condition (i.e., without the PDCL and the polarizing grating), minor distortion may occur due to the collimation lens. When both the polarization grating and PDCL are adopted, the grid distortion becomes more severe. However, the SMIA distortion does not exceed 2%, which is not conspicuously observed in a standard vision system. In addition, pincushion distortion that is noticeable at the edge side can be mitigated by digital image pre-compensation. These simulation results demonstrate that the distortion insignificant even when both the polarization grating and the PDCL are used.

3.4 Conclusion

In this chapter, the author proposes a novel eyepiece-combiner structure, which can extend the FOV up to twice with a compact form factor. We employed the polarization-dependent steering scheme to break through the FOV limitation determined by properties of the diffraction grating. We built a proof-of-concept system in which the horizontal FOV extends maximally two times with the single-channel waveguide. Even though the experimental FOV (33.2°) is somewhat less than that of commercial SRG-based near-eye displays, the FOV can be increased up to mid-50 degrees by adopting the proposed method without a high refractive index material. The proposed scheme can be applied to display the full-color image with the multilayered VHGs and achromatic polarization grating [68] that has a wavelength-independent diffraction angle. In addition, the proposed configuration can be powerfully utilized in combination with other FOV extension approaches, such as the angular and spatial multiplexing of the VHGs, which can resolve the narrow FOV issue in conventional waveguide-based near-eye displays.

Chapter 4 Viewpoint switchable retinal-projection-based near-eye display with waveguide configuration

4.1 Introduction

The waveguide technologies covered in Chapters 2 and 3 are based on diffraction-based optical combiners and collimation optics. In this approach, light from individual display pixels is incident on the waveguide as collimated light, coupled by a combiner, and then extracted as the same collimated light in front of the eye. In summary, the waveguide only performs the role of folding and duplicating the optical path. In this chapter, we will discuss a different type of display system where an out-coupler VHG has a converging lens function.

Retinal projection displays (RPDs), which are also known as Maxwellian-view displays, are based on a focus-free system [69-71]. The RPDs provide a wide range of acceptable sharp focus regardless of the accommodation response of the human eye. They can be implemented with a relatively simple configuration and a small form factor. As shown in Fig. 4.1(a), by focusing the light of display images on the pupil of the eye, an image can be directly projected onto the retina irrespective of the focal power of the crystalline lens. Focus-invariant systems can alleviate VAC problems compared to displays with a single focal plane [72]. Despite a simple configuration and wide DOF, RPDs have an intrinsic limitation: they provide a small eyebox around a focal spot. If the entrance pupil of the eye is out of the eyebox due to rotation of the eyeball and misalignment of the eye position, virtual images are blocked partially or entirely, as shown in Fig. 4.1(b). This limited eyebox is a major obstacle for the commercialization of the retinal projection-based near-eye display. To enlarge the size of the eyebox, several solutions have been proposed as follows.

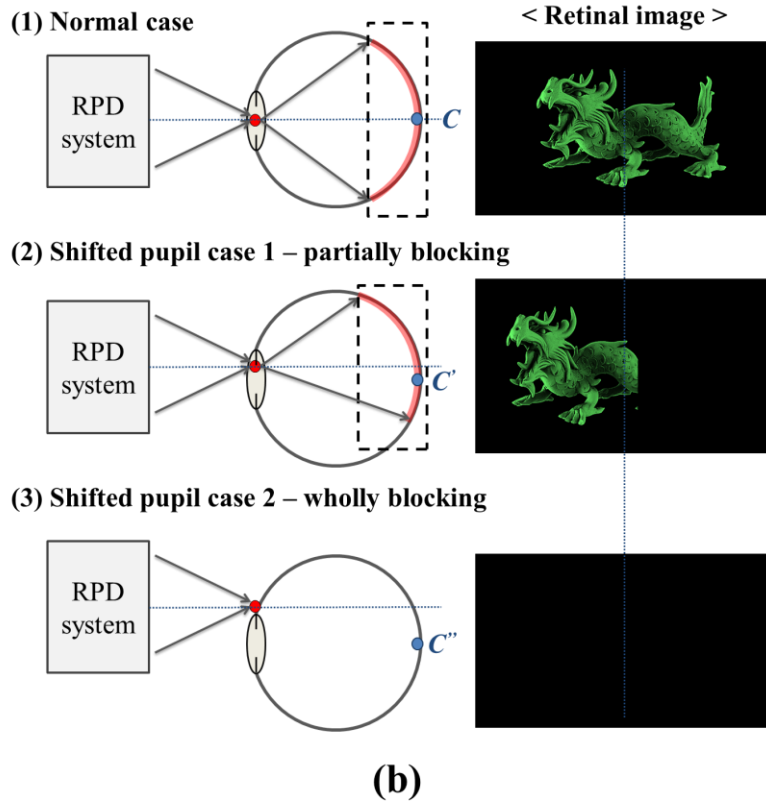
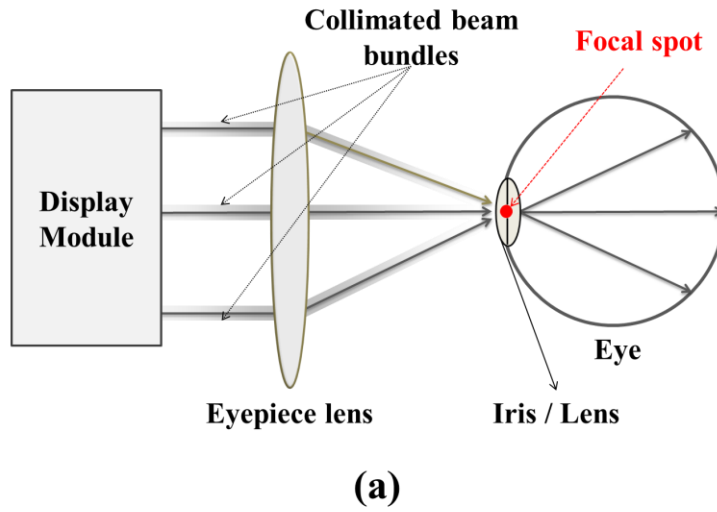


Figure 4.1 (a) Simplified configuration of the retinal projection display. (b) Illustration of retinal images according to pupil movement.

Jang et al. proposed a pupil-tracked RPD system using a lens-based holographic optical element (LHOE) as an imaging combiner and a steering mirror [47]. This system provides a dynamic eyebox, which can be realized by laterally shifting a focal point by the LHOE to track the movement of the pupil. Kim et al. suggested a dynamically moving focal point using a mechanically moving LHOE stage [73]. This approach is quite similar to Jang's approach but can provide a wider eyebox with shorter eye relief. Both of the methods, as above-mentioned, use mechanical movement of the optical element, which cause an increase in form factor or weight due to additional electro-motion components. Furthermore, if the moving speed is not fast enough, image sticking or lag may occur in real-time.

A steerable eyebox is realized using an array of light-emitting diodes (LEDs) synchronized with a pupil tracker by Hedili et al. [74]. This method can switch fixed focal spots with low motion-to-photon latency. However, an LED array light source inevitably increases the form factor of the display module. Kim et al. showed a lightguide-type RPD with an enlarged eyebox by the multiplexed HOE [44]. Jeong et al. suggested a customized LHOE combiner using a holographic printer [75], which can comfortably record an LHOE with a larger number of focal spots than Kim's method, and the vignetting problem is alleviated by finely adjusting the focal length for each viewpoint. This method using a multiplexed LHOE has the advantage that mechanical control is not required due to multiple and concurrent focal spots. However, due to always-on focal spots, double images or a blank image may be displayed depending on the pupil diameter and spacing between viewpoints, as shown in Figs. 4.2(b) and 4.2(c).

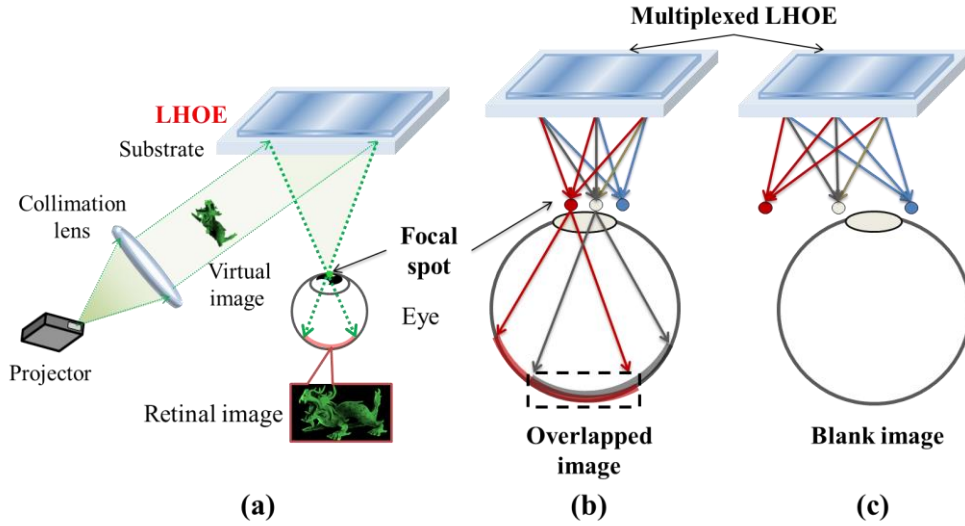


Figure 4.2 (a) Schematic diagram of the retinal projection-type near-eye display using an LHOE. (b) Illustration of the double image problem with a narrow viewpoint spacing and (c) blank image problem with wide viewpoint spacing in the RPD with multiple viewpoints.

In this chapter, the author proposes the retinal projection-based near-eye display enabling switchable viewpoints with polarization multiplexing and waveguide configuration. This active switching method is implemented by a polarization grating and multiplexed VHGs, which selectively change the diffraction angle of the output beam depending on the polarization state of the input beam. The proposed configuration divides the multiple focal spots into two modes to switch between each other. By employing the active control of viewpoints, image problems by multi-viewpoints can be mitigated. In addition, the proposed system has a wider DOF compared to the traditional waveguide-based near-eye display, which can provide a sharp image regardless of the vergence depth of the virtual image.

4.2 Polarization-dependent switchable eyebox

The goal of the proposed method is to provide an extended eyebox that can resolve the blank or double image problem in the waveguide-based RPD system with multiple focal spots. We designed to enable for switching between two viewpoint groups according to the pupil position, which alternately is located in the Sagittal plane. Polarization-dependent optical elements and multiplexed VHGs are employed to control the viewpoints switching depending on the polarization state.

4.2.1 Optical devices for polarization-dependent switching of viewpoints

First, the key element for implementing the switchable viewpoints is a polarization grating that controls the incidence angle on the in-coupler depending on the polarization state of the input beam. The transmission-type polarization grating diffracts an incident beam into two transmitted beams with opposite circular polarization states, as described in Chapter 3. Based on such advantages as the high-efficiency and form-factor property, the polarization grating can be used as a beam steering optics without mechanical movement [76]. The polarization grating used in the experiments diffracts the input beam with the right-handed circular polarization (RCP) in a clockwise tilted direction; whereas diffracts the input beam with the left-handed circular polarization (LCP) in a counterclockwise tilted direction, as shown in the mirror symmetry in Fig. 3.3.

Second, the waveguide is used to deliver a collimated virtual image to the eyes of users with a small form factor. By employing the waveguide configuration, the design flexibility of the entire system can be improved compared to free-space propagation (FSP) methods in which the input beam from the display module propagates into the air and directly enters the imaging combiner. In the glasses-type RPD with FSP methods, the incidence angle on the imaging combiner is limited due to the bone structure of the skull. Moreover, the angular resolution and

the spatial uniformity of the angular resolution depend on the inclination angle of the input beam, as shown in Fig. 4.3 [73]. The angular-varying resolution problem hinders immersive experiences and causes visual discomfort [77]. Meanwhile, in the waveguide structure, the propagation angle of the input beam is determined by the diffraction-based combiner, which can mitigate these issues by designing the light source module undeterred by the incidence angle.

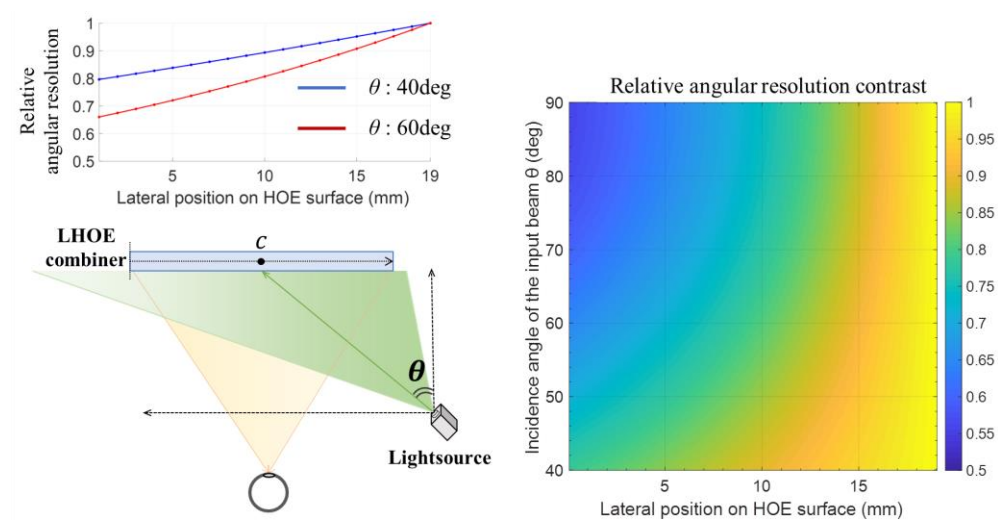


Figure 4.3 Spatial distribution of the angular resolution depending on the incidence angle of the input beam (θ). In the free-space propagation method, the incidence angle toward the center point of the LHOE (C) is changed to provide the dynamic eyebox. The simulation is conducted under the following conditions; θ : $40^\circ \sim 90^\circ$, LHOE lateral size: 19 mm, eye relief: 20 mm, and divergence angle of the light source: 30° .

Thirdly, VHGs introduced in the previous chapter is adopted as the in-coupler and out-coupler. The in-coupler VHG is recorded using the angular-multiplexing technique [78] so that two separate input beams entering the waveguide at different angles by the polarization grating are diffracted at different guiding angles with high efficiency. Similarly, the out-coupler is multiplexed to form multiple viewpoints. In the recording process of the out-coupler VHGs, the recording angle

of the reference beam is the same as the propagating angles within the waveguide, and the recording angle of the signal beam is predetermined in consideration of the position of viewpoints, which will be concretely described in following Section 4.2.3. In Fig. 4.4, we assume that the multiplexed diffraction angles of the in-coupler are θ_{i1} and θ_{i2} , and out-coupler angles are defined as θ_{o1} and θ_{o2} , respectively. The out-coupler is recorded to be paired with θ_{o1} for incidence angle θ_{i1} and with θ_{o2} for θ_{i2} . This approach can form viewpoints at different positions, depending on the guiding angle.

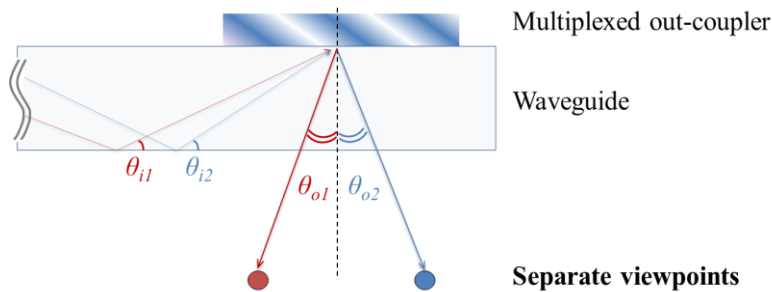


Figure 4.4 Schematic diagram of the angular-multiplexed out-coupler; the output beam is selectively diffracted depending on the guiding angle, which is presented in different colors.

Fourthly, a polarization-dependent eyepiece lens (PDEL) using geometric phase lenses (GPLs) is utilized as the converging lens to obtain a high NA. Figure 4.5 shows the operating mode of the PDEL, which is composed of a quarter-wave plate (QWP), two GPLs, and a right-handed circular polarizer (RHCP). By inserting an RHCP between two GPL with the same focal length and stacking them, the PDEL operates as an optically transparent window or convex lens depending on the polarization of the input beam. The front-most QWP converts linearly polarized real scene and virtual image into circularly polarized light, which is essential in a waveguide system where only guided beams with linear polarization can retain their polarization state, which will be discussed in detail in Section 4.3.2.

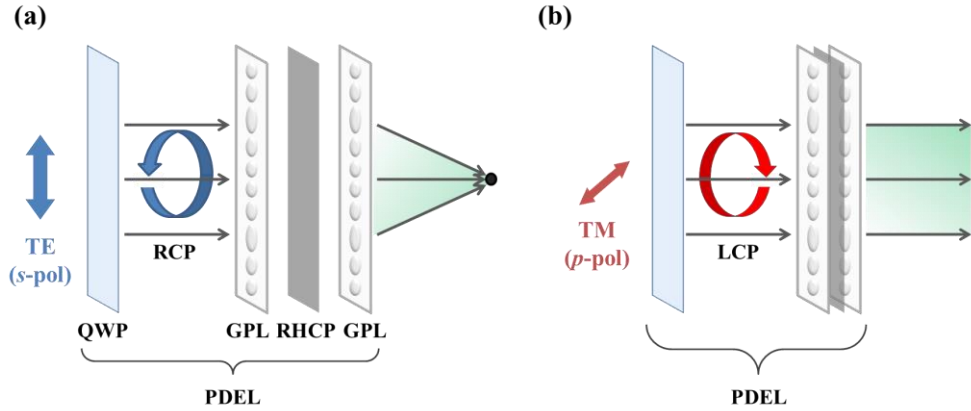


Figure 4.5 Illustration of the composition of the PDEL and operating mode depending on the polarization state; (a) lens mode for virtual images and (b) optical windows mode for real scenes.

4.2.2 System configuration for proposed method

The two-dimensional schematic diagram of the proposed waveguide-based RPD with switchable multi-viewpoints is illustrated in Fig. 4.6. A laser-scanning projector (LSP) and collimating lens are used to implement a retinal projection scheme with narrow spectral bandwidth. The polarization of the input beam is converted to RCP or LCP by a polarization rotator. A vertical linear polarizer is placed behind the polarization grating to convert the circularly polarized beam into linearly polarized light before entering the waveguide. Similarly, a horizontal linear polarizer is located in front of the out-coupler so that the PDEL acts as an optical window.

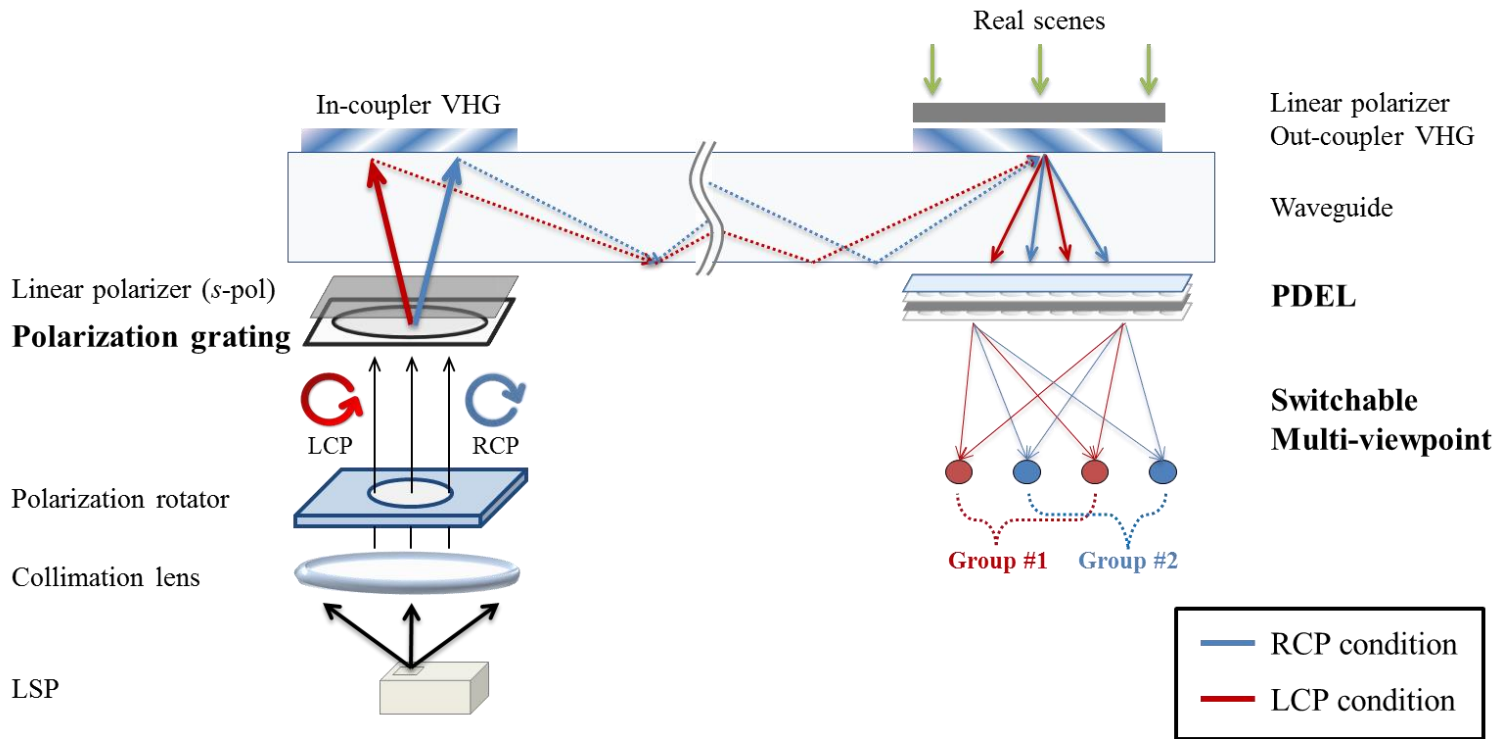


Figure 4.6 Schematic diagram of the proposed configuration. Each red line shows a beam path with LCP, and each blue line shows a beam path with RCP. The LCP and RCP are controlled by polarization.

As described above, the input beam, passing through the polarization grating, becomes to be incident on the in-coupler at different angles according to polarization state and propagates at different guiding angles. The multiplexed out-coupler allows guided beams at different angles to diffract in different directions to the incidence plane. The output beams split into two groups are focused by the PDEL for the retinal projection. Consequently, only one viewpoint group closest to the pupil position detected by the pupil tracker can be activated by controlling the polarization of input beam. The proposed configuration can solve the double image problem caused by duplicated viewpoints by switching between two groups according to pupil location. Additional thin optical components used for viewpoint control enable a compact and lightweight RPD system for an extended eyebox.

The waveguide structure using the VHG combiner is adopted for a flexible design of the form factor. In representative waveguide-based near-eye displays such as Microsoft HoloLens and Magic Leap One, the eyebox is enlarged using the EPE technique. However, the EPE scheme cannot be intactly applied to the waveguide-based RPD system in which all input beams are diffracted by the imaging combiner at the same guiding angle. This operating principle is different from the typical waveguide method using the EPE technique.

In the optical configuration of the RPD, the VHG's surface is equal to the projection plane of virtual images. Consequently, the size and location of the VHG combiner are required to match collimated input beams. If these design requirements are not satisfied, an unwanted or distorted image may be displayed. Figure 4.7 shows an illustrative case under various mismatching conditions.

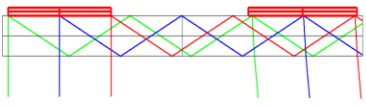
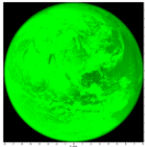
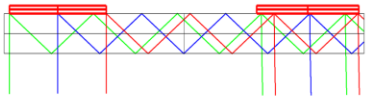
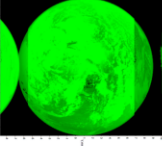
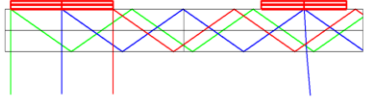
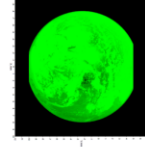
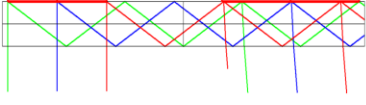
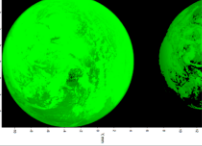
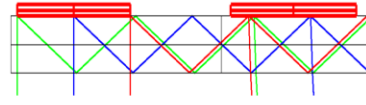
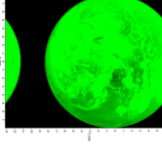
Layout of simulation model	Retinal image	Conditions	Problems
(a) 		Matching case	-
(b) 		Small guiding angle	Overlapping
(c) 		Small out-coupler	Clipping
(d) 		Large out-coupler	Duplication (double image)
(e) 		Mislocation of center point	Reverse or clipping

Figure 4.7 Optical misdesign classification. The simulation results are obtained by changing the size and position of the imaging combiners or the diffraction angle using ray-tracing software (LightTools).

Due to the design constraints of the imaging combiner, simple mechanical steering of the input source is subject to restrictions for expanding the eyebox in the waveguide structure. Figure 4.8 presents the FOV graph concerning the change of the incidence angle of the display source. This result reveals that the FOV is sharply reduced as rotating the input beam. The eyebox expansion (~3 mm) by focus shift is insufficient to cover pupil movement due to the eye rotation.

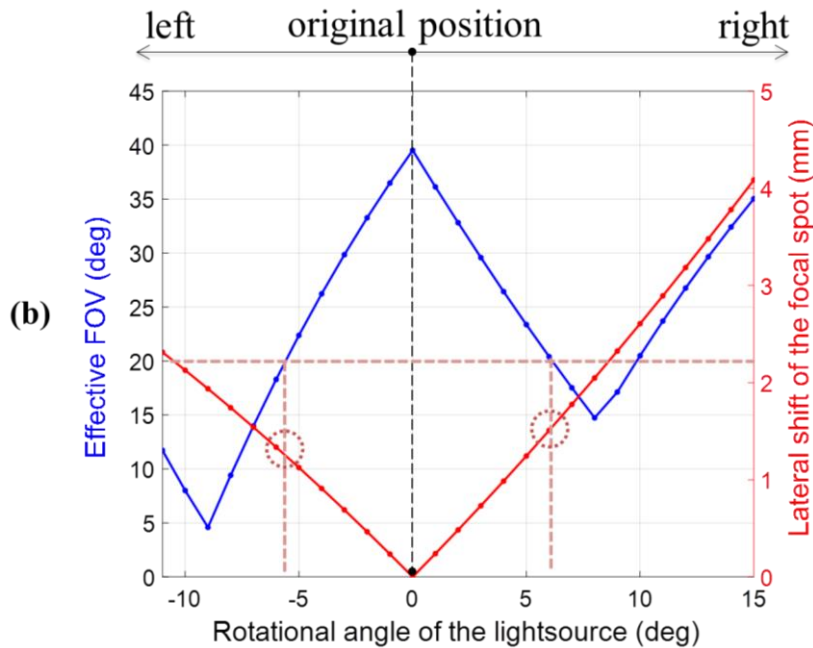
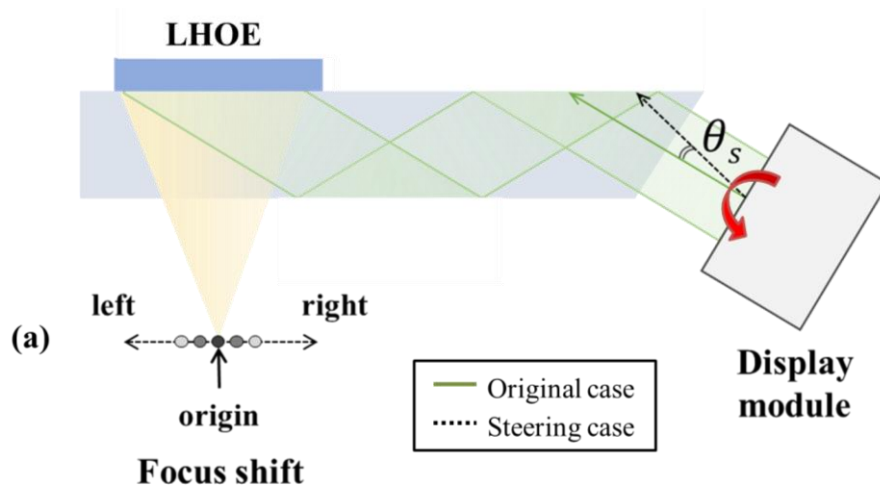


Figure 4.8 (a) Eyebox expansion by steering of the input light source in the wedge-shaped lightguide. (b) Focal spot is shifted by inducing Bragg mismatching condition. The simulation results show that the lateral shifted distance of the focal spot is 1.2 mm in a leftward direction and 1.3 mm in a rightward direction based on half of the original FOV. The simulation condition is as follows: the thickness of lightguide is 7 mm, the slanted angle of the wedge is 60° , and eye relief is 20 mm.

To guide the two split input beams from the in-coupler to the out-coupler without distortion of the original image, the guiding angle and the size and position of imaging couplers should be optimized. We adopted a planar waveguide with both in-coupler and out-coupler. The optical design of the planar waveguide is less constrained than the wedge-type lightguide in which the incidence angle of the input beam is limited by the wedge angle [34]. Also, in the wedge lightguide, the aspect ratio is modulated by the incidence angle, which causes additional image calibrations to provide the same image regardless of the viewpoint shifting.

4.2.3 Design of waveguide and imaging combiner

The overall system is determined by several key design parameters: (1) the thickness of the waveguide (d), (2) the length of the waveguide (L), (3) the guiding angle (θ_g) by the in-coupler, (4) the width of the projection plane on VHGs (w_{VHG}), (5) the diffraction angle of the polarization grating (θ_p) and (6) the focal length of the GPL (f_{GP}). We can assume that the distance between the polarization grating and waveguide and the thickness of polarization-dependent optical elements are negligible because of their thinness. For optimizing the waveguide system parameters, the following requirements should be considered. First, the maximum allowable FOV (MAFOV) Θ_{\max} of the RPD system is defined by:

$$\Theta_{\max} = 2 \tan^{-1} \left(\frac{w_{HOE} / 2}{d_{eye}} \right), \quad (4.1)$$

where d_{eye} is the eye relief, which is equal to half the focal length of a GPL. The width of VHGs w_{VHG} becomes larger as the target FOV increases, as determined by Eq. 4.1. To avoid image problems presented in Fig. 4.7, the following equation should be satisfied:

$$w_{HOE} < 2d \tan \theta_g. \quad (4.2)$$

In Eq. 4.2, the w_{HOE} is limited by the guide thickness and the guiding angle. Consequently, increasing the waveguide thickness allows a wider FOV but results in a bulky form factor. Figure 4.9 shows the performance relationship between various design parameters.

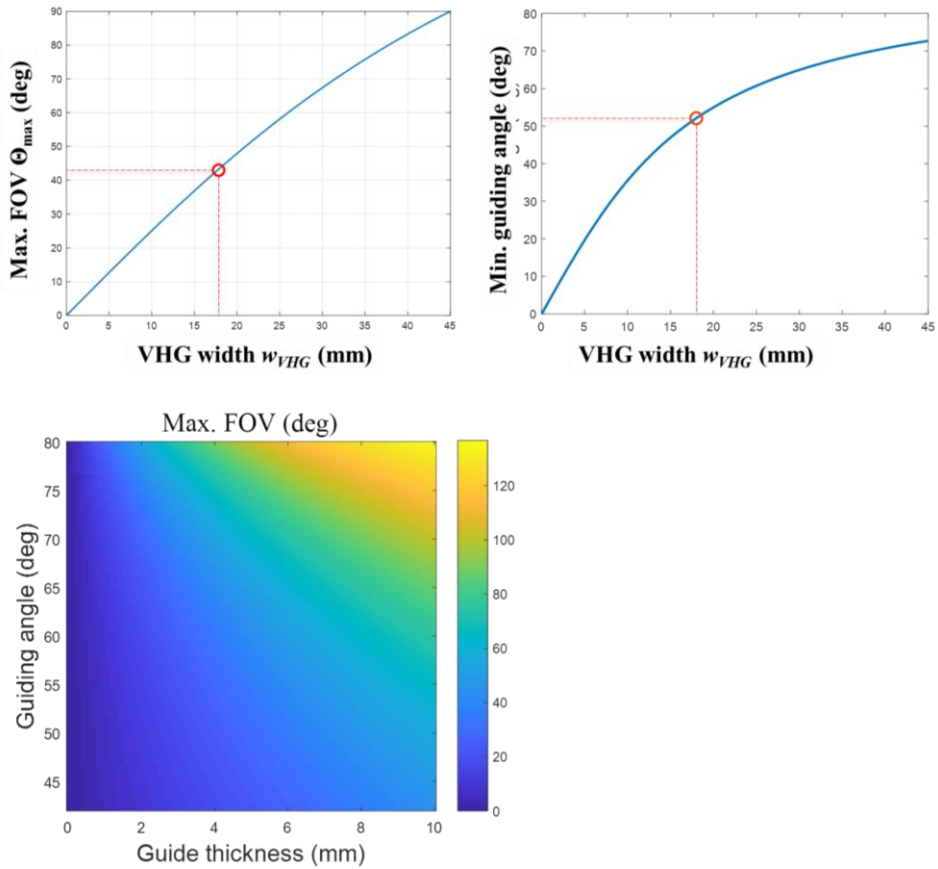


Figure 4.9 Trade-off relationships between design parameters.

Second, the difference between the two Bragg incidence angles (θ_{Bi}) of the multiplexed VHG's should be wider than the angular bandwidth of in-coupler and out-coupler VHG's for the two separate beams. This requirement can be simply written as:

$$|\theta_{B1} - \theta_{B2}| > \Delta\theta_1 + \Delta\theta_2, \quad (4.3)$$

where $\Delta\theta_i$ is the angle deviations from the Bragg incidence angle for which the diffraction efficiency firstly drops to near zero within the angular-selectivity range, as shown in Fig. 10. If the VHG's constraint in Eq. 4.3 is not satisfied; the multiplexed VHG can generate two diffraction beams for a single incident beam; accordingly, independent control of the viewpoint is not allowed.

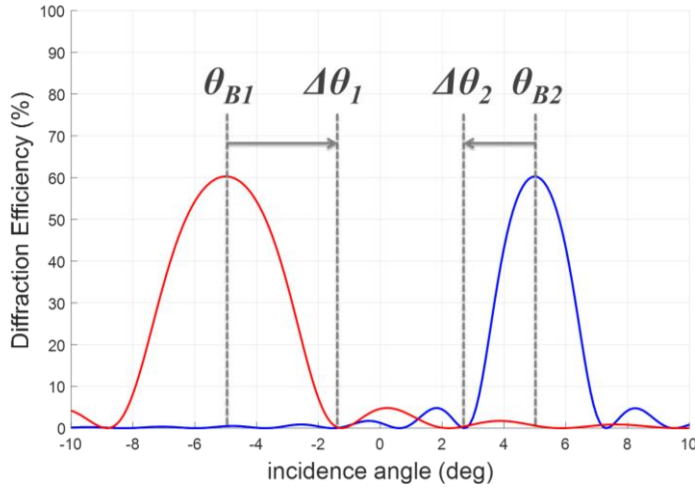


Figure 4.10 Schematic diagram of the VHG's constraint: the VHG's diffraction efficiency according to the incidence angle (angular selectivity).

Thirdly, the guided beams for two independent modes should be projected on the same location inside the out-coupler. The difference between the two projected positions (Δ_p) results in a reduction of the effective FOV to avoid the mislocation problem in Fig. 4.7. Given a first guiding angle θ_{g1} , the second guiding angle θ_{g2} is determined by the following equation:

$$\min_{\theta_{g2}} (m_1 \cdot 2d \tan \theta_{g1} + d \tan(\theta_p / n_g)) - (m_2 \cdot 2d \tan \theta_{g2} - d \tan(\theta_p / n_g)), \quad (4.4)$$

subject to $\theta_{g1}, \theta_{g2} \geq \theta_c$,

where $m_i \in \mathbb{N}$ is the number of TIR through the waveguide, n_g is the refractive index of the waveguide, and θ_c is the critical angle by TIR. By considering the inter-pupillary distance and eye position, the longitudinal length of the waveguide is limited to a specific range. Then n and m are restricted to be within specific values.

Optimal system parameters can be acquired by satisfying the design constraints above. By employing commercialized products, several key parameters are predetermined. In this experiment, the focal length of GPL is 45 mm (Edmund Optics S/N: 34-463), and the diffraction angle of polarization grating is 5 degrees in the air (Edmund Optics S/N: 12-677). The recording medium for VHGs is Covestro's Bayfol HX photopolymer film with 16 μm thickness, which is thick enough to have a narrow angular bandwidth. Based on Kogelnik's coupled-wave theory (CWT), the VHG's simulation result shows that the $\Delta\theta_i$ is approximately within 2 degrees, which means that the diffraction angle by the polarization grating should be larger than 3.3 degrees; so that the VHG's constraint by Eq. 4.3 is satisfied.

Taking into account the system performance and practicable experimental setup, other parameters are restricted as follows. Considering the precision and tolerances of the VHG recording setup, the guiding angle is limited between 48° and 65° with a step size of 1° . This limitation of step size hinders exact solutions in Eq. 4.4. To obtain nearest-neighbor solutions of the guiding angle, the value of Δ_p is allowed within 1 mm. The waveguide thickness is set between 5 and 8 mm by the allowable guiding angle by VHGs, thicker than the typical thickness range of the eyeglass (2~4 mm). For commercialization, the thickness should be reduced to the glasses-level by increasing the guiding angle. The waveguide length is limited to between 50 and 80 mm. The minimum value of the MAFOV is set to be 40 degrees.

Figure 4.11 presents the results of the optimal solution calculated by sweeping two guiding angles. In Fig. 4.11(c), the effective FOV means the modulated MAFOV calculated by considering Δ_p . The optimization results finally determine the specification of the guiding system and the recording conditions of VHG combiners. In a recording process of the in-coupler, the incidence angle of the reference beam is equal to $\pm\theta_p$ in the recording medium, and that of the signal beams is set to be a pair of guiding angles among searching results. In the out-coupler recording, the reference beam should be matched to the signal beam of the in-coupler and that of the signal beam, also defined as output angle θ_o , is determined by the position of the viewpoint.

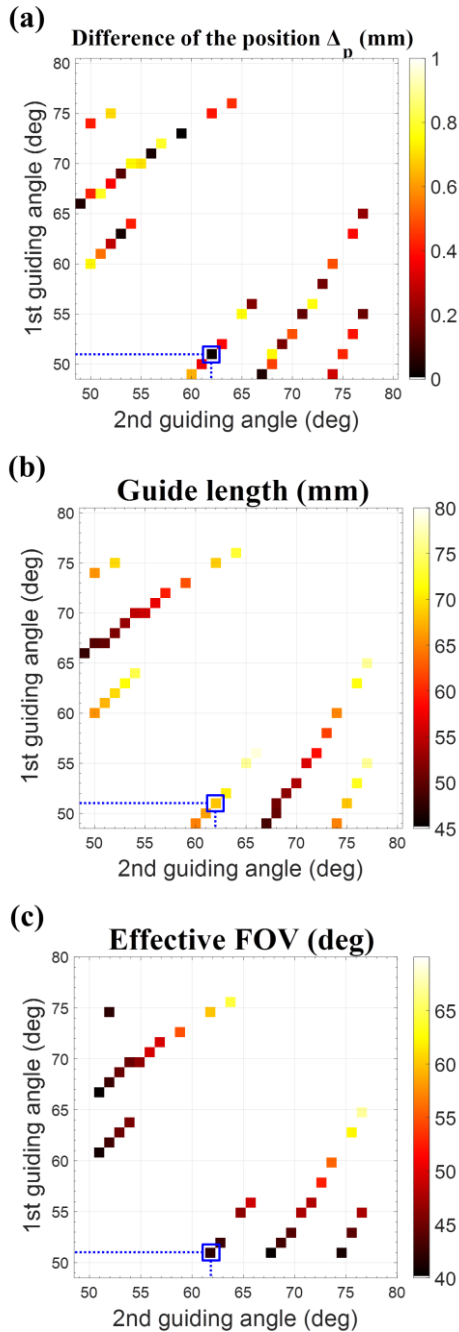


Figure 4.11 Optimized results of allowable guiding configurations: (a) positional difference (Δ_p) between the two projected beams on the out-coupler, (b) longitudinal length of the waveguide, and (c) effective FOV changed by misalignment of the two guiding beams. The blue dot lines indicate the value used in the prototype.

The diffracted beam by the out-coupler is incident on the PDEL and then is focusing at the focal length of PDEL on lens mode. The laterally shifted position of focal spots (P_i) in the horizontal direction can be given as follows under the paraxial condition:

$$P_i = d \tan \theta_o^i + f_{GP} \tan(n_g \theta_o^i) / 2, \quad (4.5)$$

where the plus sign of θ_o is defined to denote a clockwise rotation with respect to the direction normal to the waveguide surface. If viewpoints are located symmetrically about the normal axis, the spacing between the viewpoints (d_v) and the total eyebox width (S) are given as follows:

$$d_v^{i \sim i+1} = |P_i - P_{i+1}|, \quad (4.6)$$

$$S = \begin{cases} \sum_{i=1}^{n-1} d_v^{i \sim i+1} + D_p & \text{for } D_p > d_v \\ n \cdot D_p & \text{for } D_p \leq d_v \end{cases}, \quad (4.7)$$

where D_p is the pupil diameter. The pupil size is sensitively dependent on an environmental condition such as ambient light and typically varies from 2 mm to 8 mm. If the pupil size is larger than the spacing of the focal spots, a continuous eyebox can be provided; but if it is larger than twice the spacing, a double image will be projected on the retina. For an inverse situation, discrete eyebox is generated, which can provoke the blank screen or vignetting [79].

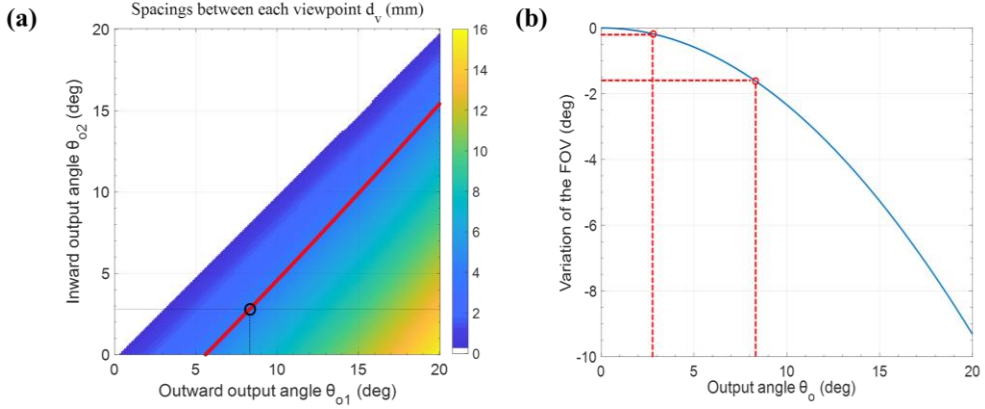


Figure 4.12 Simulation results: (a) the spacing between two viewpoints according to the output angle θ_o . The solid line indicates the pair of output angles with 4 mm spacing, which are target conditions in this experiment. (b) The FOV decrement according to the output angle. The dotted lines indicate reduced FOV variations at selected conditions in this experiment.

Figure 4.12(a) shows the relationship between output angles and the viewpoint spacing. In this experiment, the value of d_v is set to be 4 mm by considering the average pupil size of mid-age people [80]. In this condition, the double image is not observed even when the pupil size becomes large up to 8 mm. The inward output angle is 2.8° , and the outward angle is 8.3° , which is indicated by black dot lines in Fig. 4.12(a). The modulated FOV (Θ_i) according to each viewpoint, is given as follows:

$$\Theta_i = \tan^{-1} \left[\frac{w_{VHG}}{f_{GP}} + \tan(n_g \theta_o^i) \right] + \tan^{-1} \left[\frac{w_{VHG}}{f_{GP}} - \tan(n_g \theta_o^i) \right]. \quad (4.8)$$

Figure 4.12(b) presents that the effective FOV is reduced by increasing the output angle. However, the degraded FOV corresponding to the target viewpoint is within 2 degrees, as shown in Fig. 4.12(b).

Table 4.1 Specifications of the fabricated waveguide system.

Pre-decision		Optimized recording angle				Waveguide			
f_{GP}	θ_P	θ_{g1}	θ_{g2}	θ_{o1}	θ_{o2}	d	L	w_{VHG}	Θ_{max}
45 mm	$\pm 5^\circ$	51°	62°	8°	3°	7 mm	80 mm	17 mm	42°

Based on the simulation results and deployability of the system above, finally selected system parameters are listed in Table 4.1. Figure 4.13 shows the simulation results of ray tracing in LightTools, excluding a PDEL. In ray-tracing software, which does not support nanostructure devices such as polarization grating, the simulation modeling is modified separately according to the polarization state of the input beam. When using the parameters listed in Table 4.1, an input beam with a width of 17 mm (equal to w_{VHG}) can be propagated to the eyepiece part without distortion.

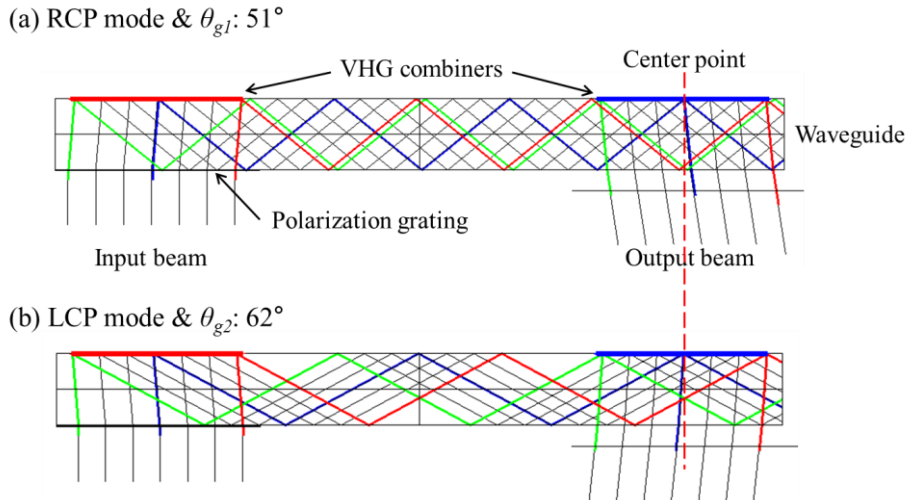


Figure 4.13 2-D layout of the designed waveguide system in LightTools. Each solid line is a ray path. Simulation result for input beam with (a) RCP mode and (b) LCP mode.

4.3 Compact retinal projection-based near-eye display with switchable viewpoints via waveguide configuration

4.3.1 Implementation of the prototype and experimental results

To validate the design parameter for the waveguide system, the experimental proof-of-concept is conducted, as shown in Fig. 4.14. The waveguide slab is fabricated using a polished glass with SCHOTT NBK7, of which thickness is 7 mm. The thickness of polarization grating and GPL is both 0.45 mm, and the aperture diameter is 25 mm. The PDEL is fabricated by stacking with optical adhesive, of which total thickness is about 1.3 mm. To avoid frustrated TIR, all polarization-dependent optical elements are attached to the waveguide with a thin air gap less than 0.1 mm. The VHG combiners are recorded with a wavelength of 532 nm, which is sequentially multiplexed by controlling the recording time and the intensity of beams. The recording angle is listed in Table 4.1; for quadruple multiplexing out-coupler, the pairs of recording angle (reference and signal beam) are $(62^\circ, 8^\circ)$ and $(62^\circ, -3^\circ)$, which are called *group 1* for LCP mode, $(51^\circ, 3^\circ)$ and $(51^\circ, -8^\circ)$, which are called *group 2* for RCP mode. Figure 4.14 shows the experimental setup and recording condition for the multiplexed VHG. To be stable and automatically adjust the recording angle, an automated recording setup using the chamber is established. The chamber system is designed to put index-matching oil in a frame made of optical glass. By utilizing the chamber system, there is no interfacial reflection between the recording medium and the air, so VHG recording with high efficiency can be implemented without a noise interference pattern. Mirrors are installed on the motorized linear stage and the rotation stage, and the stages and shutters are synchronized with the computer. By sequentially adjusting the tilting angle and position of the mirrors, VHG can be multiplexed in the recording process. The measured diffraction efficiency for a dual multiplexed in-coupler is 87% and 85%. The out-coupler efficiency is 47%, 44%, 18% and 47%.

respectively. The fabricated VHGs are resized with the width corresponding to the design value of w_{HOE} .

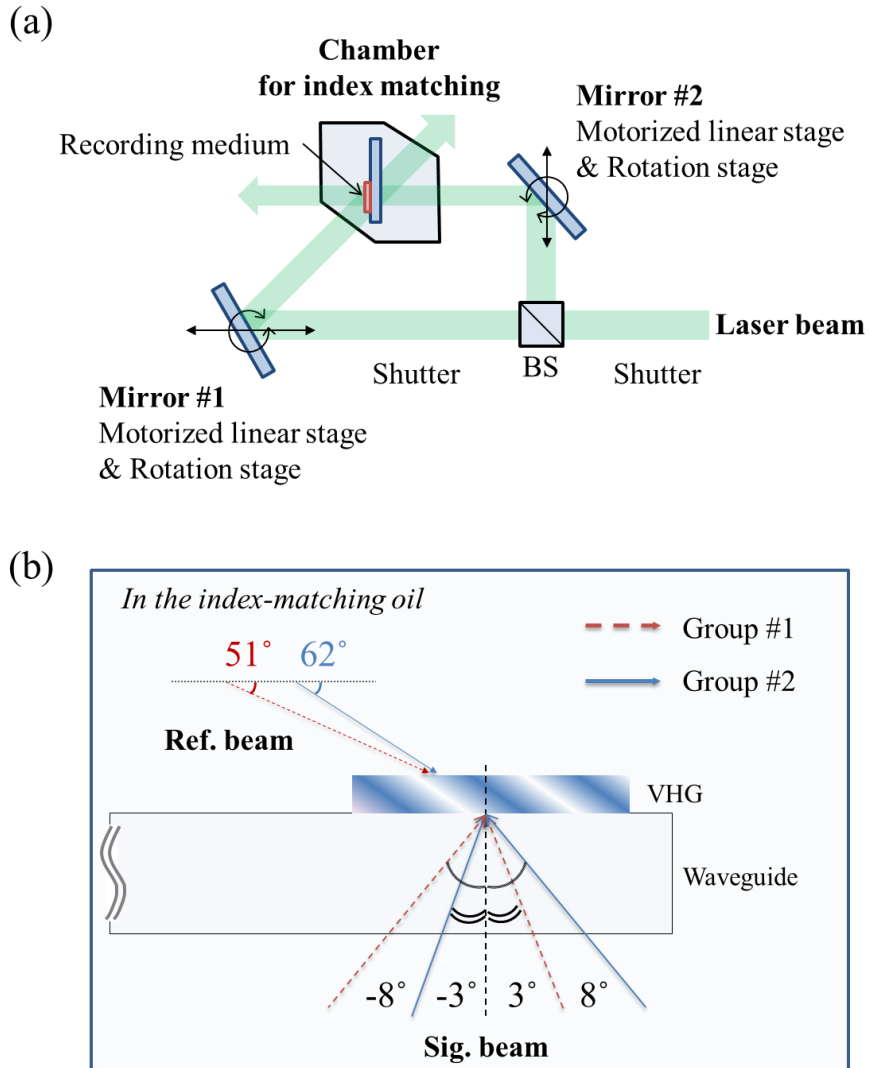


Figure 4.14 (a) Schematic diagram of the automatic VHG recording system. (b) Recording angle for the multiplexed VHG.

The experimental results show that each distance between focal spots is 4 mm or 5 mm, which has a slight gap with the target value (4 mm). Such a problem may arise from VHGs's fabrication error. The outward focal spots are blurred than inward, observed in Fig. 4.15. The sharpness degradation is caused by off-axis aberration by GPL [81] and can be mitigated using aberration-corrected GPLs [82]. The verification experiment results show that the designed polarization switching for focal spots operates well.

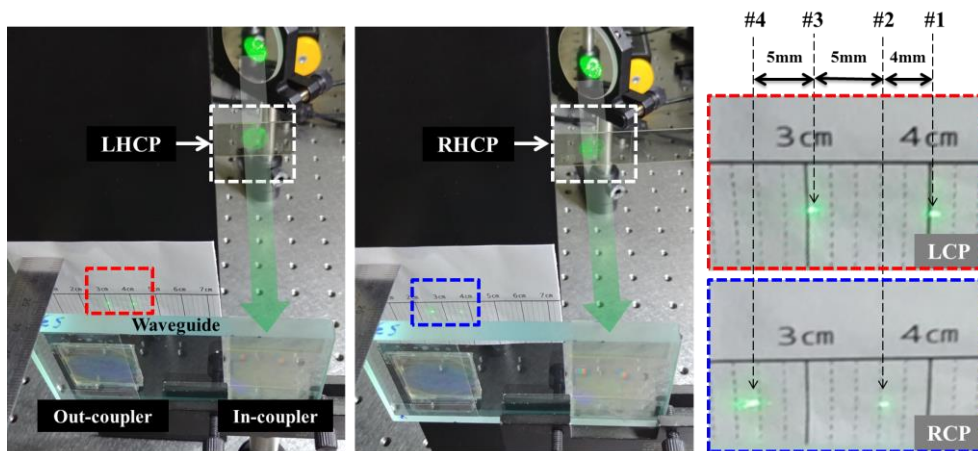


Figure 4.15 Experimental results for focal spots according to polarization of input beam. The grid paper is placed at the eye relief distance (22.5 mm).

The experimental setup for the waveguide system is constructed on the optical bench, as shown in Fig. 4.16. To provide sharp ray bundles with a compact system, we use a commercial LSP (Celluon Picopro) as a display source. The display resolution is 1280×720 pixels. The focal length of the collimating lens is 75 mm, which is employed by considering an effective resolution on intercross section of VHGs and divergence angle of the projector beam for a clear image. To enhance the sharpness of the image, an additional beam-shaping lens is employed. In this experiment, the focus-tunable lens is located between the LSP and collimating lens, which has optical power between -2 D and 3 D. The polarization rotator can

actively switch the polarization state of input beam with high-speed (10 ms) for a real-time operating system (Thorlabs LCC1221-A). The clear aperture of the polarization rotator is 20 mm, which is a critical aperture stop limiting the FOV. The smartphone with a wide-field camera ($f/1.8$ and 16 mm focal length) is used to capture resulting images because a CCD camera is not suitable for a short eye relief condition.

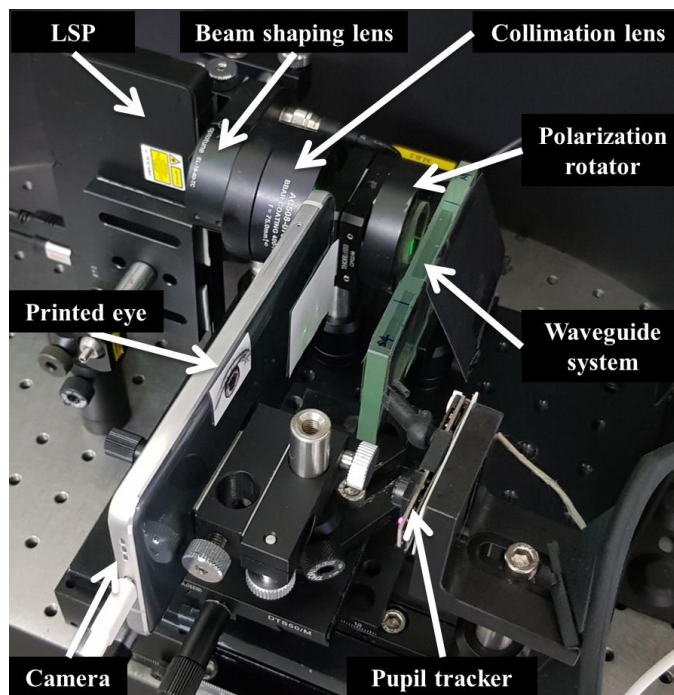


Figure 4.16 Prototype of the proposed configuration.

For dynamic switching, we synchronized the pupil tracker, polarization rotator, and display. The printed artificial eye on paper is attached to the smartphone camera, and the lateral shift of the pupil is simulated by moving the phone on the linear stage. The polarization state of the input beam is automatically changed to activate another viewpoint group when the shifting range of the imitated eye is more than half the spacing (2 mm). This prototype demonstrates the dynamic switching of focal spots and virtual images depending on the pupil position.

Figures 4.17(a) and 4.17(b) show the results of FOV measurement with a target paper located at 10 cm from the camera. Measured FOV at inward viewpoints is approximately 37 degrees in the horizontal direction and 45 degrees in the diagonal direction. The deteriorated FOV compared with simulation value (42°) may be caused by the misalignment of optical components. Figure 4.17(e) presents the AR scene in which the virtual image in Fig. 4.17(d) is superimposed on a real printout image in Fig. 4.17(c), which is located behind the waveguide.

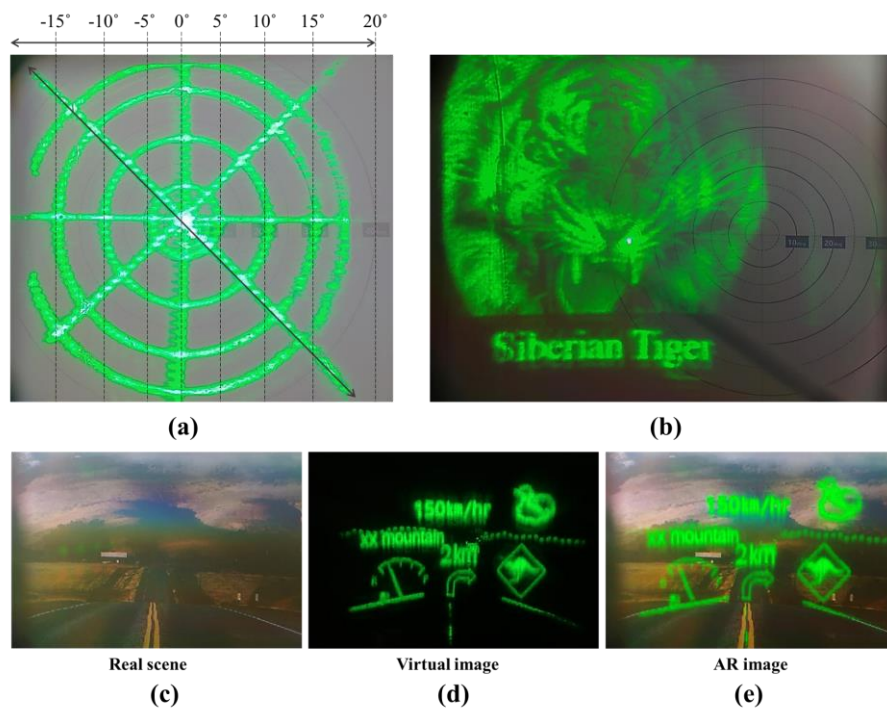


Figure 4.17 Photographs of experimental results; (a) AR scene of the rendering test circle image with real FOV target, (b) virtual image with maximum FOV, (c) printed driving screen image (real object), (d) virtual information images and (e) AR scene for simulated driving.

4.3.2 Performance analysis and discussion

To validate large DOF for a retinal-projection configuration, AR images are acquired by changing the focal depth of the camera, as shown in Fig. 4.18(a). All

captured results are the same quality regardless of the camera focus, demonstrating the all-in-focus property for the proposed configuration. Figure 4.18(b) shows the observed AR images at each focal spot. It is confirmed that virtual images can be rendered at separate viewpoints. Several image problems are observed in experimental results. A keystone distortion due to an oblique incidence at viewpoints can be resolved using additional calibration image processing [83]. In the see-through window mode, chromatic distortion of the real scene is slightly occurred, which may be caused by the misalignment and wavelength dispersion of the PDEL. A low contrast issue may result from VHG manufacturing, which can be alleviated by searching optimal fabrication conditions.

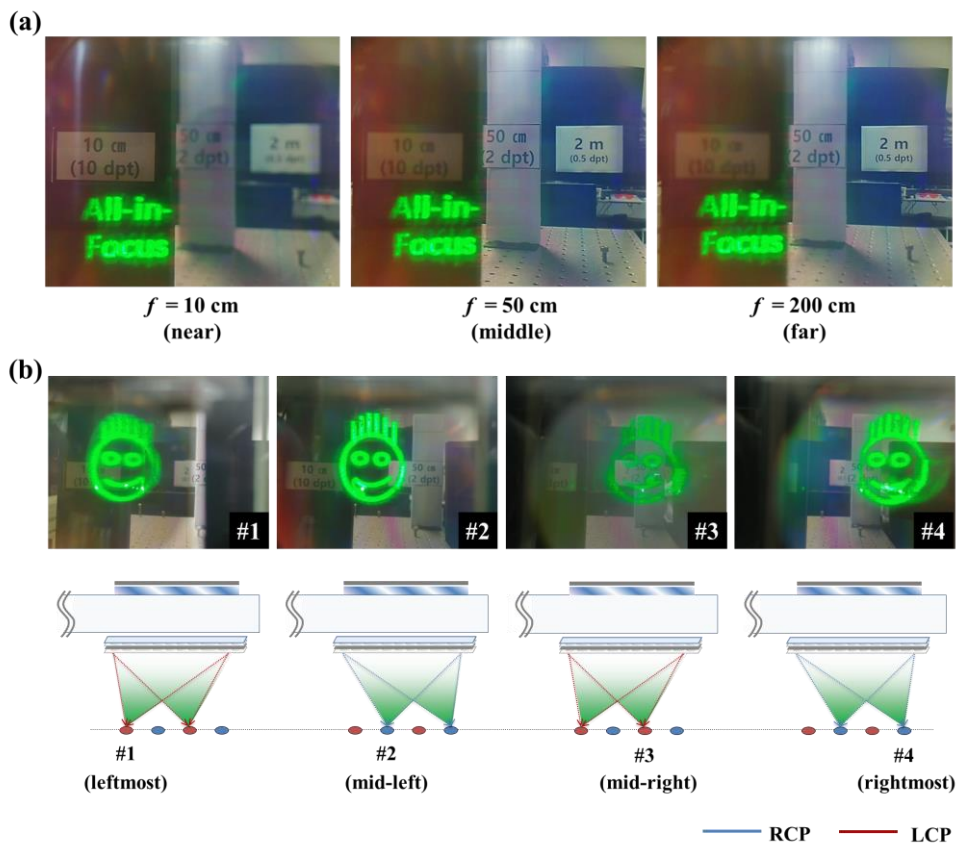
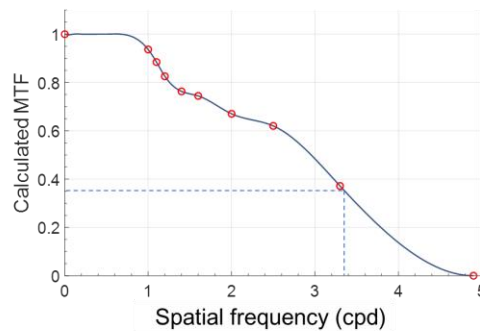


Figure 4.18 Experimental results: (a) with different focus depths of the camera, (b) at different viewpoints.

To analyze image quality for the implemented setup, angular resolution is measured at an inward viewpoint with low aberration. The maximum spatial frequency for the prototype system is 6.6 cpd in which the effective pixel size is about 30 μm in projected display on the out-coupler. The MTF contrast is acquired by calculating the contrast of captured fringe patterns and is indicated in Fig. 4.19. The cut-off frequency is about 3.4 cpd to adopt an MTF criterion of 35%. The MTF results obtained when the input beam is directly focused by a single GPL without a waveguide are equivalent to those in Fig. 4.19. This result means that resolution deterioration by the waveguide system can be negligible. The resolution degradation is caused by the Gaussian blur of the laser beam and needs a precise beam shaping for sharp images.



cpd	1.0	1.1	1.2	1.4	1.6
Captured image					
MTF	0.9367	0.8844	0.8256	0.7630	0.7444
cpd	2.0	2.5	3.3	4.8	6.6
Captured image					
MTF	0.6702	0.6202	0.3717	0	0

Figure 4.19 MTF results of the prototype system. The marked circle indicates measured values and the solid line indicates interpolated MTF curve using curve fitting.

Finally, we will discuss the polarization persistence within the waveguide. When an input beam with circular polarization is incident on the waveguide, the critical problem is that the polarization state is changed by VHGs and TIR. First, for the VHG, the polarization state for input beam with circular or elliptical polarization cannot remain due to the difference in diffraction efficiency between two orthogonal eigenvectors. Second, for the waveguide, the phase shift by TIR is different according to the polarization eigenmode and guiding angle. To sum up, for a circularly polarized input beam, the output beam is not circular polarization, as shown in Fig. 4.20. Accordingly, GPLs are simultaneously operated as a convex and concave lens, resulting in unwanted image noise.

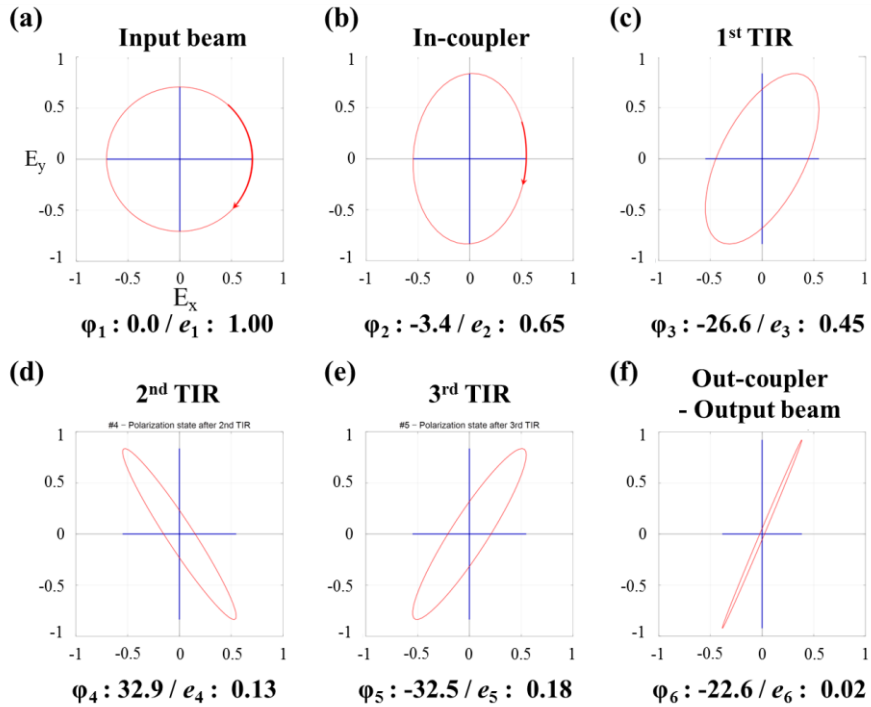


Figure 4.20 Simulation results of the polarization state along the optical path; (a) input beam with circular polarization, (b) diffracted beam by in-coupler, (c), (d), (e) guided beam according to TIR number, and (f) output beam extracted by out-coupler where ϕ_i is the inclination angle and e_i is the ellipticity.

4.4 Conclusion

In this chapter, the author proposed and demonstrated a novel retinal projection-based near-eye display that can independently activate two separate groups of viewpoints using polarization-multiplexing technique and waveguide configuration. The proposed system is constructed by polarization-dependent optics and multiplexed VHG combiners to provide an extended eyebox with a compact form factor. The author analyzed and optically designed a waveguide system in detail. The fabricated guiding system using optimal design parameters can provide quadruple focal spots for retinal projection with a short eye relief of 22.5 mm. We built a proof-of-concept system in which wide eyebox 16 mm and moderate FOV 45° are achieved for a 4 mm pupil condition. Previous studies with dynamic eyebox have several problems such as relatively bulky form factor or operating speed. The proposed configuration alleviates these problems with lightweight and thin optical devices. In addition, double or blank images arising from always-on focal spots can be mitigated. The proposed concept can also be applied in other display systems for optical path control with a compact form factor. The proposed configuration can provide an efficient way to resolve obstacles that hinder the proliferation of AR near-eye displays in various applications.

Chapter 5. Conclusion

This dissertation presents the studies on improving the display performance for waveguide-based AR near-eye display with the polarization multiplexing technique. Recently, many researchers are devoted to developing near-eye displays that provide high performance with comfortable wearing fit, and then various configurations, optical elements, and techniques have been proposed. Especially among diverse optical architectures, a waveguide-based near-eye display is one of the most promising technologies for AR experiences. The waveguide techniques typically comprise thin and lightweight waveguide and diffraction-based imaging combiners, which can enable a compact form factor and shape comparable to that of glasses. However, they still have challenging problems such as an insufficient FOV or complex modulation for the optical structure. In this regard, the key performance items and waveguide technology are introduced in Chapter 1.

The studies on this dissertation use a polarization multiplexing technique and polarization-dependent optical elements to enhance the display performance for waveguide-based near-eye display. The proposed polarization-dependent devices are fabricated by laminating geometric phase-based optical elements. The geometric phase optical devices have dual optical functions depending on the polarization state of the input beam. Using their phase conjugate property, it is possible to operate as a transparent optical window for a specific polarization mode and activate a lens or grating function for an orthogonal polarization mode. These polarization-dependent multi-functions can deliver real scenes without optical distortion, suitable for an AR eyepiece-combiner. Also, since the geometric phase devices used in this experiment are liquid crystal-based thin film, the polarization-dependent eyepiece can be easily attached to a conventional planar waveguide structure. The entire system is also lightweight and compact. To sum up their superior properties: they can provide twice the display performance than the

conventional configuration in combination with a high-speed temporal polarization multiplexing.

First, the author proposed a novel waveguide structure that increases the number of focal planes for a virtual image from single depth to dual depth. Thus, a polarization-dependent eyepiece lens (PDEL) is devised using a geometric phase lens with a doublet structure. The PDEL operates as an optical window for a horizontally polarized input beam and a concave lens for a vertically polarized beam. In a transmissive mode, the focal plane for a virtual image is formed at infinity, as in the conventional waveguide technique. For the lens mode, that is formed at a near distance equivalent to half the focal length of the geometric phase lens. For real scenes, the PDEL always operates in window mode to provide a distortion-free image. The prototype system has dual focal planes at infinity and $20D$, respectively. By synchronizing the display and the polarization controller, AR images corresponding to the two focal depths are synthesized in real-time. The experimental results demonstrate that the proposed configuration works properly. Consequently, the proposed system with dual focal planes can raise the visibility of virtual images superimposed on real scenes by considering the accommodation response.

Second, a novel configuration of the waveguide-based near-eye display is proposed to enlarge a FOV. In the traditional waveguide technique, the FOV is restricted by the design and material properties of the diffraction gratings. Due to this practical problem, commercial waveguide-based displays have a mid-level FOV of about 40 degrees. The author employed the polarization-dependent steering scheme to break through the FOV limitation by using polarization gratings. The novel polarization-dependent steering combiner (PDSC) is attached to the out-coupler part of the waveguide, which can control an optical path of the output beam depending on the polarization state. The author built a volume holographic grating-based proof-of-concept system with a horizontal 33.2° FOV that is twice as

wide as the conventional structure without a PDSC. The proposed method can extend the FOV up to the mid-50 degrees even with a substrate and diffraction gratings with a typical refractive index of 1.5, which is more improved than commercial waveguide-based products using a material with an index of 1.6 or higher.

Thirdly, the author suggested a retinal projection-based waveguide display with switchable viewpoints by polarization multiplexing. Active switching of viewpoints is implemented by employing angular-multiplexed volume gratings and polarization-dependent optics. The proposed configuration can activate one of the dual-divided viewpoint groups according to the pupil position. This operating scheme can support a pupil movement with an extended eyebox and mitigate image problem caused by duplicated viewpoints. By synchronizing the pupil tracker, display source, and polarization controller, a prototype demonstrates that only a specific viewpoint group is activated according to the eye movement. The proof-of-concept system provides all-in-focus images with an FOV of 45 degrees and a wide eyebox of 16 mm.

In summary, the author proposed methodologies to enhance the performance of waveguide-based near-eye displays based on polarization multiplexing. The proposed polarization-dependent eyepieces enable the polarization multiplexing of the waveguide system without compromising the form factor. In addition, the proposed configuration is very practical and versatile because of easy fabrication processes. However, there are still several problems to be applied to commercial waveguide-based near-eye displays. First, an optical efficiency drop caused by many polarizing optics is critical. The polarization-dependent eyepieces used in this dissertation require two polarizing filters to control the operating mode, which reduces the optical efficiency by up to 25%. In this case, it is difficult for the user to observe the real objects clearly in a dark AR environment as if wearing sunglasses indoors. In addition, for a virtual image, a bright display source with

high intensity should be adopted, which causes excessive power consumption. Second, it is difficult to generate more than two modes using a static polarization control film. For more operating modes, a multi-layered polarization-dependent eyepiece is required, which can be implemented by inserting active-type retarders. Most of these devices are based on liquid crystal, and a real-time operating system for multi-mode is very challenging due to their limited response speed.

For future work, the author will focus on optical devices with high efficiency for a specific polarization. For this, it is necessary to manufacture a customized optical device, not commercialized polarization-dependent optics that have a maximum converting efficiency for circularly polarized input beam. By applying customized optical devices tailored to a specific function or polarization mode, such as a meta-surface, the optical efficiency can be increased, and optical aberration by an overlapped structure can be reduced. Additionally, a study on innovative approaches to solving various problems in the waveguide technique will be conducted. The author expects that this dissertation can suggest efficient solutions to penetrate obstacles that hinder the proliferation of AR near-eye displays in various applications.

Bibliography

1. E. N. Merieb, and K. Hoehn, *Human Anatomy & Physiology 7th Edition* (Mount Royal University, 2007).
2. D. Park, Y. Kim, and Y. Park, "Hyperrealism in full ultra high-definition 8K display," *SID Int. Symp. Digest Tech. Papers* 50(1), 1138-1141 (2019).
3. C.D. Wickens, "Three-dimensional stereoscopic display implementation: Guidelines derived from human visual capabilities," *Stereoscopic displays and applications*. International Society for Optics and Photonics, 2-11 (1990).
4. D. Williams, "Benchmarking of the ISO 12233 slanted-edge spatial frequency response plug-in," In *PICS*, pp. 133-136 (1998).
5. M. Duocastella, F. Tantussi, A. Haddadpour, R. P. Zaccaria, A. Jacassi, G. Veronis, A. Diaspro, and F. D. Angelis, "Combination of scanning probe technology with photonic nanojets," *Sci. Rep.* 7(1), 1-7 (2017).
6. J. P. Rolland, A. Yoshida, L. D. Davis, and J. H. Reif, "High-resolution inset head-mounted display," *Appl. Opt.* 37, 4183-4193 (1998).
7. ISO 12233:2017, International Organization for Standardization (ISO), <https://www.iso.org/standard/71696.html>
8. H. Li, Y. Changxiang, and S. Jianbing, "Measurement of the modulation transfer function of infrared imaging system by modified slant edge method," *JOSK* 20(3), 381-388 (2016).
9. S. H. Schwartz, *Visual Perception: A Clinical Orientation* (McGraw Hill, 2009).
10. C. Vieri, G. Lee, N. Balram, S. H. Jung, J. Y. Yang, S. Y. Yoon, and I. B. Kang, "An 18 megapixel 4.3" 1443 ppi 120 Hz OLED display for wide field of view high acuity head mounted displays," *J. Soc. Inf. Disp.* 26(5), 314-324 (2018).
11. I. P. Howard and B. J. Rogers, *Binocular Fusion and Rivalry in Binocular Vision and Stereopsis* (Oxford University, 1995).
12. Wikipedia, "Comparison of virtual reality headsets," https://en.wikipedia.org/wiki/Comparison_of_virtual_reality_headsets
13. R. Zhang, "Design of Head mounted displays," (2007).

14. H. Pashler, V.S. Ramachandran, and M.W. Becker, "Attending to a misoriented word causes the eyeball to rotate in the head," *Psychon Bull Rev.*, 13(6), 954-957 (2006).
15. B. C. Kress and T. Starner, "A review of head-mounted displays (HMD) technologies and applications for consumer electronics," *Proc. SPIE* 8720, 87200A (2013).
16. A. Maimone, A. Georgiou, and J. S. Kollin, "Holographic near-eye displays for virtual and augmented reality," *ACM Trans. Graph.* 36(4), 85 (2017).
17. I. P. Howard, *Perceiving in Depth* (New York: Oxford University Press, 2012).
18. S. Nagata, "How to reinforce perception of depth in single two-dimensional pictures," *Spatial displays and spatial instruments*, 29 (1987).
19. N. O. Kenneth and J. T. Schwartz, "Depth of Focus of the Human Eye," *J. Opt. Soc. Am.* 49, 273-280 (1959).
20. T. Shibata, J. Kim, D. M. Hoffman, and M. S. Banks, "The zone of comfort: Predicting visual discomfort with stereo displays," *J. Vis.* 11(8), 11 (2011).
21. S. Liu and H. Hua, "Time-multiplexed dual-focal plane head-mounted display with a liquid lens," *Opt. Lett.* 34(11), 1642-1644 (2009).
22. D. Kim, S. Lee, S. Moon, J. Cho, Y. Jo, and B. Lee, "Hybrid multi-layer displays providing accommodation cues," *Opt. Express*, 26(13), 17170-17184 (2018).
23. S. Lee, Y. Jo, D. Yoo, J. Cho, D. Lee, and B. Lee, "Tomographic near-eye displays," *Nat. Commun.* 10, 2497 (2019).
24. F. Seeber, "Light Sources and laser safety," *Fundamentals of photonics 1.2* (2007).
25. G. W. Larson, R. Holly, and P. Christine, "A visibility matching tone reproduction operator for high dynamic range scenes." *IEEE Transactions on Visualization and Computer Graphics* 3(4), 291-306(1997).
26. Seeing is believing, "How virtual reality and augmented reality are transforming business and the economy,"

- https://www.pwc.ch/en/publications/2020/Seeing_is_believing_PwC_AR_VR.pdf
27. Google Co., Google Glass, <https://www.google.com/glass/start/>
 28. K. Pulli, "Meta 2: Immersive Optical-See-Through Augmented Reality," SID Int. Symp. Digest Tech. Papers 48(1), 132–133 (2017).
 29. Mira Co., Mira Prism, <https://mirareality.com/>
 30. Nreal, Co., Nreal Light, <https://www.nreal.ai/product>
 31. X. Hu and H. Hua, "High-resolution optical see-through multi-focal-plane head-mounted display using freeform optics," Opt. Express 22(11), 13896–13903 (2014).
 32. K. Sarayedine and K. Mirza, "Key challenges to affordable see-through wearable displays: the missing link for mobile AR mass deployment," Proc. SPIE 8720, 87200D (2013).
 33. J. Bornemann and F. Arndt, "Transverse resonance, standing wave, and resonator formulations of the ridge waveguide eigenvalue problem and its application to the design of E-plane finned waveguide filters," IEEE transactions on microwave theory and techniques 38(8), 1104-1113 (1990).
 34. D. Cheng, Y. Wang, C. Xu, W. Song, and G. Jin, "Design of an ultra-thin near-eye display with geometrical waveguide and freeform optics," Opt. Express 22(17), 20705–20719 (2014).
 35. M. Xu and H. Hua, "Methods of optimizing and evaluating geometrical lightguides with microstructure mirrors for augmented reality displays," Opt. Express 27(4), 5523-5543 (2019).
 36. LUMUS Co., Lumus Optical Engines, <https://lumusvision.com/technology/>
 37. Optinvent Co., ORA-2, <https://www.optinvent.com/>
 38. Y. Amitai, "Extremely Compact High-Performance HMDs Based on Substrate-Guided Optical Element," SID Int. Symp. Digest Tech. Papers 35(1), 301–313 (2004).
 39. B. C. Kress, "Optical waveguide combiners for AR headsets: features and limitations," Digital Optical Technologies 2019, 11062, International Society for Optics and Photonics (2019).

40. J. Kim, Y. Li, M. N. Miskiewicz, C. Oh, M. W. Kudenov, and M. J. Escuti, "Fabrication of ideal geometric phase holograms with arbitrary wavefronts," *Optica* 2(11), 958–964 (2015).
41. N. Matsuda, A. Fix, and D. Lanman, "Focal surface displays," *ACM Trans. Graph.* 36(4), 86 (2017).
42. B. C. Kress and W. J. Cummings, "Towards the ultimate mixed reality experience: HoloLens display architecture choices," *SID Int. Symp. Digest Tech. Papers* 48(1), 127–131 (2017).
43. H. J. Yeom, H. J. Kim, S. B. Kim, H. Zhang, B. Li, Y. M. Ji, S. H. Kim, and J. H. Park, "3D holographic head mounted display using holographic optical elements with astigmatism aberration compensation," *Opt. Express* 23(25), 32025–32034 (2015).
44. S.-B. Kim and J.-H. Park, "Optical see-through Maxwellian near-to-eye display with an enlarged eyebox," *Opt. Lett.* 43(4), 767–770 (2018).
45. I. Hamilton, "What Magic Leap One and Facebook's Half Dome Have In Common". <https://uploadvr.com/magic-leap-one-half-dome-common-differences/>
46. F. S. Roux, "Geometric phase lens," *JOSA A*, 23(2), 476–482 (2006).
47. C. Jang, K. Bang, S. Moon, J. Kim, S. Lee, and B. Lee, "Retinal 3D: augmented reality near-eye display via pupil-tracked light field projection on retina," *ACM Trans. Graph.* 36(6), 190 (2017).
48. H. Kogelnik, "Coupled wave theory for thick hologram gratings," *Bell Syst. Tech. J.* 48(9), 2909–2947 (1969).
49. H. H. Cheng, A. K. Bhowmik, and P. J. Bos, "Fast-response liquid crystal variable optical retarder and multilevel attenuator," *Opt. Eng.* 52(10), 107105 (2013).
50. W. T. Chen, A. Y. Zhu, V. Sanjeev, M. Khorasaninejad, Z. Shi, E. Lee & F. Capasso, "A broadband achromatic metalens for focusing and imaging in the visible," *Nature nanotechnology*, 13(3), 220–226 (2018).

51. C. Kim, S.-J. Kim, and B. Lee, "Doublet metalens design for high numerical aperture and simultaneous correction of chromatic and monochromatic aberrations," *Opt. Express* 28(12), 18059–18076 (2020).
52. N. V. Tabiryan, S. V. Serak, S. R. Nersisyan, D. E. Roberts, B. Y. Zeldovich, D. M. Steeves, and B. R. Kimball, "Broadband waveplate lenses," *Opt. Express* 24, 7091-7102 (2016).
53. P. E. Napieralski, B. M. Altenhoff, J.W. Bertrand, L. O. Long, S. V. Babu, C. C. Pagano, J. Kern, and T. A. Davis, "Near-field distance perception in real and virtual environments using both verbal and action responses," *ACM Trans. Appl. Percept.* 8(3), 1–19 (2011).
54. O. Cakmakci and J. Rolland, "Head-worn displays: A review," *J. Disp. Technol.* 2(3), 199–216 (2006).
55. Vallius, T. and Tervo, J. Waveguides with extended field of view. US Patent 9,791,703 (2017).
56. J. Han, J. Liu, X. Yao, and Y. Wang, "Portable waveguide display system with a large field of view by integrating freeform elements and volume holograms," *Opt. Express* 23(3), 3534–3549 (2015).
57. C. Yu, Y. Peng, Q. Zhao, H. Li, and X. Liu, "Highly efficient waveguide display with space-variant volume holographic gratings," *Appl. Opt.* 56(34), 9390–9397 (2017).
58. Z. Shen, Y. Zhang, Y. Weng, and X. Li, "Characterization and optimization of field of view in a holographic waveguide display," *IEEE Photonics J.* 9(6), 1–11 (2017).
59. Y. Weng, D. Xu, Y. Zhang, X. Li, and S.-T. Wu, "Polarization volume grating with high efficiency and large diffraction angle," *Opt. Express* 24(16), 17746–17759 (2016).
60. X. Xiang, J. Kim, R. Komanduri, and M. J. Escuti, "Nanoscale liquid crystal polymer Bragg polarization gratings," *Opt. Express* 25(16), 19298–19308 (2017).

61. Z. Shi, W. T. Chen, and F. Capasso, "Wide field-of-view waveguide displays enabled by polarization-dependent metagratings," *Proc. SPIE* 10676, 1067615 (2018).
62. S. R. Nersisyan, N. V. Tabiryan, D. M. Steeves, and B. R. Kimball, "The promise of diffractive waveplates," *Opt. Photonics News* 21(3), 40–45 (2010).
63. G. Bianco, M. A. Ferrara, F. Borbone, A. Roviello, V. Striano, and G. Coppola, "Photopolymer-based volume holographic optical elements: design and possible applications," *Journal of the European Optical Society-Rapid publications*, 10, 15057 (2015).
64. J. Kim, C. Oh, M. J. Escuti, and S. Serati, "Wide-angle nonmechanical beam steering using thin liquid crystal polarization gratings," *In Advanced Wavefront Control: Methods, Devices, and Applications VI*, International Society for Optics and Photonics, 7093, pp.709302 (2008).
65. A. Duane, "Studies in monocular and binocular accommodation, with their clinical application," *Transactions of the American Ophthalmological Society* 20, 132 (1922).
66. N. Uchida, "Calculation of diffraction efficiency in hologram gratings attenuated along the direction perpendicular to the grating vector," *J. Opt. Soc. Am* 63, 280–287 (1973).
67. P. Artal, *Handbook of Visual Optics, Two-Volume Set* (CRC Press, 2017).
68. C. Oh and M. J. Escuti, "Achromatic diffraction from polarization gratings with high efficiency," *Opt. Lett.* 33(20), 2287–2289 (2008).
69. G. Westheimer, "The Maxwellian view," *Vision Res.* 6(12), 669–682 (1966).
70. M. Sugawara, M. Suzuki, and N. Miyauchi, "Retinal imaging laser eyewear with focus-free and augmented reality," in *SID Symposium Digest of Technical Papers* (2016), pp. 164–167.
71. P. K. Shrestha, M. J. Pryn, J. Jia, J. Chen, H. Fructuoso, A. Boev, Q. Zhang, and D. Chu, "Accommodation-free head mounted display with comfortable 3D perception and an enlarged eye-box," *AAAS Research* (2019).

72. R. Konrad, N. Padmanaban, K. Molner, E. A. Cooper, and G. Wetzstein, "Accommodation-invariant computational near-eye displays," *ACM Trans. Graph.* 36(4), 88 (2017).
73. J. Kim, Y. Jeong, M. Stengel, K. Akşit, R. Albert, B. Boudaoud, T. Greer, W. Lopes, Z. Majercik, P. Shirley, J. Spjut, M. McGuire, and D. Luebke, "Foveated AR: dynamically-foveated augmented reality display," *ACM Trans. Graph* 38(4), 99 (2019).
74. M. Hedili, B. Soner, E. ulusoy, and H. Urey, "Light-efficient augmented reality display with steerable eyebox," *Opt. Express* 27(9), 12572–12581 (2019).
75. J. Jeong, J. Lee, C. Yoo, S. Moon, B. Lee and B. Lee, "Holographically customized optical combiner for eye-box extended near-eye display," *Opt. Express.* 27(26), 38006–38018 (2019).
76. H. Chen, Y. Weng, D. Xu, N. V. Tabiryan, and S.-T. Wu, "Beam steering for virtual/augmented reality displays with a cycloidal diffractive waveplate," *Opt. Express* 24(7), 7287–7298 (2016).
77. R. E. Stevens, D. P. Rhodes, A. Hasnainb, and P.Y. Laffontb, "Varifocal technologies providing prescription and VAC mitigation in HMDs using Alvarez lenses," *Digital Optics for Immersive Displays* 10676. (2018).
78. A. Pu and M. Spie, "Exposure schedule for multiplexing holograms in photopolymer films," *Opt. Eng.* 35, 2824– 2829 (1996).
79. K. Ratnam, R. Konrad, D. Lanman, and M. Zannoli, "Retinal image quality in near-eye pupil-steered systems," *Opt. Express* 27(26), 38289–38311 (2019).
80. I. M. Borish, *Clinical refraction, 3rd ed.* (Professional press, Chicago, 1970).
81. M. Khorasaninejad, W. T. Chen, J. Oh, and F. Capasso, "Super-dispersive off-axis meta-lenses for compact high resolution spectroscopy," *Nano Lett.* 16(6), 3732–3737 (2016).
82. K. J. Hornburg, X. Xiang, J. Kim, M. Kudenov, and M. Escuti, "Design and fabrication of an aspheric geometric-phase lens doublet," *Proc. SPIE* 10735, 1073513 (2018).

83. A. Bauer, S. Vo, K. Parkins, F. Rodriguez, O. Cakmakci, and J. P. Rolland, "Computational optical distortion correction using a radial basis function-based mapping method," *Opt. Express* 20(14), 14906–14920 (2012).

Appendix

Portions of the work discussed in this dissertation were also presented in the following publications:

[**Chapter 2**] C. Yoo, K. Bang, C. Jang, D. Kim, C.-K. Lee, G. Sung, H.-S. Lee, and B. Lee, “Dual-focal waveguide see-through near-eye display with polarization-dependent lenses,” *Optics Letters*, vol. 44, pp. 1920-1923 (2019).

[**Chapter 3**] C. Yoo, K. Bang, M. Chae and B. Lee, “Extended-viewing-angle waveguide near-eye display with a polarization-dependent steering combiner,” *Optics Letters*, vol. 10, pp. 2870-2873 (2020).

[**Chapter 4**] C. Yoo, M. Chae, S. Moon, and B. Lee, “Retinal projection type lightguide-based near-eye display with switchable viewpoints,” *Optics Express*, vol. 28, pp. 3116-3135 (2020).

초 록

본 박사학위 논문에서는 편광 다중화 기법을 이용하여 도파관 기반의 증강현실 근안 디스플레이의 성능을 향상시키는 광학 설계 및 이에 대한 분석에 대해 논의한다. 본 연구는 도파관 기반 근안 디스플레이의 가장 큰 장점인 소형 폼 팩터를 유지하면서 디스플레이 성능을 개선하는 것에 중점을 둔다. 이를 위해 기존 광학 소자에 비해 매우 가볍고 얇은 편광 의존형 결합기 광학 소자가 새롭게 제안되며, 이는 입사광의 편광 상태에 따라 독립적인 광 경로 제어를 가능케 하여 편광 다중화를 통해 향상된 성능을 제공 할 수 있다. 또한 실제 영상의 빛은 그대로 투과 시킴으로써 증강현실을 위한 소자로 활용 가능하다.

본 연구에서 제안하는 편광 의존형 결합기 광학 소자는 기하학적 위상(geometric phase, GP)에 기반하여 동작한다. GP 기반의 광학소자가 서로 직교하는 원형 편광 입사광에 대해 상보적인 기능을 수행하는 것을 이용하여, 두 개 이상의 GP 소자와 편광 제어를 위한 광학 필름들을 중첩 시킴으로써 증강현실 결합기 광학 소자를 구현할 수 있다. 이들 광학 소자는 매우 얇기 때문에, 본 연구에서 제작된 편광 의존형 결합기 광학 소자의 총 두께는 1 mm 수준으로 폼 팩터 제약으로부터 자유롭다. 또한 평평한 필름 형태이므로, 평판형 도파관에 부착하기 쉽다는 이점을 지닌다.

고안된 편광 의존형 결합기 광학 소자를 사용하여 세 가지 유형의 새로운 도파관 기반의 근안 디스플레이 구조를 제안한다. 첫 번째는 입사광의 편광 상태에 따라 투명 광학 창 또는 오목 렌즈로 작동하는 편광 의존형 결합기 렌즈를 적용하여 가상 영상에 대해 이중 초점면을 제공하

는 시스템이다. 제안된 구조는 기존의 도파관 기반 근안 디스플레이가 무한대 위치에 단일 초점면을 제공함으로써 발생하는 시각적 피로 및 흐릿한 증강현실 영상의 문제를 완화할 수 있다. 두 번째로는 입사광의 편광 상태에 따라 광 경로를 좌측 또는 우측으로 제어할 수 있는 편광 격자를 활용하여 가상 영상의 시야각을 기존보다 최대 2배까지 확장할 수 있는 시스템을 제안한다. 이는 단일 도파관 기반 근안 디스플레이에서 영상 결합기 (imaging combiner)로 활용되는 회절 소자의 설계 변수에 의해 제한되는 시야각 한계점을 돌파할 수 있는 구조로 컴팩트한 폼 팩터로 더욱 몰입감 있는 대화면 증강현실 영상을 제공할 수 있다. 마지막으로 위에서 제안된 두 가지 편광 의존형 광학 소자를 모두 사용하여 시점 전환이 가능한 도파관 기반의 망막 투사형 디스플레이 구조를 제안한다. 편광 다중화를 통해 다중 초점들을 선택적으로 활성화함으로써, 확장된 시정영역을 제공하는 동시에 동공 크기 변화 또는 움직임에 의한 이중 영상 문제를 완화할 수 있다. 또한 기계적 움직임 없이 시점 간의 고속 전환이 가능하다는 장점을 지니고 있다.

본 박사학위 논문에서 제시한 편광 다중화를 활용한 새로운 결합기 광학 소자 및 광학 구조들은 도파관 기반 근안 디스플레이의 향상된 성능을 제공하는 해결책 및 새로운 가능성으로 제시할 수 있을 것이라 기대된다.

주요어 : 증강현실, 근안 디스플레이, 도파관, 편광 다중화, 기하위상 광학 소자, 홀로그래픽 광학 소자, 편광 격자, 체적 격자, 망막 투사 디스플레이

학 번 : 2016-20939